FRAGMENTATION OF JETS PRODUCED IN PROTON-ANTIPROTON COLLISIONS AT $\sqrt{S} = 1.96$ TEV

By

SERGO R. JINDARIANI

A DISSERTATION PRESENTED TO THE GRADUATE SCHOOL
OF THE UNIVERSITY OF FLORIDA IN PARTIAL FULFILLMENT
OF THE REQUIREMENTS FOR THE DEGREE OF
DOCTOR OF PHILOSOPHY

UNIVERSITY OF FLORIDA

2007

1

To my newborn daughter Elizabeth, to my beautiful wife Oksana, and to my parents,

Valentina and Robert Jindariani, all of whom I love.

ACKNOWLEDGMENTS

I am grateful to Sasha Pronko, who taught me how to do an experimental analysis and helped me a lot during the early stage of it. I also learned from him that it is very important to set a goal and work hard to achieve it.

I want to thank Prof. Jacobo Konigsberg, the leader of the University of Florida High Energy Physics Group and CDF co-spokesperson, for his support. I also appreciate the opportunity to be a part of the University of Florida High Energy Physics Group. It was a pleasure to work with such great colleagues as Sergei Klimenko, Alexander Sukhanov, Song Ming Wang, Roberto Rossin, Nathan Goldschmidt, Valentin Necula and George Lungu. I also thank the entire High Energy Group of University of Florida for supporting me financially during all five years in graduate school, and for the opportunity to travel to many conferences to present the results. These experiences helped me build confidence in my place in the high energy physics community. I emphasize the role of Prof. Guenakh Mitselmakher in building a very strong HEP experimental group at UF.

Life is not only physics, and I also had many great friends over my graduate career whom I have been able to share my experiences with. At UF, Victor Barashko, Craig Group, Khristian Kotov, Alexei Drozdetski, Yuriy Pakhotin and many others contributed indirectly to my success. I also thank all my friends from Tbilisi State University and from high school, who are now scattered all over the world, but still keep in touch.

I thank my high school physics teacher, Tengiz Bibilashvili, who is the best teacher I've known, for dedication to his work. He was the one who introduced physics to me and played a very important role in my choice to pursue a career in physics. I also thank my advisor at the Joint Institute for Nuclear Research, Joseph Manjavidze, for helping me to develop skills very useful in high energy physics.

TABLE OF CONTENTS

CHAPTER

LIST OF TABLES

LIST OF FIGURES

11

13

15

Abstract of Dissertation Presented to the Graduate School
of the University of Florida in Partial Fulfillment of the
Requirements for the Degree of Doctor of Philosophy

FRAGMENTATION OF JETS PRODUCED IN PROTON-ANTIPROTON COLLISIONS
AT $\sqrt{S} = 1.96$ TEV

By

Sergo R. Jindariani

December 2007

Chair: Andrey Korytov
Major: Physics

We present the first measurement of two-particle momentum correlations in
jets produced in $p\bar{p}$ collisions at center of mass energy of 1.96 TeV. A comparison
of the experimental data to theoretical predictions obtained for partons within the
framework of resummed perturbative QCD (Next-to-Leading Log Approximation)
shows that the predicted parton momentum correlations survive the hadronization
stage of jet fragmentation and are present at the hadron level. We also present the
measurement of the intrinsic transverse momenta of particles with respect to jet axis (k_T).
Experimental data is compared to the theoretical predictions obtained for partons within
the framework of Modified Leading Log Approximation and Next-to-Modified Leading
Log Approximation, and shows good agreement in the range of validity of the theoretical
predictions. The results of both measurements indicate that the perturbative stage of
the jet formation must be dominant and give further support to the hypothesis of Local
Parton-Hadron Duality.

16

CHAPTER 1
INTRODUCTION

Since the dawn of civilization humanity has been trying to understand what are the fundamental constituents of matter. As early as around 400 BC atomism arose as an explanatory scheme with the ancient Greeks, Leucippus, Democritus, and Epicurus, and the Roman poet, Lucretius. At the most fundamental level atomism is the belief that all phenomena are explicable in terms of the properties and behavior of ultimate, elementary, localized entities (or "fundamental particles"). Thus it prescribes a strategy for the construction of scientific theories in which the behavior of complex bodies is to be explained in terms of their component parts. That strategy has led to many of the successes of modern physical science, though these do not prove that there actually are 'ultimate entities' of the type postulated by atomism.

Modern particle physics began in the early 20th century as an exploration into the structure of the atom. The discovery of the atomic nucleus in the gold foil experiment of Geiger, Marsden, and Rutherford was the foundation of the field. The components of the nucleus were subsequently discovered in 1919 (the proton) and 1932 (the neutron). In the 1920s the field of quantum physics was developed to explain the structure of the atom and the spectrum of black-body radiation..

The binding of the nucleus could not be understood by the physical laws known at the time. Based on electromagnetism alone, one would expect the protons to repel each other. In the mid-1930s, Yukawa proposed a new force to hold the nucleus together, which would eventually become known as the strong nuclear force. He speculated that this force was mediated by a new particle called a meson. Also in the 1930s, Pauli postulated the neutrino as an explanation for the observed energy spectrum of beta decay, and Fermi

proposed an effective theory of the weak force. Separately, the positron and the muon were discovered by Anderson. Yukawa's meson was discovered in the form of the pion in 1947. Over time, the focus of the field shifted from understanding the nucleus to the more fundamental particles and their interactions, and particle physics became a distinct field from nuclear physics.

Throughout the 1950s and 1960s, a bewildering variety of additional particles was found in scattering experiments. This was referred to as the "particle zoo". This term was deprecated after the formulation of the Standard Model during the 1970s in which the large number of particles was explained as combinations of a (relatively) small number of fundamental particles. The Standard Model can be truly considered as one of the greatest achievements of science.

1.1 Standard Model of Elementary Particles

A fundamental interaction or fundamental force is a mechanism by which particles interact with each other, and which cannot be explained in terms of another interaction. Every observed physical phenomenon can be explained by these interactions. The apparent irreducible nature of these interactions leads physicists to study the properties of these forces in great detail. In modern physics, there are four fundamental interactions (forces): gravitation, electromagnetism, the weak interaction, and the strong interaction.

The Standard Model [1] of particle physics is a theory which describes three of the four known fundamental interactions between the elementary particles that make up all matter. It is a quantum field theory [2] developed between 1970 and 1973 which is consistent with both quantum mechanics and special relativity. The Standard Model is based on the principle of the local gauge invariance of the group $SU(3)_c \times SU(2)_L \times U(1)_Y$. $SU(3)_c$ represents the symmetry group of the strong

interaction while $SU(2)_L \times U(1)_Y$ represents the symmetry group of the unified electroweak interaction. Gravity is not included in the Standard Model but the strength of gravitational interactions is so small that it becomes important only on macroscopic scales. The detailed description of the Standard Model is beyond the scope of this dissertation. Here we discuss only the particle content of the Standard Model and its aspects relevant to the jet fragmentation physics. More detailed discussions can be found in [3].

The matter particles described by the Standard Model all have an intrinsic spin whose value is determined to be 1/2, making them fermions. For this reason, they follow the Pauli exclusion principle in accordance with the spin-statistics theorem giving them their material quality. Apart from their antiparticle partners, a total of twelve different types of matter particles are known and accounted for by the Standard Model. Six of these are classified as quarks: up (u), down (d), strange (s), charm (c), top (t) and bottom (b), and the other six as leptons: electron (e), muon (μ), tau (τ), and their corresponding neutrinos (ν_e, ν_μ, ν_τ). These particles carry charges which make them susceptible to the fundamental forces. Pairs from each group (one up-type quark and one down-type quark, or a down-type lepton and its corresponding neutrino) form a generation. Corresponding particles between each generation are identical to each other apart from their masses and flavors. The properties of quarks and leptons are summarized in Tables 1-1 and 1-2.

The force-mediating particles described by the Standard Model all have an intrinsic spin whose value is 1, making them bosons. As a result, they do not follow the Pauli Exclusion Principle. Photons mediate the electromagnetic force between electrically charged particles. The photon is massless and is well-described by the theory of quantum electrodynamics (QED). All known fermions interact via the weak interaction. It is mediated by the exchange of the three gauge bosons: W^+, W^- and Z°. They are massive,

with the Z° being more massive than W$^\pm$. Furthermore, the W$^\pm$ carry an electric charge and couple to the electromagnetic interactions. These three gauge bosons along with the photons are grouped together which collectively mediate the electroweak interactions, as described by the Glashow-Salam-Weinberg (GSW) theory [4, 5].

Each quark carries any one of three color charges - red, green or blue, enabling them to participate in strong interactions mediated by the eight gluons. Gluons are massless. The eight-fold multiplicity of gluons is labeled by a combinations of color and an anticolor charge. Because the gluon has an effective color charge, they can interact among themselves. The gluons and their interactions are described by the theory of quantum chromodynamics (QCD) [6?]. The properties of gauge bosons are summarized in Table 1-3.

The only particle predicted by Standard Model yet to be discovered is the Higgs boson (H). This boson plays a key role in explaining the origins of the mass of other elementary particles, in particular the difference between the massless photon and the very heavy W and Z bosons. It is also needed to give fermions their masses. Masses arise in a gauge invariant way, due to a process known as the Higgs mechanism [7]. In this mechanism, the local $SU(2)_L \times U(1)_Y$ symmetry of the electroweak interactions is spontaneously broken. This aspect of the theory correctly predicts the existence of the weak gauge bosons as well as the ratio of their masses. It also predicts the existence of a spin 0 particle: the Higgs boson. The search for the Standard Model Higgs boson remains one of the top priorities at the Tevatron and the future LHC experiments.

To date, almost all experimental tests of the three forces described by the Standard Model have agreed with its predictions. The most impressive is the agreement between the predicted and measured values of the W and Z gauge bosons masses. The Standard

Model predictions have also lead to the discovery of top quark at the Tevatron. Still, the Standard Model falls short of being a complete theory of fundamental interactions, primarily because of its lack of inclusion of gravity, but also because of the large number of numerical parameters (such as masses and coupling constants) that must be put "by hand" into the theory rather than being derived from first principles.

1.2 Quantum Chromodynamics

Quantum chromodynamics (QCD) is the theory of the strong interaction (color force), a force describing the interactions of the quarks and gluons found in hadrons.

With the invention of bubble chambers and spark chambers in the 1950s, experimental particle physics discovered a large and ever-growing number of particles called hadrons. It seemed that such a large number of particles could not all be fundamental. First, the particles were classified by charge and isospin; then, in 1953, according to strangeness by Murray Gell-Mann and Kazuhiko Nishijima. To gain greater insight, the hadrons were sorted into groups having similar properties and masses using the eightfold way, invented in 1961 by Gell-Mann and Yuval Neeman. Gell-Mann and George Zweig went on to propose in 1963 that the structure of the groups could be explained by the existence of three flavors of smaller particles inside the hadrons: the quarks [8]. At this stage, one particle, the Δ^{++} remained mysterious; in the quark model, it is composed of three up quarks with parallel spins. However, since quarks are fermions, this combination is forbidden by the Pauli exclusion principle. In 1965 this problem was resolved by proposing that quarks possess an additional SU(3) gauge degree of freedom, later called color charge [9] and that quarks interact via an octet of vector gauge bosons: the gluons.

A coupling constant g, is a number that determines the strength of an interaction. In quantum field theory, a beta-function $\beta(g)$ encodes the running of a coupling constant. It

is defined by the relation:

$$\beta(g) = \mu \frac{\delta g}{\delta \mu}. \tag{1-1}$$

where μ is the energy scale of a given physical process.

In non-Abelian gauge theories, the beta function can be negative, as first found by F. Wilczek, D. Politzer and D. Gross [10, 11]. As a result the QCD coupling decreases logarithmically at high energies:

$$\alpha_s(Q^2) = \frac{4\pi}{\beta_0 \ln(Q^2/\Lambda_{QCD}^2)}, \tag{1-2}$$

where Λ_{QCD} is the energy scale at which the coupling in QCD diverges. This behavior of the coupling constant implies two very important properties of QCD. It is easy to see that at high values of Q^2 the coupling constant becomes small, this leads to the property called asymptotic freedom. Basically it implies that in high-energy scattering the quarks move within nucleons are essentially free, non-interacting particles. At low Q^2 the coupling diverges. This property of QCD is known as the color confinement and is the reason why free quarks and gluons are not observed in nature. Instead, they form color singlet objects known as hadrons.

Different theoretical methods can be used to describe processes in each of the two domains of QCD. At short distances (high Q^2) the methods of perturbative QCD (pQCD) can be applied, while phenomenological models are used at long distances (low Q^2). The behavior (running) of the QCD coupling is mainly due to the presence of self-interaction of gauge bosons.

The Λ_{QCD} parameter depends on the renormalization scheme and number of active flavors (number of quarks with mass $m_q < Q$). Its value was determined experimentally to

be approximately 200 MeV. Therefore, the perturbative approach breaks down for scales comparable with masses of light hadrons ($Q \sim 1$ GeV).

1.3 Structure of QCD Events

Measurements described in this dissertation were conducted in proton-antiproton environment at the Tevatron. The nature of these collisions is much more complicated than at the electron-positron colliders. The protons and antiprotons consist not only of the "valence" quarks, but also from a "sea" of quarks and gluons being constantly produced and annihilated. Each of these partons carries a fraction of the total energy of a hadron. Therefore, the actual colliding particles are not protons and antiprotons but rather quarks and gluons. Functions that describe probability of finding a certain constituent carrying some certain fraction of hadrons energy are called parton distribution functions (PDFs).

The inelastic cross-section of the proton-antiproton collisions is largely dominated by the "soft" component, meaning that only a small amount of momentum is transfered into the new particles. However, sometimes a hard scattering can occur. In this case partons with large transverse momenta are being created in the collision. These partons radiate soft gluons creating the so called parton shower. The probability of a gluon with momentum k and transverse momentum $k_\perp$ being emitted off a quark with momentum p is:

$$dw^{q \rightarrow q+g} = 2C_F \frac{\alpha_s(k_\perp)}{4\pi}[1 + (1 - \frac{k}{p})^2]\frac{dk}{k}\frac{dk_\perp^2}{k_\perp^2}, \qquad (1-3)$$

where

$$\alpha_s(k_\perp) = \frac{2\pi}{\beta_0}ln(k_\perp/\Lambda), \qquad (1-4)$$

$$C_F = (N_c^2 - 1)/2N_C = 4/3. \qquad\qquad (1\text{--}5)$$

N_C here denotes number of colors. It is easy to see that jet evolution is determined by the emission of soft and collinear gluons [12], i.e. $w \sim \alpha_s \ln^2 p \sim 1$ when $k \ll p$. The emission of a parton at large angle is also possible, however it is suppressed [12]: $w \sim \alpha_s/\pi \ll 1$ when $k \sim p$. The parton shower state of an event cannot be observed physically, but is often referred as parton level.

Due to the color confinement property of QCD, partons in the shower have to hadronize into the color singlet hadrons. A jet is a narrow cone of hadrons and other particles produced by the hadronization of a quark or gluon. The particle content of an event after the hadronization is often referred as hadron level.

The detection of hadrons in an experiment is done using their interaction with the material of the detector. Physically measured collection of objects is usually tracks and calorimeter towers referred to as the detector level.

The primary hard scattering can sometimes be accompanied by another parton-parton interaction within the same proton-antiproton collision, this process is called Multiple Parton Interaction (MPI). The MPI together with the beam-beam remnants contribute to the underlying event. The presence of the underlying event complicates measurements in the hadron collider environment since one has to disentangle contributions of particles coming from the hard scattering and from the underlying event. It is not possible to correct for this effect on an event-by-event basis, but the average correction factor can be reconstructed statistically.

In addition to these difficulties, a measurement is further complicated by the fact that the primary hadrons collide in bunches and there may be multiple proton-antiproton

interactions within the same bunch crossing. The effect is called pileup, it is luminosity dependent and can be accounted by considering only particles coming from the same primary vertex.

Table 1-1. Summary of quark properties.

	Particle	Spin	Charge	Mass
1st Generation	u	1/2	2/3	1.5-4 MeV/c^2
	d	1/2	-1/3	4-8 MeV/c^2
2st Generation	c	1/2	2/3	1.15-1.35 GeV/c^2
	s	1/2	-1/3	80-130 MeV/c^2
3rd Generation	t	1/2	2/3	170.9 ± 1.8 GeV/c^2
	b	1/2	-1/3	4.1-4.4 GeV/c^2

Table 1-2. Summary of lepton properties.

	Particle	Spin	Charge	Mass
1st Generation	e^-	1/2	-1	0.511 MeV/c^2
	ν_e	1/2	0	¡3×10^{-6}
2st Generation	μ^-	1/2	-1	105.7 MeV/c^2
	ν_μ	1/2	0	< 0.19
3rd Generation	τ^-	1/2	-1	1777 MeV/c^2
	ν_τ	1/2	0	< 18.2

Table 1-3. Summary of gauge boson properties of the Standard Model.

Boson	Spin	Electric charge	Mass
Photon (γ)	1	0	0
W	1	± 1	80.398 ± 0.025 GeV/c^2
Z	1	0	91.1876 ± 0.0021 GeV/c^2
Gluon (g)	1	0	0

CHAPTER 2
JET FRAGMENTATION

2.1 Motivation and Phenomenology

In the description of jet fragmentation it is important to keep in mind that it is governed by the fundamental properties of QCD - asymptotic freedom and the color confinement.

In the previous chapter it was outlined that theoretical methods used to describe QCD phenomena at low and high transfered momenta Q^2 are different. It was also discussed that formation and evolution of the QCD jets happens in two stages, and that particles that we are able to observe in detectors are hadrons, produced after the hadronization. A cartoon description of the different levels of a jet event is shown in Fig. 2-1. QCD provides the means to apply perturbative techniques to hadronic processes with large transferred momenta. The first stage, parton showering, which is driven by the emission of gluons at relatively large momenta, can be described using pQCD methods. The pQCD calculation techniques used to describe the parton shower development are commonly referred as soft gluon resummations. However, the second, color confinement stage of the jet formation, happens at small momentum transfers ($<$ 1 GeV), and the strong coupling becomes large, making it impossible to utilize the perturbative approach.

A common assumption about hadronization is Local Parton-Hadron Duality (LPHD) [13], which states that parton distributions are simply renormalized in the process of hadronization, without changing their shape. LPHD originated from the idea of soft preconfinement, whereby partons group in colorless clusters without disturbing the initial spectra. Phenomenological models of hadronization have been incorporated into Monte Carlo simulations of inelastic processes and in most cases support the approximate

property of LPHD. The framework of pQCD and LPHD forms the so-called analytical perturbative approach to QCD jet physics.

Simplified estimates suggest either that hadronization does not drastically alter the parton level results or else that its effects can be estimated from the energy dependence of experimental observables. Phenomenologically, the distributions of partons and hadrons are often found to be remarkably similar. This implies that the study of the partonic stage of an event is of utmost importance since the properties of high energy multihadronic events are primarily determined at that level.

In this dissertation we present studies of fragmentation of jets produced in proton-antiproton collisions at a center-of-mass energy 1.96 TeV. These studies address the question whether basic properties of jets are being shaped in the partonic stage of their development, as predicted by theory.

2.2   Soft Gluon Resummations

For predictions of final states with large numbers of partons, one cannot use the conventional perturbative approach based on the fixed order calculations. Instead, theorists use so called soft gluon resummation techniques. The main idea here is to reorganize the perturbative expansion so that the terms with leading collinear singularities are summed to all orders.

The leading logarithm approximation (LLA) [14] allows one to perform a resummed perturbative calculation of the parton shower by keeping all terms of order $\alpha_s^n \ln^n(Q)$ and at all orders n of perturbation theory. In this equation, α_s is the strong coupling constant and Q is the energy scale. The logarithmic expansion terms $\alpha_s^n \ln^n(Q)$ stem from the fact that in the region of finite momentum fractions the quark can emit a collinear gluon with probability $w^{q \to q+g} \sim \int \alpha_s dk_\perp^2 / k_\perp^2$, where $k_\perp$ is the gluons transverse momentum.

The idea of the LLA arose as an attempt to describe the logarithmic deviations from the true Bjorken scaling behavior. However, despite its success in deep inelastic scattering, the LLA fails to give a satisfying description of jet fragmentation, which is dominated by the soft gluon emissions.

The lowest order approximation allowing one to describe the dynamics of soft gluon emission is the so called Double Log Approximation (DLA) [15], in which all the terms of the order of $\alpha_s^n \ln^{2n}(Q)$ are resummed, while contribution of the higher order logarithmic terms is neglected. The DLA gets its name from the double logarithmic infrared and collinear singularities of gluon emissions. In any QCD process, the energies of cascading partons degrade during their evolution, and a proper accounting for soft partons, their recoil due to interaction, and energy-momentum conservation laws should be included. All these considerations are neglected in the DLA, for which only processes with rather large gradient of energies and emission angles at each stage of evolution are considered.

In order to include leading infrared singularities one must account for the effects of soft gluon interference. It has been shown that the effect of this interference is completely destructive to leading order outside of an angle-ordered region for each parton decay. That is, one can preserve the probabilistic interpretation of the cascade simply by restricting the phase space allowed for each parton branching so that the opening angles always decrease. This is called angular ordering [16] and leads to a suppression of the number of soft partons.

Account is taken of soft partons and strict transverse momentum ordering in subsequent terms of the perturbative series, such as the Next-to-Leading Log Approximation (NLLA) [17]. NLLA allows one to perform a resummed perturbative calculation of the parton shower by keeping all terms of order $\alpha_s^n \ln^{2n}(Q)$ and $\alpha_s^n \ln^{2n-1}(Q)$ at all orders n

of perturbation theory. Most of the particles in jets have $k_T < 1$ GeV/c, where k_T is the transverse momentum with respect to the jet axis. Therefore, in order to successfully describe jet fragmentation, a theoretical model must be able to handle particle emissions at very low transverse momenta scales. In NLLA, a sufficiently high cut-off scale Q_{cutoff} is selected to ensure that all partons have $k_T > Q_{cutoff}$ so that the perturbative calculations can be applied. After the resummation, the value of the parameter Q_{cutoff} can often be lowered down to the value of Λ_{QCD}. The phenomenological scale replacing the two initial parameters Q_{cutoff} and Λ_{QCD} is conventionally called Q_{eff}. The value of Q_{eff} was measured experimentally and found to be ~ 200 MeV.

The NLLA approach keeps only terms that are fully controlled within the calculation. The Modified Leading Log Approximation (MLLA) approach partially includes higher order terms. The next-to-MLLA (NMLLA) calculation keeps all terms of the order $\alpha_s^n \ln^{2n}(Q)$, $\alpha_s^n \ln^{2n-1}(Q)$, and $\alpha_s^n \ln^{2n-2}(Q)$, and partially includes higher order terms.

2.3 Local Parton-Hadron Duality

QCD yields results on partons, and not hadrons, as already mentioned. Therefore an assumption about hadronization must be made in any comparison of experimental data to theory.

LPHD [13] is a hadronization conjecture that suggests that the conversion of partons into hadrons occurs at a low virtuality scale, independent of the scale of the primary hard process, and the properties of hadrons and partons are closely related. Therefore, predictions made for partons with $k_T > Q_{eff}$ should be also valid for hadrons. With increasing energy sensitivity to the cutoff, Q_{eff}, decreases, thus LPHD is expected to be correct asymptotically.

In the simplest interpretation of LPHD, each parton at the end of the pQCD shower development picks up a color-matching partner from the vacuum sea and forms a hadron. Within LPHD, one relates particle multiplicity of hadrons to the multiplicity of partons via an energy-independent constant K_{LPHD}:

$$N_{hadrons} = K_{LPHD} \cdot N_{partons} \qquad (2\text{--}1)$$

This statement should also be valid for the inclusive momentum distributions of partons and hadrons. The inclusive momentum distribution function of particles in jets $D(\xi) = \frac{dN}{d\xi}$ in NLLA (MLLA) is defined in terms of variable $\xi = \ln(\frac{1}{x})$ where $x = \frac{p}{E_{jet}}$ and p is the parton momentum. Within the LPHD framework:

$$\frac{dN_{hadrons}}{d\xi} = K_{LPHD} \cdot \frac{dN_{partons}}{d\xi}. \qquad (2\text{--}2)$$

Past studies of inclusive particle distributions at e^+e^- experiments and CDF gave strong support to the LPHD hypothesis. In this dissertation, we extend the LPHD test by examining whether the two-particle momentum correlations predicted in the pQCD framework also survive the hadronization. We also address the question of whether MLLA and NMLLA predictions for the transverse momenta of particles in jets agree with the corresponding distributions for hadrons.

2.4 Theoretical Predictions and Past Measurements

2.4.1 Mean Particle Multiplicities

The analytical perturbative approach to QCD jet physics allows one to make predictions for many different observables. In this section we briefly discuss theoretical

predictions for the mean particle multiplicity and momentum distributions and provide more detailed description of the two-particle momentum correlations and the k_T distributions of particles in jets. Theoretical predictions for these observables are based on calculations carried out in the framework of NLLA supplemented with the LPHD hypothesis. We also present a review of the results of past measurements.

One particularly simple observable, which contains information about the dynamics of hadron production, is the charged particle multiplicity distribution. A number of QCD models make predictions for the evolution of the shape and the leading moments of the multiplicity distribution as a function of the center-of-mass energy. In addition, in QCD, quarks and gluons have different probabilities (proportional to their color factors) to emit gluons, therefore jets produced by quarks and gluons are expected to exhibit a difference in their fragmentation properties.

Past experimental studies of mean particle multiplicity in jets in e^+e^- environment indicated qualitative agreement with theoretical predictions. However, the reported results of measurements of the ratio of gluon and quark jet multiplicities $r = N_g/N_q$ varied from $r \approx 1.1$ to $r \approx 1.5$ [19], most of which were significantly below the theoretical predictions, $r \approx 1.4 - 1.8$ [20].

In $p\bar{p}$ environment, it was found by the CDF collaboration [22], that data agrees with perturbative QCD calculations carried out in the framework of MLLA, if: a) the ratio of parton multiplicities in quark and gluon jets r equals 1.7 ± 0.3, and b) the ratio of the number of charged hadrons to the number of partons $K_{LPHD}^{charged}$ is 0.55 ± 0.10. The results of the measurement are shown in Fig. 2-2. Another measurement [24] based on the comparison of CDF dijet and photon-jet data, with different contents of quark and gluon

jets in the final state, yields $r = 1.8 \pm 0.2$ which agrees well with re-summed perturbative QCD calculations.

2.4.2 Momentum Distributions

Another interesting observable is inclusive momentum distribution of particles in jets and its evolution with jet energy. The distributions are expected to be sensitive to effects of QCD coherence (gluon interference).

The inclusive momentum distribution function of partons in jets $D(\xi) = \frac{dN}{d\xi}$ in NLLA is defined in terms of the variable $\xi = \ln(\frac{1}{x})$ where $x = \frac{p}{E_{jet}}$ and p is the parton momentum. This distribution is predicted to have a distorted Gaussian shape [21]:

$$D(\xi) = \frac{N}{\sigma\sqrt{(2\pi)}} exp(\frac{1}{8}k - \frac{1}{2}s\delta - \frac{1}{4}(2+k)\delta^2 + \frac{1}{6}s\delta^3 + \frac{1}{24}k\delta^4), \tag{2–3}$$

with $\delta = \frac{\xi - \bar{\xi}}{\sigma}$ and

$$\bar{\xi} = \frac{\tau}{2}(1 + \frac{\rho}{24}\sqrt{\frac{48}{\beta\tau}}) + O(1), \tag{2–4}$$

$$\sigma = \sqrt{\frac{\tau}{3}}(\frac{\beta\tau}{48})^{1/4}(1 - \frac{\beta}{64}\sqrt{\frac{48}{\beta\tau}}), \tag{2–5}$$

$$s = -\frac{\rho}{16}\sqrt{\frac{3}{\tau}}(\frac{48}{\beta\tau})^{1/4}, \tag{2–6}$$

$$k = -\frac{27}{5\tau}(\sqrt{\frac{\beta\tau}{48}} - \frac{\beta}{24}). \tag{2–7}$$

Here β and ρ are constants which depend on the number of flavors and the number of effectively massless quarks. The position of the maximum ξ_0 and its width depend on the jet hardness Q. The predicted dependence of the inclusive momentum distribution

on jet hardness is shown in Fig. 2-3. The predictions contain three free parameters: normalization $N(Q)$, Q_{eff}, and an unknown higher order correction term $O(1)$ [27] to the ξ_0. Prediction for the inclusive momentum distribution were also obtained in the MLLA framework [25, 26], the results were similar to those of NLLA [27].

Comparisons of momentum distributions observed in data to the NLLA and MLLA predictions have been performed in several e^+e^- and ep experiments and show good qualitative agreement. The distributions were fitted for the value of the Q_{eff} parameter and the normalization factor $K_{LPHD}^{charged}$. Q_{eff} was found to have a value around 250 MeV. On the other hand, the measurements of $K_{LPHD}^{charged}$ were too high ($\approx$ 1.3) to be consistent with one-to-one parton-hadron correspondence. In $p\bar{p}$ environment the only measurement was performed by the CDF collaboration. The results of the measurement were $Q_{eff} = 240 \pm 20$ MeV and $K_{LPHD}^{charged} = 0.56 \pm 0.10$. The fit of the CDF data to the MLLA function is shown in Fig. 2-4. The inclusive momentum distributions are closely related to one of the main topics of this dissertation - the two-particle momentum correlations in jets, which will be discussed in the next section.

2.4.3 Two-particle Momentum Correlations

In this thesis we address the question of whether more subtle effects, such as momentum correlation, also survive hadronization. The predictions for the parton momentum correlations at the level of NLLA precision were first obtained by C.P. Fong and B.R. Webber in [27] and recently recalculated in the Modified Leading Log Approximation (MLLA) framework in [28]. These pQCD-driven correlations extend over a large range of parton momenta and should not be confused with phenomenological short-range Bose-Einstein correlations [29].

The two-particle momentum correlation function $R(\xi_1, \xi_2)$ is defined to be the ratio of the two- and one-particle momentum distribution functions:

$$R(\xi_1, \xi_2) = \frac{D(\xi_1, \xi_2)}{D(\xi_1)D(\xi_2)}, \tag{2–8}$$

where $D(\xi_1, \xi_2) = \frac{d^2 N}{d\xi_1 d\xi_2}$. The momentum distributions are normalized as follows: $\int D(\xi)d\xi = \langle n \rangle$, where $\langle n \rangle$ is the average multiplicity of partons in a jet, and $\int D(\xi_1, \xi_2)d\xi_1 d\xi_2 = \langle n(n-1) \rangle$ for all pairs of partons in a jet. The average multiplicity of particles $\langle n \rangle$ is a function of the dijet mass M_{jj} and the size of the opening angle θ_c. For $\theta_c = 0.5$, $\langle n \rangle$ varies from ~ 6 to ~ 12 for M_{jj} in the range 80–600 GeV/c^2 [22].

The NLLA approximation of Eq. (2–8) for the two-particle momentum correlation function [27] can be written as follows:

$$R(\Delta\xi_1, \Delta\xi_2) = r_0 + r_1(\Delta\xi_1 + \Delta\xi_2) + r_2(\Delta\xi_1 - \Delta\xi_2)^2, \tag{2–9}$$

where $\Delta\xi = \xi - \xi_0$, ξ_0 is the position of the maximum of $D(\xi)$ and parameters r_0, r_1, and r_2 define the strength of the correlation and depend on the variable $\tau = \ln(Q/Q_{eff})$. Eq. 2–9 is valid only for particles with ξ around the peak (ξ_0) of the inclusive particle momentum distribution, in the range $\Delta\xi \sim \pm 1$. The parameters r_0, r_1, and r_2 are calculated separately for quark and gluon jets [27], and are the results determined from an expansion in powers of $1/\sqrt{\tau}$ using the assumption that the number of effectively massless quarks N_f is 3, and keeping only the terms controlled by theory, the parameters are:

$$r_0^q = 1.75 - \frac{0.64}{\sqrt{\tau}}, \qquad r_1^q = \frac{1.6}{\tau^{3/2}}, \qquad r_2^q = -\frac{2.25}{\tau^2}, \tag{2--10}$$

$$r_0^g = 1.33 - \frac{0.28}{\sqrt{\tau}}, \qquad r_1^g = \frac{0.7}{\tau^{3/2}}, \qquad r_2^g = -\frac{1.0}{\tau^2}. \tag{2--11}$$

The theoretical prediction of the shape of the two-particle momentum correlation distribution function is shown in Fig. 2-5. The distribution has a ridge-like shape. Its central diagonal profiles $\Delta\xi_1 = \Delta\xi_2$ and $\Delta\xi_1 = -\Delta\xi_2$ have linear and parabolic shapes, respectively. The obvious features of the prediction are (1) the correlation should be stronger for particles with equal momenta $\Delta\xi_1 = \Delta\xi_2$, and (2) the strength of this effect should increase toward larger values of ξ (*i.e.* for softer particles).

Note that in the two-particle momentum correlation given by Eq. (2–8), K_{LPHD} simply cancels, suggesting that the correlation distributions for hadrons and partons are expected to be the same.

Until now, the two-particle momentum correlations were studied only by the OPAL collaboration in an e^+e^- environment at a center of mass energy of $\sim$ 91 GeV [30]. Charged particles in the full experimentally accessible solid angle were used in OPAL's analysis. This made it possible for OPAL to ignore some effects of jet reconstruction, but it clearly went beyond the range where the theory was valid. Strictly speaking, the theory controls parton shower development only within a small opening angle θ_c around the jet axis, so that $\tan\theta_c \sim \sin\theta_c \sim \theta_c$. OPAL's measured distributions showed a pattern in qualitative agreement with theory predictions, but the fitted values of the parton shower cutoff Q_{eff} (32 ± 2, 2^{+5}_{-1}, and 60^{+38}_{-27} MeV) were inconsistent with the Q_{eff} extracted

from fits of the inclusive momentum distributions (250 MeV) [31]. Fig. 2-6 shows the 3-dimentional momentum correlation distribution as measured by the OPAL collaboration. The same figure also shows six narrow bands for which correlation in data is compared to the analytical pQCD predictions. The results of the comparison in all six bands are shown in Fig. 2-7.

The NLLA correlation function from Eq. (2–8) entangles two effects: (1) multiplicity fluctuations of particles in a jet and (2) actual momentum correlations. In this analysis, we wish to measure purely momentum correlations. This can be achieved by introducing one- and two-particle momentum distributions normalized to unity:

$$D'(\xi) = \frac{D(\xi)}{\langle n \rangle}, \quad \int D'(\xi)d\xi = 1, \tag{2–12}$$

$$D'(\xi_1, \xi_2) = \frac{D(\xi_1, \xi_2)}{\langle n(n-1) \rangle}, \quad \int D'(\xi_1, \xi_2)d\xi_1 d\xi_2 = 1. \tag{2–13}$$

Then, the correlation function can be defined as:

$$C(\Delta\xi_1, \Delta\xi_2) = \frac{D'(\xi_1, \xi_2)}{D'(\xi_1)D'(\xi_2)} = \frac{\langle n \rangle^2}{\langle n(n-1) \rangle} R(\Delta\xi_1, \Delta\xi_2) = \frac{1}{F(\tau)} R(\Delta\xi_1, \Delta\xi_2), \tag{2–14}$$

where $F(\tau) = \frac{\langle n(n-1) \rangle}{\langle n \rangle^2}$ is the second binomial moment. The explicit dependence of the binomial moments on the energy scale for quark and gluon jets was taken from theory [32]:

$$F_q(\tau) = 1.75 - \frac{1.29}{\sqrt{\tau}}, \qquad F_g(\tau) = 1.33 - \frac{0.55}{\sqrt{\tau}}. \tag{2–15}$$

2.4.4 The k_T Distributions

The second topic addressed in this thesis are distributions of the transverse momenta of particles with respect to jet axis. This observable is of particular interest for us mainly

due to the fact that theoretical predictions obtain in the frameworks of MLLA [33] and NMLLA [34] were obtained fairly recently, allowing to make the first direct comparison of the CDF data to the results of the analytical QCD calculations. In addition, one may expect k_T distributions to be more sensitive to the hadronization effect than other observables described earlier in this chapter.

If the radiated parton with 4-momentum $(k_0, \vec{k})$ is emitted with an angle θ with respect to the direction of the jet, one has $k_T = |\vec{k}|sin\theta \approx k_0 sin\theta$. The inclusive k_T distribution is then defined as $\frac{dN}{d\ln k_T}$. In theory it is derived from the so called "double differential inclusive distribution", $\frac{d^2N}{d\ln(1/x)d\ln\theta}$, where $x = k_0/E_{jet}$. The validity range of the predictions is determined by two features of the calculation: a) the assumption that momentum of emitted parton is much less than jet energy (soft approximation), and b) the requirement for the double differential inclusive distribution to stay positive at all values of k_T within the range. The lower k_T boundary for the predictions is effectively Q_{eff}, the upper boundary depends on the order in which the pQCD calculation is done. In the MLLA case it is approximately $\ln(k_T) < \ln(Q) - 2.5$, while in the NMLLA case it is approximately $\ln(k_T) < \ln(Q) - 1.6$.

In theory distributions are normalized to the mean multiplicity of particles in a jet. The MLLA predictions for the mean particle multiplicities as a function of jet energy scale Q were compared to CDF data in earlier analysis and good agreement between data and theory was observed. The goal of this study is to compare the shape and not the absolute scale of the distributions. Consequently, they are normalized to the bin with $-0.2 < \ln(k_T) < 0.0$. Both theoretical prediction and experimental measurement are expected to be reliable for particles falling in this bin of $\ln(k_T)$. The general shape of the distribution and its evolution with increasing jet energy scale are shown in Fig. 2-8.

The results of the MLLA calculation predict distributions to have few very interesting features, namely very week sensitivity to the origin of the jet, being quark or gluon, and practically no dependence on the parton shower cutoff Q_{eff}. The dependence of the k_T distributions on jet origin and on the value of Q_{eff} is shown in Fig. 2-9. At the NMLLA level the dependence on jet origin becomes more prominent.

2.4.5 Mixing Quark and Gluon Jets

In theory, correlation functions and k_T curves are calculated for quark and gluon jets separately and denoted by $D_q(\xi)$ and $D_g(\xi)$, respectively. However, dijet events at the Tevatron consist of both quark and gluon jets. Therefore, in order to compare data to theory, we rewrite the formula for particle momentum distributions as follows:

$$D(\xi) = f_g D_g(\xi) + (1 - f_g) D_q(\xi), \qquad (2\text{--}16)$$

$$D(\xi_1, \xi_2) = f_g D_g(\xi_1, \xi_2) + (1 - f_g) D_q(\xi_1, \xi_2), \qquad (2\text{--}17)$$

where f_g is a fraction of gluon jets in the sample. After simple algebraic transformations, it can be shown that the momentum correlation Eq.(8) is reduced to the following:

$$C(\Delta\xi_1, \Delta\xi_2) = c_0 + c_1(\Delta\xi_1 + \Delta\xi_2) + c_2(\Delta\xi_1 - \Delta\xi_2)^2, \qquad (2\text{--}18)$$

where c_i coefficients $(i = 0, 1, 2)$ are:

$$c_i = \frac{f_g r^2}{f_g r^2 F_g + (1 - f_g) F_q} r_i^g + \frac{1 - f_g}{f_g r^2 F_g + (1 - f_g) F_q} r_i^q, \qquad (2\text{--}19)$$

where $r = \frac{\langle n_g \rangle}{\langle n_q \rangle}$ is the ratio of average multiplicities of partons in gluon and quark jets. The value of r enters in derivation of Eqs. (2–10),(2–11) [27], Eq. (2–15) [32] and Eq. (2–19).

In NLLA, this ratio, r_{theory} is equal to 9/4. Experimentally, the measured value of r_{exp} is 1.8 ± 0.2 [24]. The difference between these two values is used to evaluate the associated systematic uncertainty in our measurement of Q_{eff}.

For the inclusive k_T distributions the prescription for mixing is more straightforward. The distribution for a mixture is:

$$\frac{dN}{dln(k_T)} = f_g(\frac{dN}{dln(k_T)})_g + (1 - f_g)(\frac{dN}{dln(k_T)})_q \qquad (2\text{--}20)$$
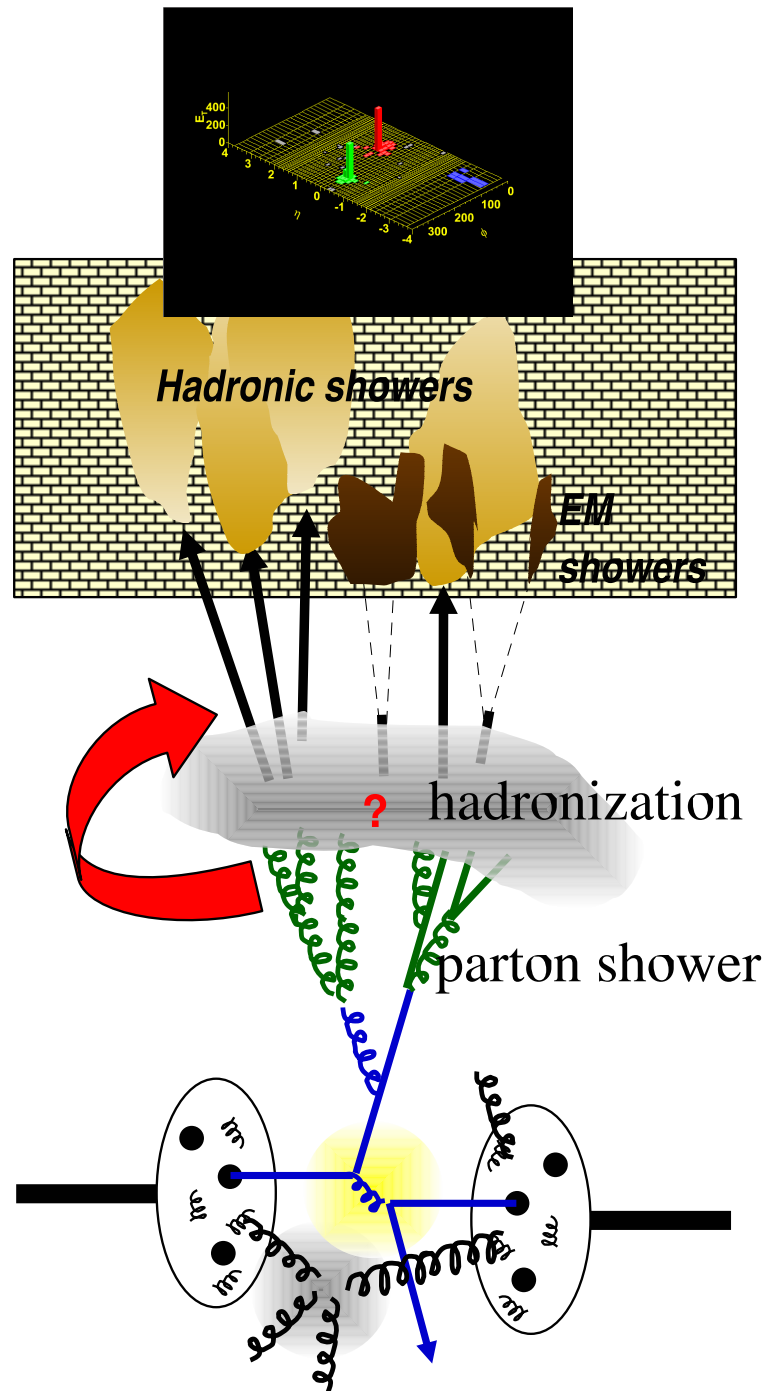
Figure 2-1. A cartoon description of the different levels of a jet event. The parton level is the state before partons hadronize, in theory this stage of an event can be described by the pQCD calculations. The hadron level is the state after hadronization. The transition (hadronization) is usually described using phenomenological models, and is mostly unexplored. The detector level is a result of the event as reported by the detector.
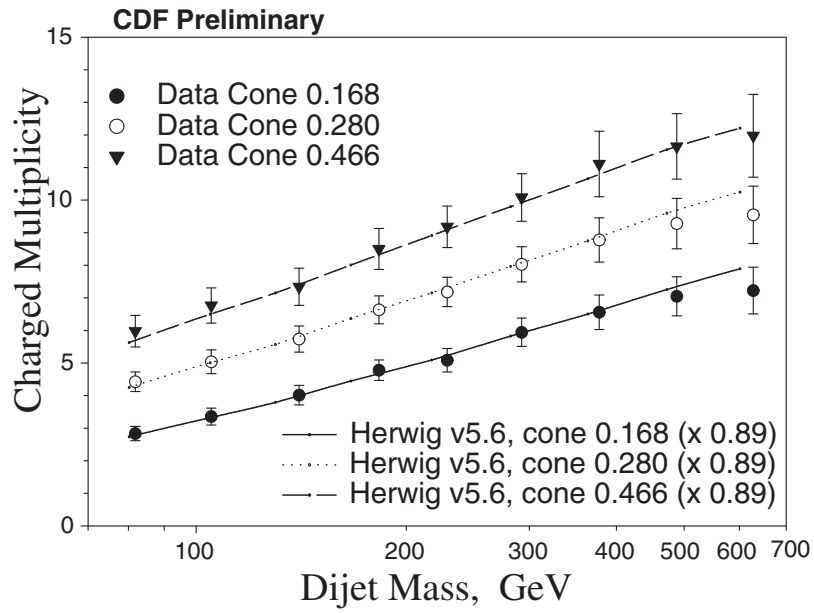
Figure 2-2. Inclusive multiplicity of charged particles within cones 0.168, 0.280 and 0.466 in dijet events. Data errors are completely dominated by correlated systematic errors. Fit for possible overall normalization to Herwig v5.6 predictions, yields $N = 0.89 \pm 0.05$. The level of the errors does not allow to claim the difference significant. Herwig predictions were scaled by a factor 0.89 and are shown on the plot (lines).
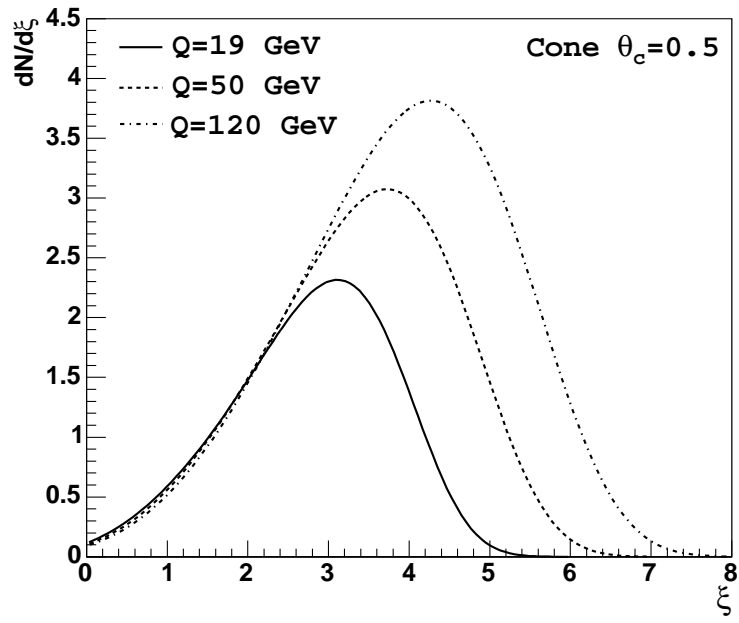
Figure 2-3. NLLA inclusive parton momentum distributions for $Q = 19, 50, 120$ GeV and $Q_{eff} = 230$ MeV as calculated by C.P. Fong and B.R. Webber.
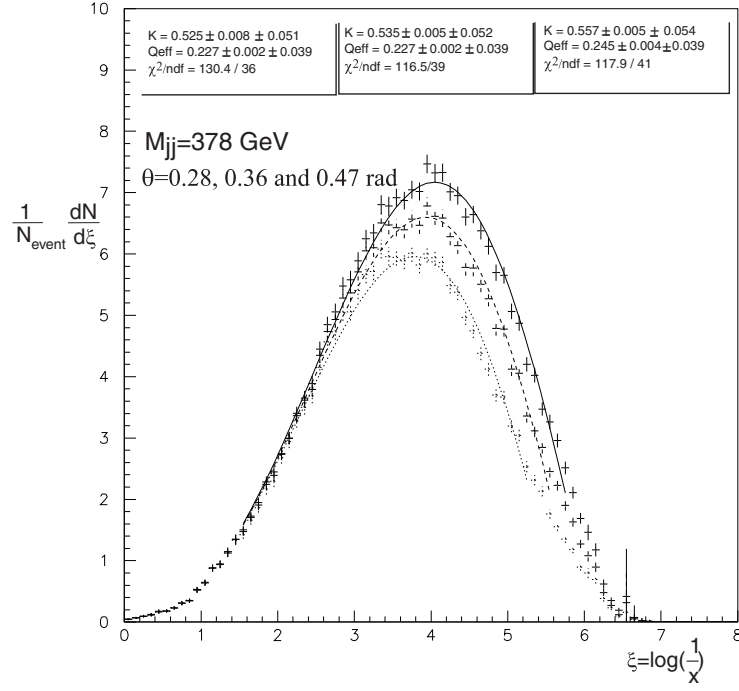
Figure 2-4. Inclusive momentum distribution of charged particles within restricted cones 0.466 in dijet events fitted with MLLA limiting spectrum. Dijet mass Mjj=378 GeV.

44
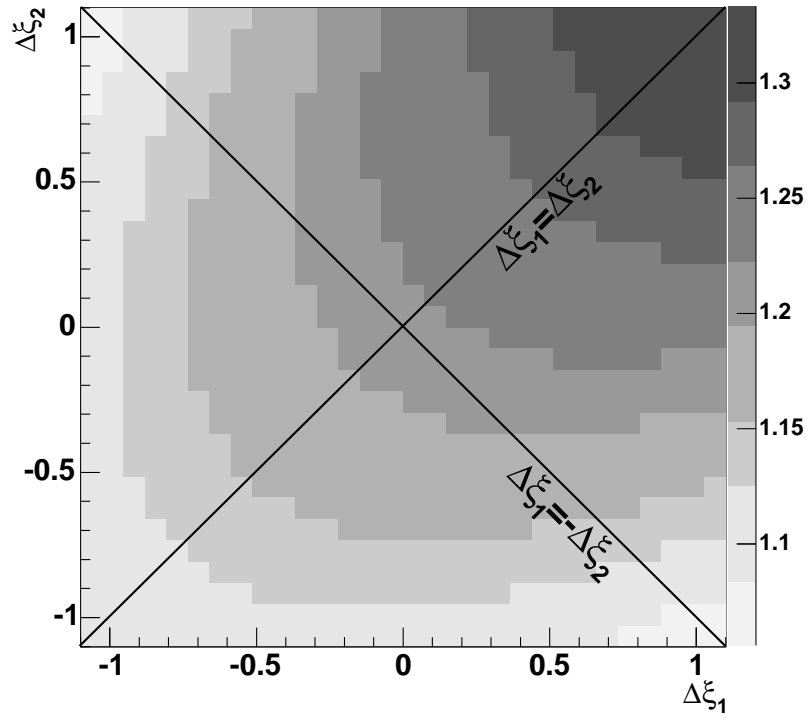
Figure 2-5. The NLLA patron momentum correlation function calculated for a gluon jet, $Q = 50$ GeV and $Q_{eff} = 230$ MeV as calculated by C.P. Fong and B.R. Webber.
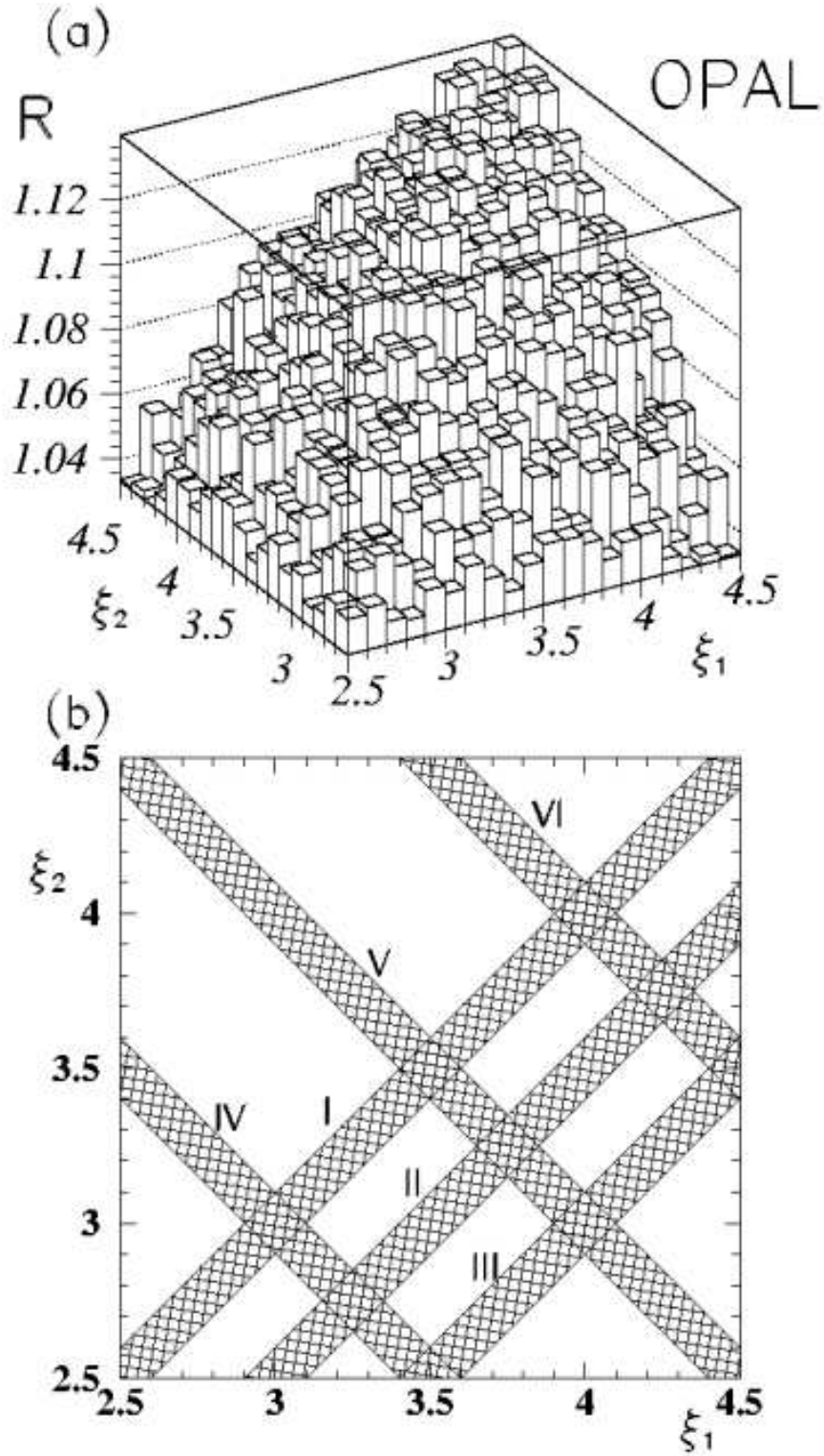
Figure 2-6. The 3-dimentional momentum correlation distribution as measured by the OPAL collaboration (top). Also shown are six narrow bands (bottom) for which correlation in data is compared to the analytical pQCD predictions.
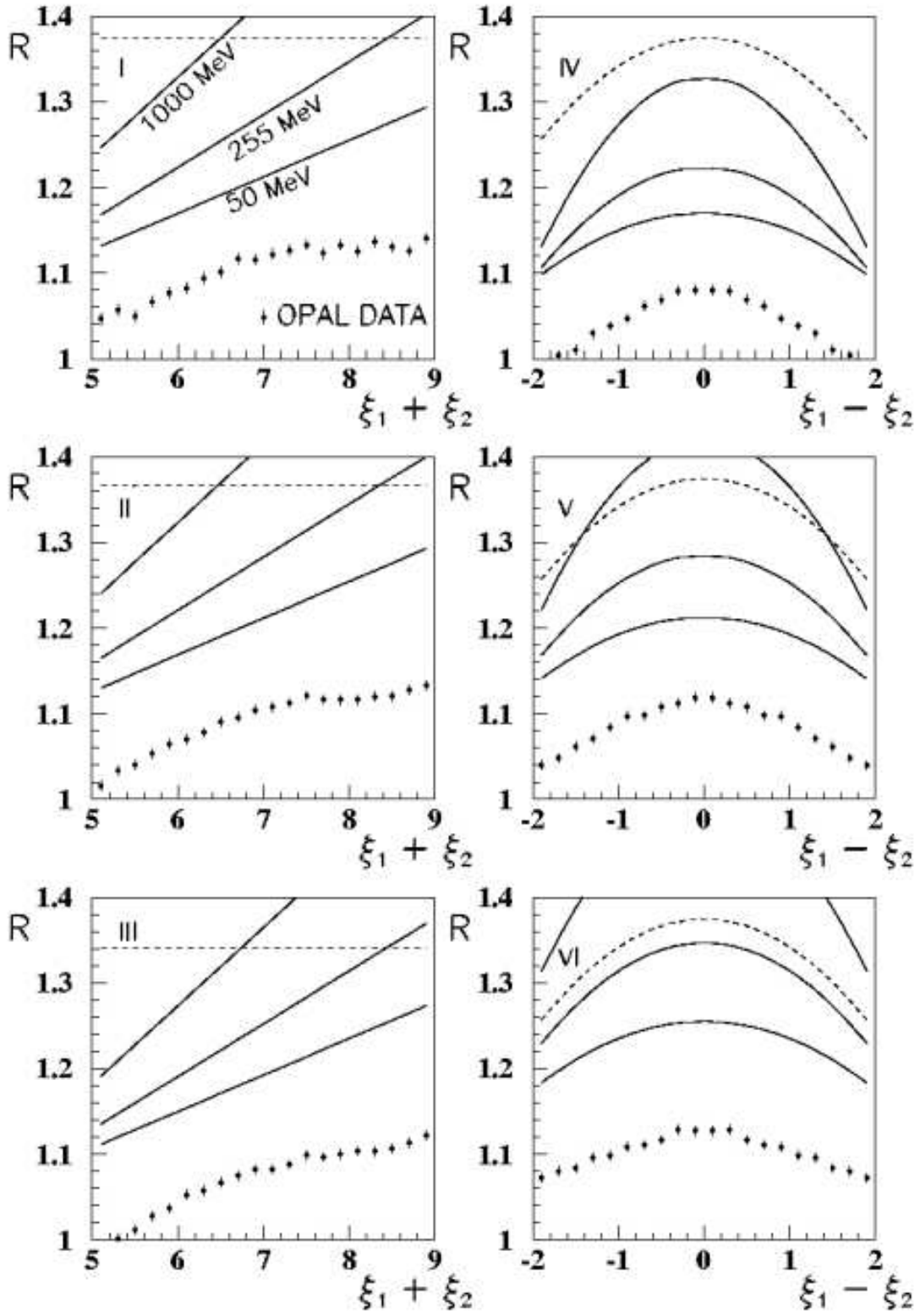
Figure 2-7. Comparison of the OPAL data to analytical QCD calculations. The three solid curves represent the next-to-leading QCD calculations for three values of Q_{eff}, 1000 MeV (highest), 255 MeV (middle), and 50 MeV(lowest). The dashed lines indicate the leading order QCD calculations for $Q_{eff} = 250$ MeV.
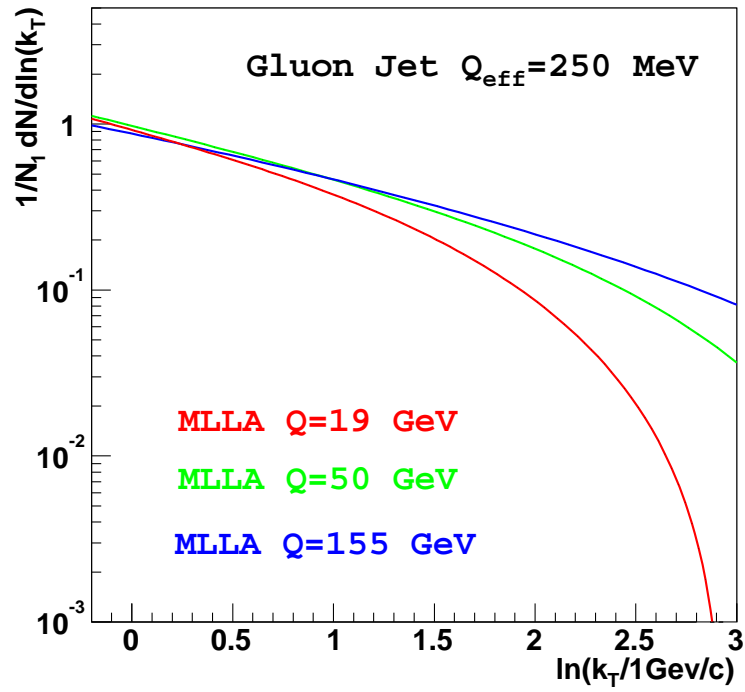
Figure 2-8. Inclusive k_T distribution of charged particles as predicted by the results of the MLLA calculations. The dependence of the predictions on jet energy scale is shown.
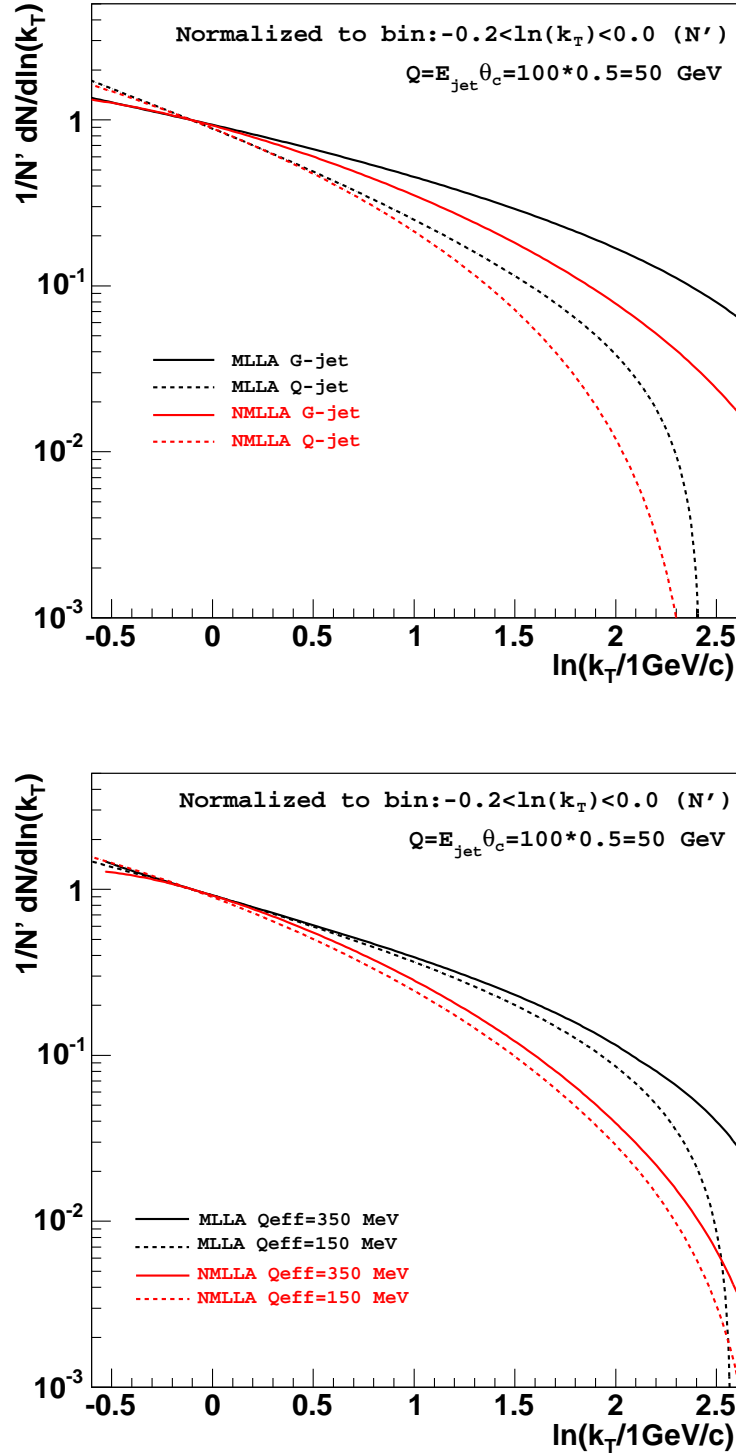
Figure 2-9. Inclusive k_T distribution of charged particles as predicted by the results of the MLLA and NMLLA calculations.[49] A) The dependence of the predictions on jet origin, quark or gluon, (top), and B) value of parton shower cutoff Q_{eff} (bottom) is shown.

CHAPTER 3
EXPERIMENTAL APPARATUS

In particle physics, high energies are needed both to create new and unstable particles and to explore the structure of hadrons. Until the early 1950s the only source of such high-energy particles was cosmic rays, and studies of them led to many important discoveries. However, cosmic rays now used only in special circumstances, and the overwhelming majority of experiments are conducted using beams of particles produced by machines called accelerators.

Fermi National Accelerator Laboratory (Fermilab or FNAL), located in Batavia near Chicago, Illinois is a U.S. Department of Energy national laboratory specializing in high-energy particle physics. It is the home of the highest energy particle accelerator in the world, Tevatron [35]. The Tevatron is a superconducting synchrotron that is four miles in circumference. At Tevatron bunches of protons and anti-protons collide at the center-of-mass energy of $\sqrt{s} = 1.96$ TeV. Top quark, the heaviest of six, was discovered at Tevatron. There is also a chance of discovering the hypothetical Higgs boson at Tevatron.

The collisions at Tevatron happen at two points. The Collider Detector at Fermilab (CDF) is a multipurpose detector positioned at one of the two Tevatrons collision points (the D0 detector is positioned at another interaction point). CDF is also an international collaboration of about 600 physicists (from about 30 American universities and National laboratories and about 30 groups from universities and national laboratories from Italy, Japan, UK, Canada, Germany, Spain, Russia, Finland, France, Taiwan, Korea, and Switzerland). The CDF detector itself weighs 5000 tons and is about 12 meters in all three dimensions.

In this chapter we give a brief overview of the accelerator chain and the CDF II detector used to collect the data for the measurements.

3.1   Accelerator

The Fermilab accelerator chain allows to accelerate particles (protons and anti-protons) to the energy of 980 GeV. The chain consists of several individual components: Proton Source (Cockcroft-Walton, Linac and Booster), Main Injector, Antiproton Source (Debuncher, Accumulator and Recycler) and the Tevatron. The schematic picture of the Fermilab accelerator chain is shown in Fig. 3-1.

3.1.1   Proton Source

The process leading to the $p\bar{p}$ collisions begins with hydrogen atoms, used to create protons. The atoms are taken from the ordinary cylinder of compressed hydrogen gas (H_2). The bottle contains 5×10^{25} hydrogen atoms. If the Fermilab chain of accelerators ran "flat out" it could accelerate 10^{20} protons each year. So the gas in the bottle could last 500,000 years!! In fact, due to inefficiency in the ion source, it is replaced about once per year.

Hydrogen atoms consist of a proton and an electron. The atoms are placed in an electric field to strip away electrons and create positively charged ions H^+. The protons then will congregate on metal surface with cesium. The metal has free electrons and the cesium makes it easier to "steal" electrons from metal. If the proton gets two electrons from the metal, it becomes negatively charged (H^-) and is forced away from the surface. The acquired atoms are then accelerated to 750 keV by a Cockcroft-Walton electrostatic generator.

The next component in the chain is a 150 m linear RF accelerator (the Linac) which boosts their energy to 400 MeV. The beam here is bunched instead of a continuous ribbon

of beam that is in the Cockcroft-Walton. Due to its RF nature, in the Linac there must be "dead" spaces, where there is no beam. These "dead" spaces coincide with where the electric field is pointing in the wrong direction. The first half-length of the Linac is the Drift Tube Linac, which accelerates the ions to 116 MeV. The second half of the Drift Tube Linac has been replaced with a Side-coupled Cavity Linac, allowing ions to achieve an ultimate energy of 400 MeV. After the Linac, the H^- ions are passed through a graphite foil which strips them of their electrons and leaves the bare protons

The protons are injected into the Booster, a rapid cycling synchrotron about 150 meters in diameter. Dipole magnets steer the beam of protons so that they travel in a circle while quadrupole magnets focus the beam by successively squeezing it along both axes perpendicular to the direction of the beam. Once the bare protons are collected in the Booster, they are accelerated to an energy of 8 GeV by the RF cavities. The protons travel around the Booster approximately 16,000 times with revolution period of 2.22 ms before they get transfered to the Main Injector.

3.1.2 Main Injector

In Run I, the protons and antiprotons were injected into the Tevatron by the Main Ring, another synchrotron built in the early 1970's. However, the Main Ring was not designed to serve as an injector, therefore imposing certain limits on the performance of the Tevatron. In Run II, Fermilab upgraded its accelerator complex with the Main Injector, the primary functions of which are to provide 120 GeV protons for the Antiproton Source and to accelerate protons and antiprotons from 8 to 150 GeV. Since protons and antiprotons have opposite charge, the Main Injector can accelerate both particles moving in opposite directions simultaneously. It also accepts 150 GeV antiprotons from the Tevatron and decelerates them to 8 GeV for transfer to the Recycler.

The Main Injector is a synchrotron 3.3 km in circumference. It accelerates protons to *flat top* (maximum energy for a given machine at which particles can be kept for a long time) of 150 GeV, combines them into bunches of roughly 27×10^{10} and injects these bunches into the Tevatron. Thirty-six of them are needed to fill the Tevatron. Once Tevatron is filled with protons, the Main Injector returns to the process of antiproton production.

3.1.3 Antiproton Source

The rate of the antiproton production is the main limitation to the performance of Tevatron. As it was mentioned in the previous section, antiproton production is one of the Main Injector's primary tasks. Some of the 120 GeV protons from the Main Injector are guided to impact a nickel target. This impact produces many particles, antiprotons are produced with an effective efficiency of 10^{-5}. The antiprotons leave the target at a wide range of energies, positions and angles. This randomness is equivalent to temperature so we say that the beam coming off the target is "hot". This "hot" beam will have a difficult time fitting into a beam pipe of reasonable dimensions. *Stochastic cooling* is a technique that is used to remove the randomness of the "hot" beam on a particle by particle basis. Stochastic Cooling systems are used in both the Debuncher and the Accumulator. The antiprotons are isolated and injected into the Debuncher, where their bunches are spread to form a continuous beam. The beam size and its momentum spread are then reduced in a stochastic cooling process, where the trajectory of the beam is measured on one side of the Debuncher and corrected on the other.

The antiproton beam is then injected into the Accumulator, the purpose of which is to accumulate the antiprotons. There the beam is more thoroughly stochastically cooled for several hours, until the maximum Accumulator intensity is reached or the

Tevatron needs to be refilled. Then these antiprotons are divided into bunches and injected backward into the Main Injector at 8 GeV. In the Main Injector, antiprotons are accelerated from 8 GeV to 150 GeV and subsequently injected into the Tevatron.

It was mentioned earlier that antiprotons are difficult to produce and accumulate. Therefore, the efficient use of created ones is ones is of highest importance. The last component of the antiproton source, the Recycler, was included in the Fermilab program in 1997 and commissioned in 2004. It is a fixed-energy storage ring placed in the Main Injector tunnel directly above the Main Injector beam-line. The purpose of the Recycler is to further increase the luminosity of the Tevatron over the luminosity goals of the Main Injector by itself. Before it was built, the precious antiprotons left at the end of a collider store were thrown away. The Recycler made it possible to recover these antiprotons and re-use them in a later store. It also functions as a post-Accumulator ring. As the stack size in the Accumulator ring increases, there comes a point when the stacking rate starts to decrease. By emptying the contents of the Accumulator into the Recycler periodically, the Accumulator is always operating in its optimum antiproton intensity regime. The Recycler is a high reliability storage ring for antiprotons. Because there are few power sensitive components, there are virtually no mechanisms for inadvertent beam loss.

3.1.4   Tevatron

Tevatron is the final component of the acceleration process, it is currently the highest energy hadron collider in the world. The Tevatron accelerates beams of protons and antiprotons to the energy of 980 GeV, providing a center of mass energy of 1.96 TeV. It is also the worlds first superconducting synchrotron. There are about 1000 superconducting magnets in the Tevatron, requiring the world's largest cryogenic cooling system and, consequently, huge amounts of liquid helium.

The circumference of the Tevatron is 6.28 km. The protons are accelerated by RF cavities in the clockwise direction and antiprotons in the counterclockwise direction. Each of the beams (proton and antiproton) are divided into three "trains", each containing 12 bunches. The time separation between bunches is 396 ns. Each bunch "train" is followed by a gap called "abort gap". These gaps are used to remove the beam from the Tevatron without producing any damage. The beam configuration is illustrated in Fig. 3-2. The antiprotons are usually injected after the protons and their bunch ensemble is the mirror image of the proton spacing.

The number of events for a particular process at a given center-of-mass energy depends upon the cross section of this process and the instantaneous luminosity (i.e. the intensity of colliding proton and antiproton beams) integrated over the total data taking period. The instantaneous luminosity is defined:

$$L = \frac{N_B N_p N_{\bar{p}} f}{2\pi(\sigma_p^2 + \sigma_{\bar{p}}^2)},\tag{3-1}$$

where N_B is the number of bunches; N_p and $N_{\bar{p}}$ are number of protons and antiprotons per bunch, respectively; f is the bunch revolution frequency; and σ_p and $\sigma_{\bar{p}}$ are the average cross-sectional areas of the bunches. Making σ_p, $\sigma_{\bar{p}}$ smaller and N_p, $N_{\bar{p}}$ larger increases the rate of collisions.

The effort is made to maximize the probability of proton-antiproton collisions at two precise locations: CDF and D0 detectors. It is achieved by focusing the beams directly before impact, using the so called low-beta quadrupole magnets. The instantaneous luminosity is highest at the beginning of Tevatron stores and gradually decreases with time. After some time (20 hours on average) the luminosity becomes very low, the store is

being terminated and a new cycle starts. To day, the longest store at the Tevatron lasted for almost 54 hours.

Summary of the current Tevatron performance characteristics is given in Table 3-1. The total integrated luminosity measured at CDF is shown in Fig. 3-3 from the beginning of Run II which started in April 2001. The live luminosity, which excludes integrated luminosity during all the detector dead-times is also shown. The peak instantaneous luminosity recorded is 285×10^{30} cm^{-2}s^{-1}. The design goal for the Tevatron is to collect 8 fb^{-1} by the end of 2009.

3.2   The CDF II Detector

Data used in the measurements were recorded with the CDF Run II detector [36]. The detector was designed for precision measurements of the energy, momentum and position of particles produced in proton-antiproton collisions. Significant upgrades to the detector were made since Run I to adjust it to the increased collision rate and center-of-mass energy. The detector is roughly cylindrically and backward-forward symmetric around the beam axis. It is about 10 meters high, extends about 27 meters from end to end, and weights over 5000 tons. The layout of CDF is shown in Fig. 3-4.

The coordinate system used at CDF is right-handed: the $\hat{z}$ axis points along the direction of the proton beam, the $\hat{x}$ axis is in the plane of the accelerator ring, pointing radially outward, and the $\hat{y}$ axis points vertically up. The center of the detector roughly coincides with the center of the beam crossing region.

Due to the symmetry of the detector, it is sometimes more convenient to use polar (r, θ, ϕ) coordinate system. In this case the polar angle θ is counted from the positive direction of the $\hat{z}$ axis. The azimuthal angle ϕ runs in the transverse $(x - y)$ plane ,

56

with $\phi = 0$ being the positive direction of the $\hat{x}$ axis. Commonly, θ is replaced by the pseudo-rapidity, (η):

$$\eta = -\ln\tan(\frac{\theta}{2}). \tag{3–2}$$

The choice of η instead of θ is motivated by the fact that the actual colliding particles are partons, carrying only some fraction of protons and antiprotons energy, often with imbalanced longitudinal components of the momenta. This leads to large boosts in the observed physics interactions. The quantity called the rapidity:

$$\zeta = \frac{1}{2}\ln\frac{E + p_z}{E - p_z} \tag{3–3}$$

is invariant under Lorentz transformations. In the ultra-relativistic/massless particle limit, the rapidity can be replaced by the pseudo-rapidity.

CDF takes a multi-layer approach to measure a wide variety of particle interactions, and it consists of the few major detector components. From the inside out there are: tracking system, magnet, electromagnetic and hadronic calorimetry and muon detectors. There is also the Time-of-Flight (TOF) system, expanding CDF's particle identification capability in the low transverse momenta region; and the Cherenkov Luminosity Counter (CLC) designed to measure instantaneous luminosity at CDF. In the next sub-sections we give a general description of the CDF detector components with an emphasis on those relevant to the measurements described in this dissertation. Throughout this document we omit the "II" part of "CDF II". There is no ambiguity, because we always speak of the Run II incarnation, unless the opposite is explicitly stated.

3.2.1 Tracking and Vertexing Systems

CDF tracking and vertexing systems are contained within a superconducting solenoid, 5 meters in length and 3.2 meters in diameter, which supports a 1.4 T magnetic field oriented parallel to the $\hat{z}$ axis. Charged particles cause ionization as they pass through matter, the ionization is typically localized near the trajectory of the particle in little clusters called hits. The tracking systems at CDF locate charged particles in space by sampling the deposited electrical charge due to ionization along the particle trajectory. The process is called tracking. Due to the magnetic field, electrically charged particles produced in the collisions follow a helical trajectory. The particle momentum in the $x - y$ plane and its electric charge are determined by observing the radius of curvature of the helix and its orientation relative to the magnetic field.

For many analysis it is critical to determine the point of origin of a particle. It cannot be obtained from a helix alone, all we know is that it is somewhere on the helix. Normally the point of origin is determined by intersecting the helix with at least one other helix corresponding to a particle which we believe has come from the same space point as a result of a decay of common parent particle. This process is called vertexing.

CDF tracking system consists of two major components. These are the Central Outer Tracker (COT) and the silicon detectors: Layer00 (L00), Silicon Vertex Detector (SVX), and Intermediate Silicon Layers (ISL). Combined, these systems provide coverage up to $|\eta| < 2.0$. The schematic of one quadrant of the CDF tracking system is shown in Fig. 3-5. The components are described in details below.

Central Outer Tracker

The Central Outer Tracker (COT) [37] is an anchor of CDFs tracking system. It is a cylindrical open-cell drift chamber with a large tracking volume, designed to measure the three-dimensional trajectories of charged particles in the central region, $|\eta| < 1.0$. The COT occupies the radial region 40 to 138 cm, and measures 310 cm along the $\hat{z}$ axis. It is filled with with fast gas (50% argon, 50% ethane) to make drift times small enough so that the hits can be read out between each Tevatron bunch crossing.

The basic element of the COT is the *cell*, which spans the length of the COT. Within each cell are high-voltage field panels, potential wires and shaper wires which serve to support a regular electrostatic field. Charged particles traveling through the gas mixture leave a trail of ionization electrons. These electrons drift toward the sense wires by virtue of the electric field created by the field panels and potential wires. Because of the magnetic field along the $\hat{z}$ axis, the drift is not in the direction of the electric field. In such crossed fields electrons move in the plane perpendicular to the magnetic field and at an angle α with respect to the electric field. The values of α depends on the magnitude of both fields and the gas properties, in the COT it is $\alpha \sim 35°$. Since the electron drift velocity is known, the position of the track can be accurately measured by simply recording the time of the resulting current on the sense wires. A transverse view of a typical cell with the positions of individual wires is shown in Fig. 3-6.

The cells of the COT are arranged into eight radially spaced superlayers. Four of them have their wires arranged parallel to the $\hat{z}$ axis, allowing track measurements in the $r - \phi$ plane. Other four superlayers have their wires tilted by 2° allowing to record stereo information, track measurements in the $r - z$ plane. The superlayer geometry is shown in Fig. 3-7. The hit position resolution of COT is approximately 140 μm, which translates into the transverse momentum resolution $\frac{\delta p_T}{p_T} \sim 0.0015 \frac{p_T}{GeV/c}$.

59

Silicon Detectors

The volume surrounding the beam-pipe is occupied by three silicon detector systems: Layer 00 (L00), Silicon Vertex Detector (SVX) and the Intermediate Silicon Layers (ISL) [37]. The primary purpose of the silicon detectors is to provide excellent spatial resolution for the charged-particle tracks. This is crucial for reconstruction of the displaced secondary vertexes, and, therefore, identification of b jets.

The principle on which the silicon tracking is based is somewhat similar to that of the drift chamber. When a charged particle goes through the silicon, it ionizes the atoms, producing electrons and holes - the remaining silicon atoms missing an electron. In the electric field electrons travel to one side and the holes in the other, leaving an electric signal that can be recorded. Due to the narrow width of the strips, the silicon detectors have much better resolution than COT. To provide excellent spacial resolution silicon detectors have to be positioned as close to the beam as possible, imposing an additional requirement, that the detector should be able to withstand large doses of radiation in the region close to the beam-pipe.

Layer 00 is a single-sided radiation hard silicon microstrip detector. It is mounted directly on the beam pipe, at the inner radius of 1.15 cm and an outer radius of 2.1 cm, so as to be as close as possible to the interaction point. L00 is designed to enhance the track impact parameter resolution (the impact parameter d_0 is defined as the shortest distance in the $r - \phi$ plane between the interaction point and the trajectory of the particle obtained by the tracking algorithm fit). There are six readout modules with two sensors bonded together in each module.

The Silicon Vertex Detector is composed of five layers of double-sided silicon microstrip detectors, it covers radial coverage from 2.5 to 10.7 cm. SVX is built in

three cylindrical barrels each 29 cm long. One side of each microstrip detector provides tracking information in the $r - \phi$ plane, the other side provides tracking information in the $r - z$ plane, therefore SVX can reconstruct three-dimensional tracks. Three of the five SVX layers provide 90° stereo information, two SVX layers provide ±1.2° small-angle stereo information. The total number of channels in the system is 405,504. The SVX bulkhead design is shown in Fig. 3-8.

The primary goal of the SVX is to detect secondary vertices from heavy flavor decays. The secondary goal is to maximize tracking performance by combining the COT and SVX hit information. The alignment of the SVX detector is very important for the track reconstruction, every effort is made to position the SVX barrels in a coaxial manner. The process of combined COT and SVX track reconstruction [38] starts in COT. After COT-only track is reconstructed, it is extrapolated through the SVX. Because the track parameters are measured with uncertainties, the track is more like a tube of certain radius, determined by the errors on tracks parameters. At each SVX layer, hits that are within a certain radius are appended to the track and the re-fitting is performed to obtain the new set of parameters for the track. In this process there may be several track candidates associated to the original COT-only track. The best one in terms of the number of hits and fit quality is selected at the end.

The impact parameter resolution of the SVX is about 40 μm. The resolution in z is about 70 μm.

In the central region, a single ISL layer is placed at a radius of 22 cm. In the plug region, $1.0 < |\eta| < 2.0$, two layers of silicon are placed at radii of 20 cm and 28 cm. ISL improves the tracking coverage in the forward region of the detector. This system is useful for matching tracks within the COT to those within the SVX. Double sided silicon is used

in the ISL, the single hit resolution is about 16 μm on the axial side and about 16 μm on the stereo side.

3.2.2 Calorimetry

The purpose of the calorimeters is to measure the energy of particles producing electromagnetic (photons and electrons) and hadronic (hadrons) showers as they transverse and interact with regions of dense material. CDF uses sampling calorimeters, with dense absorbers interleaved with layers of active scintillator. Wavelength-shifting fibers (WLS) are embedded within the layers of scintillator and transmit the scintillator light via acrylic light guides to photomultiplier tubes (PMTs) located at the tops of the towers. Integrating the charge collected by the PMT gives a measure of the energy deposited in the calorimeter.

The systems cover 2π in azimuth and the pseudorapidity region $|\eta| < 3.6$. The calorimeters are segmented into projectile towers (Fig. 3-9).

The calorimetry detectors at CDF [37] are mechanically subdivided into three regions: central, wall and plug. They are located just outside the solenoid magnet in the central region, and just outside the tracking volume in the plug region. The electromagnetic and hadronic components are called the Central Electro-Magnetic (CEM), Central Hadronic (CHA), Wall Hadronic (WHA), Plug Electromagnetic (PEM) and Plug Hadronic (PHA) calorimeters.

The CEM is divided into 15° wedges is azimuthal angle ϕ and into ten η towers subtending 0.1 units of pseudorapidity. In consists of alternating 1/8 inch absorber layers, made of aluminum-cled lead, and 5 mm layers of polystyrene scintillator, for a total depth of 18 radiation lengths of material. Embedded in the CEM at the approximate depth of maximum shower development are proportional wire chambers, Central Electromagnetic

62

Strip (CES). With the position resolution of 2 mm, they contribute to $e^{\pm}/\gamma$ identification, using the position measurement to match with tracks. A second set of proportional chambers, the Central Preshower (CPR), is located between the CEM and the magnet coil, and provide greatly enhanced photon and soft electron identification.

The CHA consist of alternating layers of iron absorber and naphthalene scintillator. They are segmented to match the CEM towers, 0.1 units of pseudorapidity per tower and 15° of azimuth per wedge, with a total thickness of 4.7 nuclear interaction lengths. The WHA is designed to compensate the limited forward coverage of the CHA, and covers the region $0.7 < |\eta| < 1.3$. It is also iron/scintillator based with the thickness of 4.5 nuclear interaction lengths.

The CDF plug calorimeters are similar in concept to the central calorimeters. They also have electromagnetic and hadronic component, as well as preshower and shower maximum detectors. The details of implementation, however, are slightly different. The segmentation is variable: in the lower η (less forward) region the plug calorimeters have 48 wedges, each subtending 7.5° in ϕ; in the higher η (more forward) region they have 24 wedges, each subtending 15° in ϕ. The segmentation in η also varies from 0.1 to 0.15 units of pseudorapidity. The PEM alternates layers of lead with 4 mm layers of scintillating tiles, for a total of 21 radiation length at normal incidence. The first layer of scintillating tiles act as a preshower detector, Plug Preshower (PPR). At the position of maximum shower development is located a shower position detector (PES) made of scintillating strips. The PHA calorimeter alternates layers of iron with scintillating tile for a total depth of about 7 interaction length.

The measure of calorimeter performance is its resolution. Summary of CDF calorimeter characteristics, including the resolution, is given in Table 3-2.

3.2.3   Other Systems

Muon Detectors

Muons have low bremsstrahlung radiation (due to their relatively large mass), and are not subject to strong interaction with atomic nuclei. Thus, they can penetrate much more material than any other charged particle. In CDF, the muon detectors are placed behind the calorimetry and are generally the outermost detector systems, separated from the rest of the detector by steel shielding.

CDF uses four systems of scintillators and proportional chambers in the detection of muons over the region of $|\eta| < 2$ [37]: Central Muon Detector (CMU), Central Muon Upgrade (CMP), Central Muon Extension (CMX) and Intermediate Muon Detector (IMU). The CDF muon detectors consist of stacked argon-ethane drift tubes, some backed up with scintillator counters. Muons which pass through the drift tubes leave a trail of ionized gas along their trajectory; muons which pass through the scintillation panels induce light pulses which are collected by PMTs.

The CMU detector consists of four layer drift chamber directly behind the hadronic calorimeter. The layers are divided into rectangular drift cells each with a single sense wire. The detector covers $|\eta| < 0.6$ and detects muons with a minimum p_T of 1.4 GeV/c. The CMP sits behind an additional 60 cm layer of steel and is also composed of four layers of individual drift cells covering $|\eta| < 0.6$. The CMP detects muons down to p_T of 2.2 GeV/c. The CMX, composed of conical sections of drift chambers and scintillation counters , extends the muon $|\eta|$ coverage from 0.6 to 1.0, while measuring muons with a minimum p_T of 1.4 GeV/c. Finally, the IMU, which was a part of CDF Run II upgrade,

extends muon coverage out to $|\eta| < 1.5$. The IMU is also composed of drift cells and scintillator counters, detects muon with minimum transverse momentum $1.4 - 2.0$ GeV/c.

Having a track segment (stub) in the muon chambers is not sufficient for muon detection. Stubs can be due to a hadronic punch-through or just noise in the electronics. Only if a stub matches a certain track measured by the COT then the two are combined to make a muon.

Cherenkov Luminosity Counter

The purpose of the Cherenkov Luminosity Counter (CLC) [39] at CDF in Run II is to measure the luminosity. CLC successfully provides precise measurements at current peak instantaneous luminosities of $\sim 3 \times 10^{32}$ cm^{-2}s^{-1}.

The CLC utilizes the effect known as Cherenkov radiation. When a charged particle travels in a medium faster the speed of light in this medium (*i.e.* when $\beta = v/c > 1/n$, where n is the refraction index of the medium), it starts emitting light into a cone around its direction. Cone's opening angle depends on the ratio of the two speeds and the refraction index.

The detector consists of two modules (East and West) located within the "3-degree holes" inside the forward and backward calorimeters, it covers pseudorapidity range $3.75 < |\eta| < 4.75$. Each CLC module consists of 48 long and thin Cherenkov counters, filled with isobutane at pressure 1.5 times larger than atmospheric. The use of isobutane was motivated by its large index of refraction and good transparency for photons. The counters point toward the interaction region as shown schematically in Fig. 3-10. They are arranged around the beam-pipe in three concentric layers, 16 counters in each. This arrangement allows to make the detector much more sensitive to the particles coming

directly from the interaction point because they transverse the full length of a counter and generate a large amount of light, which is read out by a photomultiplying tube. Particles coming from secondary interactions with material and from beam-halo interactions pass through the counters at large angles, producing significantly smaller signal than that of primary particles.

The luminosity is measured using the following relation between the instantaneous luminosity L and the number of primary interactions per bunch crossing μ:

$$\mu \cdot f_{BC} = \sigma_{p\bar{p}} \cdot L, \qquad (3\text{--}4)$$

where $\sigma_{p\bar{p}}$ is the total $p\bar{p}$ cross-section at $\sqrt{s} = 1.96$ TeV, and is known relatively well; and f_{BC} is the rate of bunch crossings in the Tevatron.

Therefore, in order to obtain the value of instantaneous luminosity one has to measure μ. At CDF this is done by counting "empty" bunch crossings, *i.e.* bunch crossings with zero primary interactions. The number n of primary interactions per bunch crossing follows Poisson statistics with mean μ:

$$P_n(\mu) = \frac{\mu^n e^{-\mu}}{n!}. \qquad (3\text{--}5)$$

The probability of having an empty bunch crossing is then:

$$P_0(\mu) = e^{-\mu}. \qquad (3\text{--}6)$$

Thus, measurement of the probability of having an empty crossing is enough to determine the average number of interactions μ, and, consequently, the value of instantaneous luminosity. This probability is measured by dividing the number of empty crossings (corrected for the detector acceptance) by the total number of bunch crossings in a certain

66

time interval. For a crossing to be considered empty there should be no hits in either East or West CLC modules. The disadvantage of this method is that at very high luminosities the probability of having an empty crossing is small, making it difficult to maintain good precision.

Time-of-Flight

The Time-of-Flight system (TOF) expands CDFs particle identification capability in the low p_T region. TOF measures arrival time t of a particle with respect to the collision time t_0. The particle mass m is then determined using the relation:

$$m = \frac{p}{c}\sqrt{\frac{(ct)^2}{L^2} - 1},$$
(3–7)

where L is the path length and p is the momentum measured by the tracking system.

TOF has cylindrical geometry with 2π coverage in ϕ and roughly $|\eta| < 1$ in pseudorapidity. It consists of 216 scintillator bars installed at a radius of about 138 cm in the 4.7 cm space between the outer shell of the COT and the cryostat of the superconducting solenoid. The complete description of the TOF detector can be found in [40].

3.2.4 Trigger System and Data Acquisition

Bunch crossings at the Tevatron occur every 396 ns, a rate of 2.5 MHz. Since data can be written to tape at a rate of $\sim$75 Hz, there needs to be a system that allows to select quickly the most interesting events. CDF uses a three level trigger system, the data flow through it is schematically shown in Fig. 3-11. The elaborate description of the entire system is given in [37].

The Level-1 (L1) is a synchronous system with an event read in and an accept or reject decision made every bunch crossing. Within the DAQ electronics of each detector component, there is a 42 "bucket" data pipeline. The pipeline is synchronized with the Tevatron master clock, which has a period of 132 ns. Event data from each proton-antiproton bunch crossing enters the pipeline. A decision must be made before the data reaches the end of the pipeline, otherwise the data is lost. The decision time for L1 is 5.5 μs and it is based on the data from the calorimeters, the COT and the muon chambers. The calorimeter stream decision is based upon the energy deposited in calorimeter towers, along with the magnitude of unbalanced transverse energy. The Extremely Fast Tracker (XFT) [41] uses information from the COT to reconstruct tracks, events are accepted or rejected based on the track multiplicity and transverse momenta. The muon stream uses information from the XFT to match tracks to hits in the muon chambers to produce muon candidates. The maximum accept rate for L1 trigger is 20 kHz, a factor of few hundred smaller than the input rate of 2.5 MHz.

Events which meet the requirements of the L1 trigger are passed to the Level-2 (L2). At L2, an event is written into one of four buffers within the DAQ electronics for each detector component. These buffers are different from the data pipeline used in L1, the data here remains in the buffer until the decision is made. While event data are being processed, they cannot be overwritten by another event from L1. If an L1 accept occurs while all four L2 buffers are occupied, the deadtime is incurred. In order to minimize deadtime, the latency of the L2 decision must less than approximately 80% of the average time between L1 accepts. Therefore, the L2 latency is designed to be 20 μs. To make a decision, L2 uses information from L1 as well as additional data from the shower maximum strip chambers (CES) in the central calorimeter and the $r - \phi$ strips of SVX.

L2 extends XFT tracks inside the SVX volume and adds the measurement of the track impact parameter d_0. Significant impact parameter indicates a displaced vertex, which is an extremely powerful signature. The maximum accept rate for the L2 trigger is 300 Hz.

The Level-3 (L3) trigger uses the entire detector data and consists of two components: the Event Builder and the processing farm. The read out event fragments are put in the proper order by the custom hardware system, called the Event Builder. Then, the arranged event fragments are channeled to a farm of conventional PCs running Linux. The farm consists of multiple sub-farms, each having one head node and 12-16 processor nodes. The head nodes receive ordered sequence of event fragments from the Event Builder and assemble those fragments into a block of data, called the event record. This event record is suitable for analysis by CDF software and from then becomes one and the only piece of information about a particular event. The L3 takes advantage of full detector information, a decision is made based upon detailed particle identification and event topology. The accept rate for the L3 trigger is approximately 75 Hz.

3.2.5 Good Run Requirements

The data passing the L3 trigger is being segmented into ten streams and written to tape in real time. However, not all of it is suitable for physics analysis. For this reason, good run requirements are established to determine which data runs should be used by physics groups and which are not. A run is defined as a continuous period of data taking without resetting the DAQ system. For a run to be marked "good", all detector components and their readout should operate properly during the run. If one (or more) of detector components is experiencing problems, a "bad" flag is set. The run can still be used in physics analysis, but only if the analysis does not need data from the problematic component. It is up to the CDF shift crew to decide which flag should be set to a run.

69

3.3 Jet Reconstruction

In theory, a "jet" is a collection of soft partons originating in a process of soft gluon showering by a primary parton. Quarks and gluons produced in high-energy collisions do not interact directly with the detector. Instead, they hadronize, forming a collimated groups of hadrons, often referred as "jets", which pass through the detector. The definition of jet is rather vague, as one can come up with many different ways of grouping particles.

Jet clustering algorithms are designed to cluster the complex structure of final state objects from each collision into jets. These jets reflect physical properties of the partons from hard scattering. Currently at CDF there are three jet clustering algorithms in use: JetClu [42], a cone algorithm combining objects based on relative separation in $\eta - \phi$ space; MidPoint, an algorithm similar to JetClu but having some modifications; and K_T [43], an algorithm combining objects based on their relative transverse momentum as well as their relative separation in $\eta - \phi$ space.

The JetClu algorithm was used in the measurements presented in this dissertation.

3.3.1 Jet Clustering

Jets are reconstructed based on the calorimeter information using a JetClu cone algorithm. The algorithm starts with the highest E_T tower and forms preclusters from an unbroken chain of continuous seed towers with transverse energy above 1 GeV within a window of 7×7 towers centered at the originating seed tower. If a seed tower is outside this window, it is used to form a new precluster. The coordinates of each precluster are the E_T-weighted sums of ϕ and η of the seed towers within this precluster:

$$E_T^{cluster} = \sum_{i=0}^{N_{towers}} E_{Ti},\qquad(3\text{--}8)$$

$$\phi^{cluster} = \sum_{i=0}^{N_{towers}} \frac{E_{Ti}\phi_i}{E_T{}^{cluster}}, \tag{3-9}$$

$$\eta^{cluster} = \sum_{i=0}^{N_{towers}} \frac{E_{Ti}\eta_i}{E_T{}^{cluster}}. \tag{3-10}$$

The tower centroid (η_i, ϕ_i) is obtained by:

$$\eta^i = \frac{E_{Ti}{}^{EM}\eta_i^{EM} + E_{Ti}{}^{HA}\eta_i{}^{HA}}{E_{Ti}}, \tag{3-11}$$

$$\phi^i = \frac{E_{Ti}{}^{EM}\phi_i^{EM} + E_{Ti}{}^{HA}\phi_i{}^{HA}}{E_{Ti}}, \tag{3-12}$$

where $E_{Ti}{}^{EM}$ and $E_{Ti}{}^{HA}$ are transverse energies deposited in the electromagnetic (EM) and hadronic (HA) parts of the i-th calorimeter tower, respectively.

In the next step, all towers with $E_T > 0.1$ GeV within $R = \sqrt{(\Delta\phi)^2 + (\Delta\eta)^2} = 1.0$ of the precluster are merged into a cluster, and its (η, ϕ)-coordinates are recalculated. This procedure of calculating cluster coordinates is iterated until a stable set of clusters is obtained. A cluster is stable when the tower list is unchanged from one iteration to the next. If the clusters have some finite overlap, then an overlap fraction is computed as the sum of the E_T of the common towers divided by the E_T of the smaller cluster. If the fraction is above a cutoff (0.75), then the two clusters are combined. If the fraction is less than the cutoff, the clusters are kept intact. The raw energy of a jet is the sum of the energies of the towers belonging to the corresponding cluster. The momentum of a jet is a scalar sum:

$$p_x = \sum_{i=0}^{N_{towers}} E_i \sin(\theta_i)\cos(\phi_i), \tag{3-13}$$

$$p_y = \sum_{i=0}^{N_{towers}} E_i \sin(\theta_i) \sin(\phi_i), \tag{3-14}$$

$$p_z = \sum_{i=0}^{N_{towers}} E_i \cos(\theta_i), \tag{3-15}$$

where (θ_i, ϕ_i) is the angular position of the i-th calorimeter tower.

3.3.2 Jet Corrections

Corrections are applied to the raw energy to compensate for the non-linearity and non-uniformity of the energy response of the calorimeter, the energy deposited inside the jet cone from sources other than the leading parton, and the leading parton energy deposited outside the jet cone. Here we give a brief review of the applied corrections. A detailed description of this procedure can be found in [44].

The first step is to correct for the η-dependence of the calorimeter response. This correction is especially important in the regions with significant non-uniformities and uninstrumented regions, such as between two halves of the central calorimeter, or between central, wall and plug calorimeters. The correction is based on a good understanding of the central region of the calorimeter. The ideas is that in an event with only two jets, their transverse energies should be balanced. The p_T of a "probe" jet, anywhere in the calorimeter is compared to the p_T of a "trigger" jet in the central region, away from uninstrumented regions, $0.2 < |\eta| < 0.6$. The results are shown in Fig. 3-12. The final corrections are derived as continuous functions of $'_T$ and binned functions of η.

The next step is designed to correct for multiple $p\bar{p}$ interactions in the same bunch crossing. This is done by measuring the amount of energy deposited in a randomly chosen cone of radius $R = 1.0$ in minimum bias events, triggered by requiring hits in the CLC

counters on either side of the detector. The correction is parametrized as a function of the number of primary vertexes in an event.

The so called "absolute" correction accounts for the non-linear response of the calorimeter. The CDF calorimeters respond differently to particles of various energies. An average correction is determined from dijet Monte Carlo. This correction relies on the careful tuning of the detector simulation, based on "in situ" calibrations using data tracks at low energies and test beam data at high energies. The correction is a function of p_T.

Finally, the so called "out-of-cone" correction account for the particle-level energy leakage of radiation outside the clustering cone. It corrects the jet energy back to the parent parton energy. The correction is based on the ratios of jet and parent parton energies obtained from the Monte Carlo.

3.4 Monte Carlo Generators and Detector Simulation

The ability to accurately simulate the production of physics events and their propagation through the detector is extremely important in High energy Physics analysis. In this section we provide a brief review of the Monte Carlo (MC) generators used in the analysis, as well as the software used to simulate CDF detector response. In the measurements described in this dissertation MC generators were used mainly to evaluate systematic uncertainties. We also compare MC predictions to data to verify if MC is able to predict some of the features of CDF jet fragmentation data.

3.4.1 Event Generators

The usual sequence in preparing a MC sample starts with generating physics process of interest. In our case it is hard QCD $2 \rightarrow 2$ scattering of partons from protons and antiprotons. This is done by such well-known programs (also called generators) Pythia

and Herwig. Pythia Tune A [45, 46] and Herwig 6.5 [47] are used for studies discussed in this dissertation.

Jet fragmentation in both generators two steps: the perturbative initial- and final-state parton showering and hadronization using phenomenological models. The parton shower models of Pythia and Herwig are very similar. The cascade evolution is treated as a branching process based on the Leading Log Approximation (LLA). The probability for the decay of a parton into two partons is evaluated using "DGLAP" evolution equation [48]. The QCD coherence effects are included in both generators, however, with some differences. The treatment of hard gluon emission in Herwig is improved by matching of the first gluon branching to the three-jet matrix element. In both generators the parton shower is terminated when the parton virtualities drop below Q_{eff}.

The implementation of hadronization is different in Pythia and Herwig. The conversion of partons to hadtons in Pythia is accomplished by the Lund String Model [49]. The concept of this model can be easily understood using an example of the $q\bar{q}$ production in e^+e^- annihilation. The produced quark and antiquark move out in opposite directions, losing energy to the color field, which collapses into a string-like configuration between them. The string then breaks up into hadrons through spontaneous $q\bar{q}$ pair production in its intense color field. The addition of gluon radiation results in kinks on the string, each carrying localized energy and momentum equal to that of its parent gluon. During a string breakup, the equal and opposite transverse momenta of quarks from a $q\bar{q}$ pair are generated according to a Gaussian distribution. Longitudinal hadron momenta are determined by means of phenomenological fragmentation functions. Baryon production is included by allowing diquark-antiquark pairs to be created. Meson production in the string between baryon and antibaryon is also allowed.

74

Herwig utilizes the so-called cluster hadronization model [50], the implementation of which is following. At the end of parton shower, all gluons are forced to split into $q\bar{q}$ pairs. Neighboring $q\bar{q}$ pairs form color-neutral clusters which decay in their rest frame into two hadrons. Special treatment is given to very light clusters, which are allowed to decay into a single hadron, and to very heavy clusters which can decay into smaller clusters. Baryons are produced from cluster decays into baryon-antibaryon pairs, *i.e.* clusters themselves always have zero baryon number.

Both MC generators have their advantages and disadvantages. The string hadronization model used in Pythia was tested extensively in e^+e^- collisions ans showed and excellent agreement with data. However, a large number of phenomenological parameters somewhat shadows the perturbative information. The advantage of the cluster model used in Pythia is its simplicity and that the global event shape is determined by the parameters describing the parton shower (Λ_{QCD} and Q_{cutoff}), and to a lesser extent by the thresholds of cluster mass.

3.4.2   CDF Simulation

After hadronization, hundreds of final state particles are passed to the CDF simulation (CDFSim) package. It contains a detailed description of the CDF detector geometry including the active detector elements as well as passive material, such as read-out electronics, cables, support structures, *etc.* The overall framework for the simulation is done using the GEANT package [51], with some modifications directed at making the simulation work faster. Once the detector is built in the language of GEANT, almost any kind of particle can be tracked through it with all appropriate physics processes taking place to mimic the physical detector response. Some interaction are handled with specific parametrized models, such as GFLASH shower simulation

package [52], tuned to single particle response and shower shape based on the test beam and collision data. The "raw" data (digitized physical detector response) after detector simulation is fed to the algorithm that implements the actual trigger logic to decide if the event should be accepted. The events passing the trigger simulation go through production stage, in which the collection of physics objects (tracks, jets, muons, *etc.*) are created from the raw data.
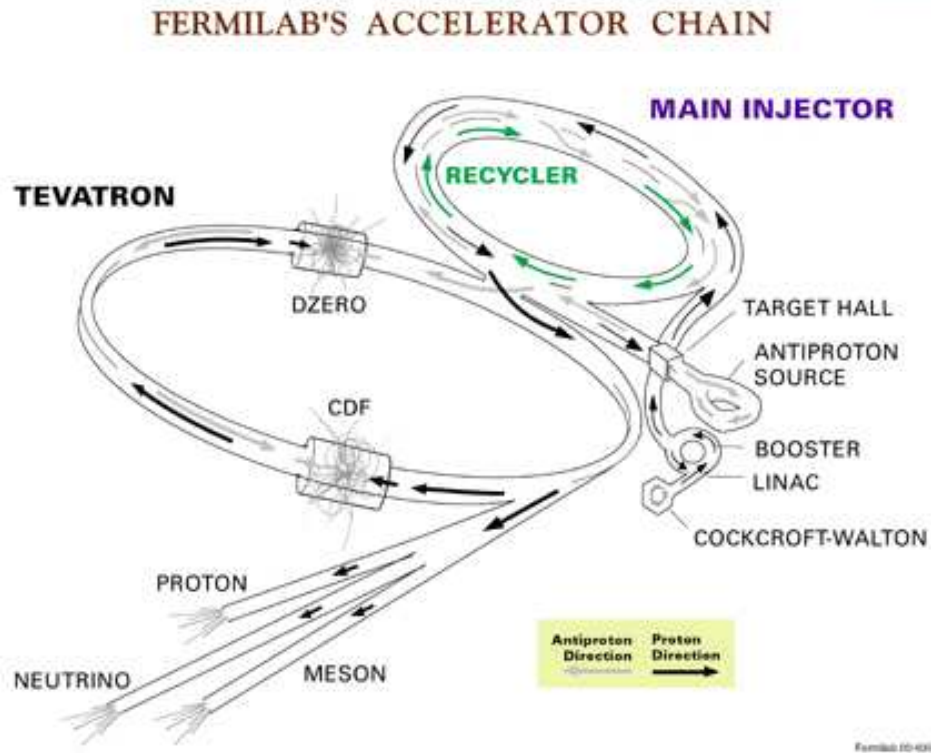
Figure 3-1. The schematic picture of the accelerator chain at Fermilab. The chain consists of several individual components: Proton Source (Cockcroft-Walton, Linac and Booster), Main Injector, Antiproton Source (Debuncher, Accumulator and Recycler) and the Tevatron. The detectors, CDF and D0, are also shown.

Table 3-1. Summary of the current Tevatron performance characteristics.

center-of-mass energy	1.96 TeV
bunch crossing separation	396 ns
number of protons per bunch	240×10^9
number of antiprotons per bunch	25×10^9
peak luminosity	290×10^{30} cm^{-2}s^{-1}

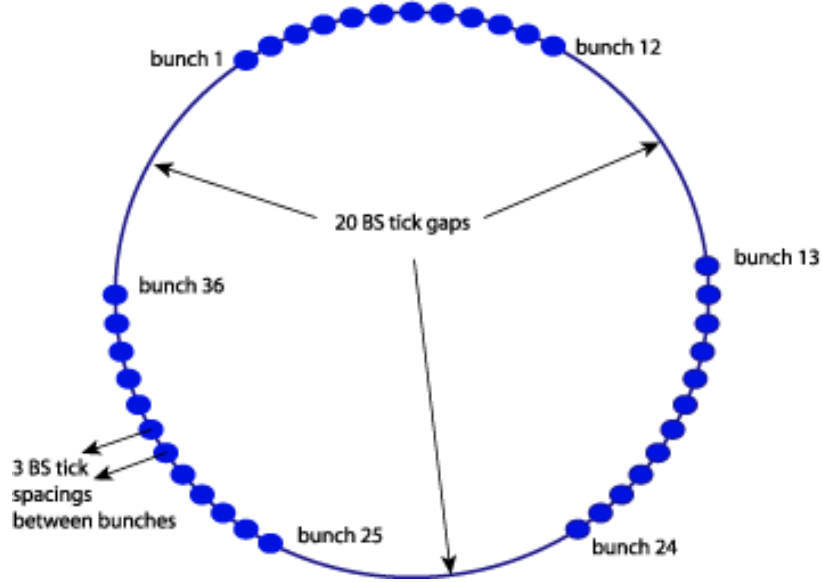Figure 3-2. The proton and antiproton beam structure at the Tevatron. Each beam is divided into three "trains" separated by the abort gap. Each train contains 12 bunches of protons or antiprotons. The time separation between consequent bunches is 396 ns.

Table 3-2. Summary of quantities characterizing CDF calorimetry.

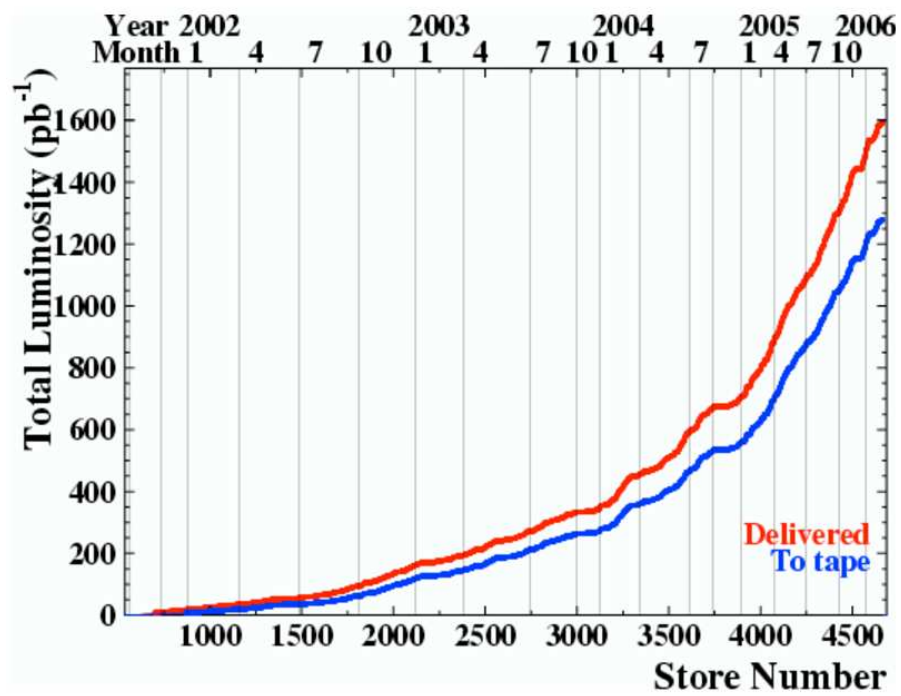| Name	Thickness	Material	Resolution (E in GeV)
CEM	$19X_0$	3 mm Pb, 5 mm Scint.	$13.5\%/\sqrt{E} + 2\%$
PEM	$21X_0$	4.5 mm Pb, 4 mm Scint.	$16\%/\sqrt{E} + 1\%$
CHA	$4.7\lambda_0$	25 mm Fe, 10 mm Scint.	$75\%/\sqrt{E} + 3\%$
WHA	$4.5\lambda_0$	50 mm Fe, 10 mm Scint.	$75\%/\sqrt{E} + 3\%$
PHA	$7\lambda_0$	51 mm Fe, 6 mm Scint.	$80\%/\sqrt{E} + 5\%$

Figure 3-3. The total integrated luminosity delivered by the Tevatron from the beginning of Run II which started in April 2001. The live luminosity, which excludes integrated luminosity during all the detector dead-times is also shown.
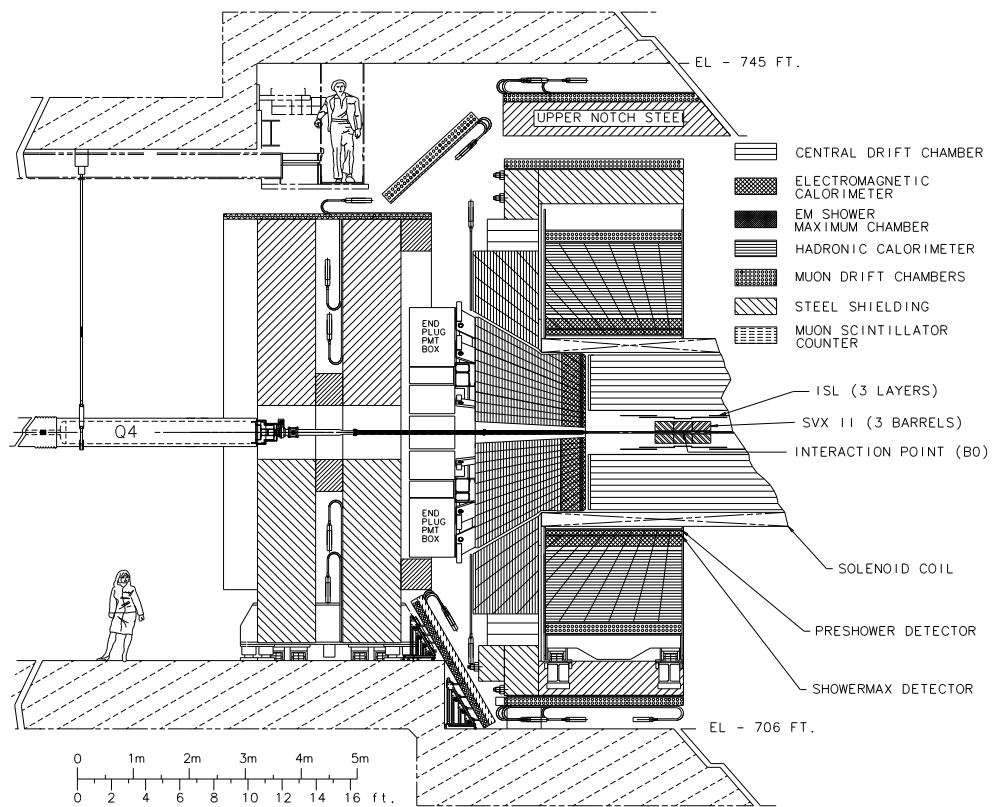
Figure 3-4. The schematic cross-section view of the CDF detector.

CENTRAL DRIFT CHAMBER

ELECTROMAGNETIC
CALORIMETER

EM SHOWER
MAXIMUM CHAMBER

HADRONIC CALORIMETER

MUON DRIFT CHAMBERS

STEEL SHIELDING

MUON SCINTILLATOR
COUNTER

EL – 745 FT.

UPPER NOTCH STEEL

END
PLUG
PMT
BOX

END
PLUG
PMT
BOX

Q4

ISL (3 LAYERS)

SVX II (3 BARRELS)

INTERACTION POINT (B0)

SOLENOID COIL

PRESHOWER DETECTOR

SHOWERMAX DETECTOR

EL – 706 FT.

0   1m   2m   3m   4m   5m

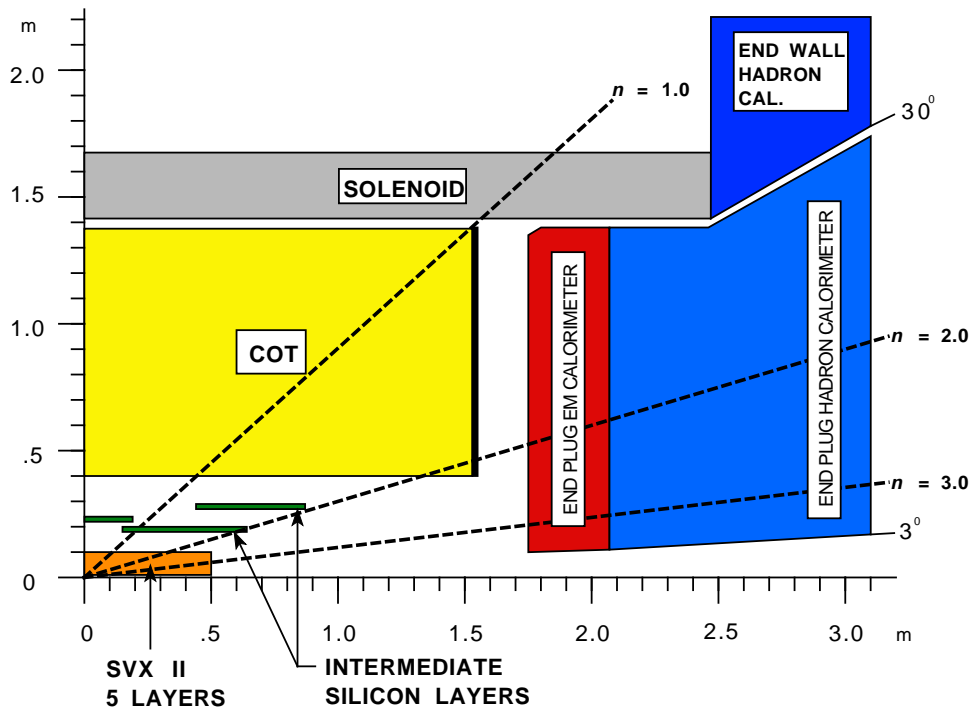0   2   4   6   8   10   12   14   16 ft.

CDF Tracking Volume

Figure 3-5. The schematic r–z view of one quadrant of the CDF tracking system. Its components: Central Outer Tracker (COT) and the silicon detectors: Layer00 (L00), Silicon Vertex Detector (SVX), and Intermediate Silicon Layers (ISL) are shown.
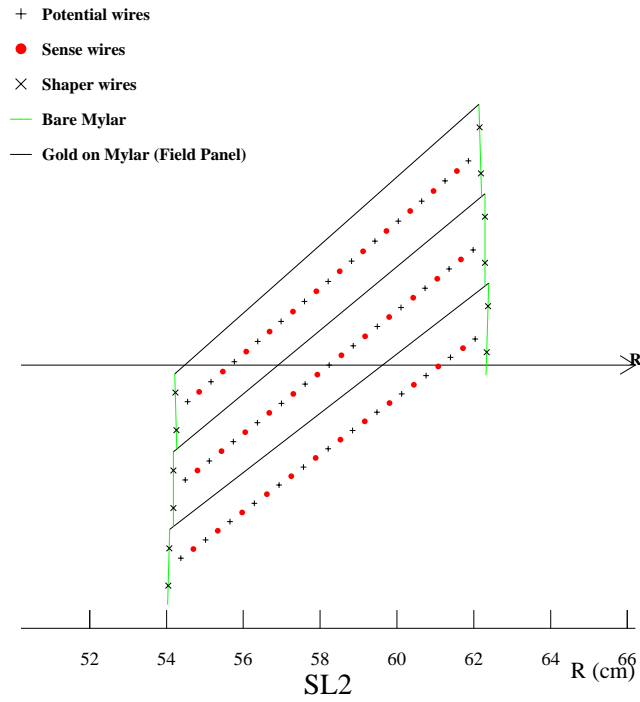
Figure 3-6. Transverse view of the nominal cell layout for COT superlayer 2. The arrow shows the radial direction. The electric field is roughly perpendicular to the field panels. The magnetic field is perpendicular to the plane. The angle between wire-plane of the central cell and the radial direction is 35°
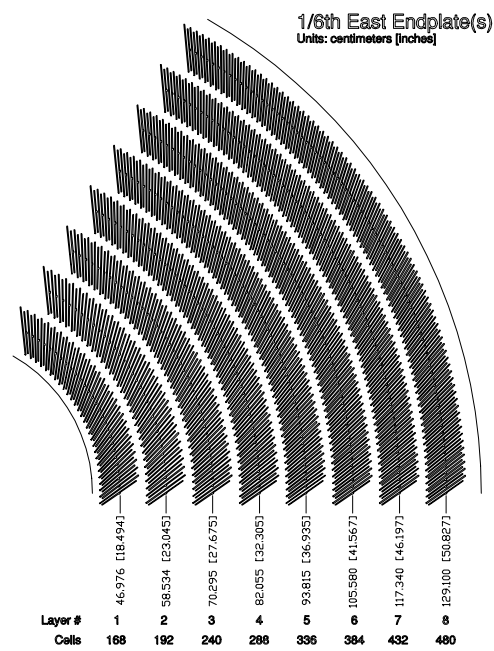
Figure 3-7. 1/6th of the COT east end plate. Shown are the wire-plane slots grouped into eight superlayers.
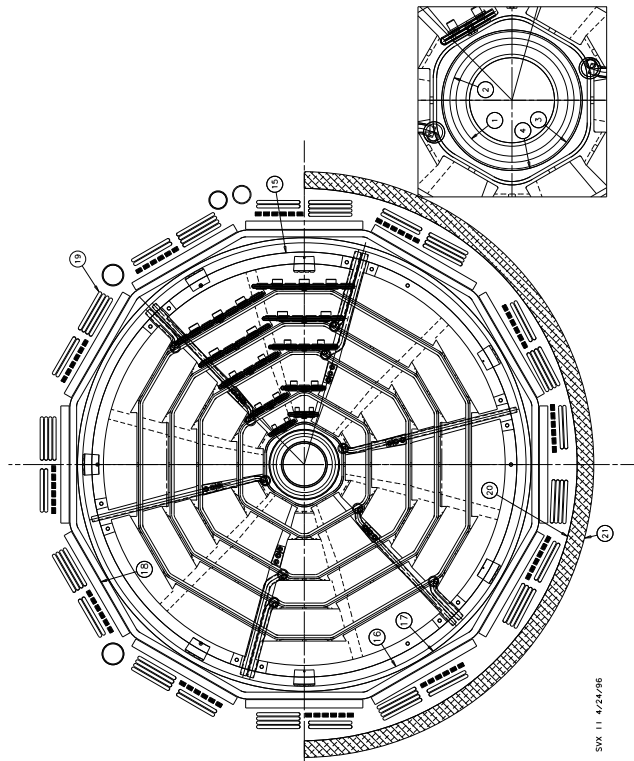
Figure 3-8. SVX bulkhead design. Placement of ladders is shown in two adjacent wedges.
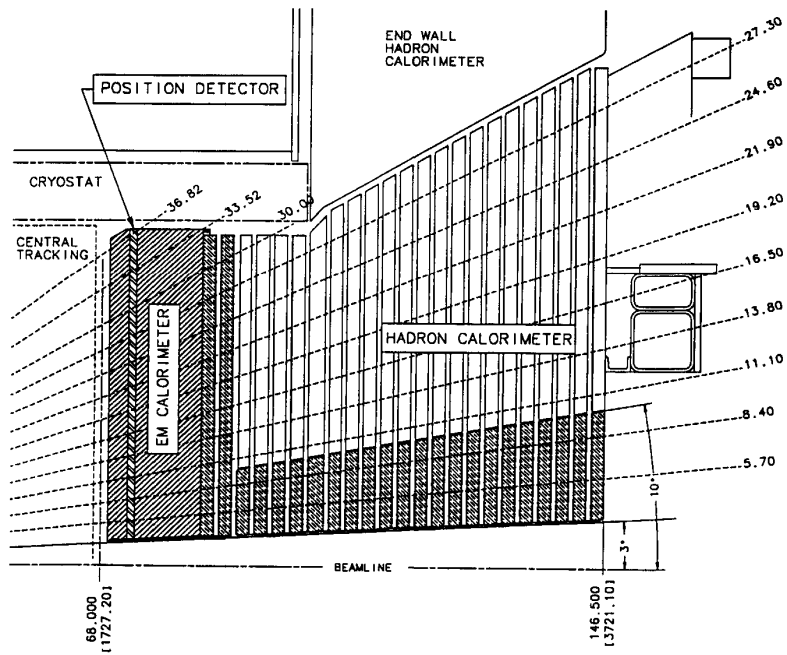
Figure 3-9. Schematic picture of one quadrant of the plug calorimeter including the electromagnetic and hadronic parts. The plug calorimeter has full 2π coverage and extends to $1.1 < |\eta| < 3.6$
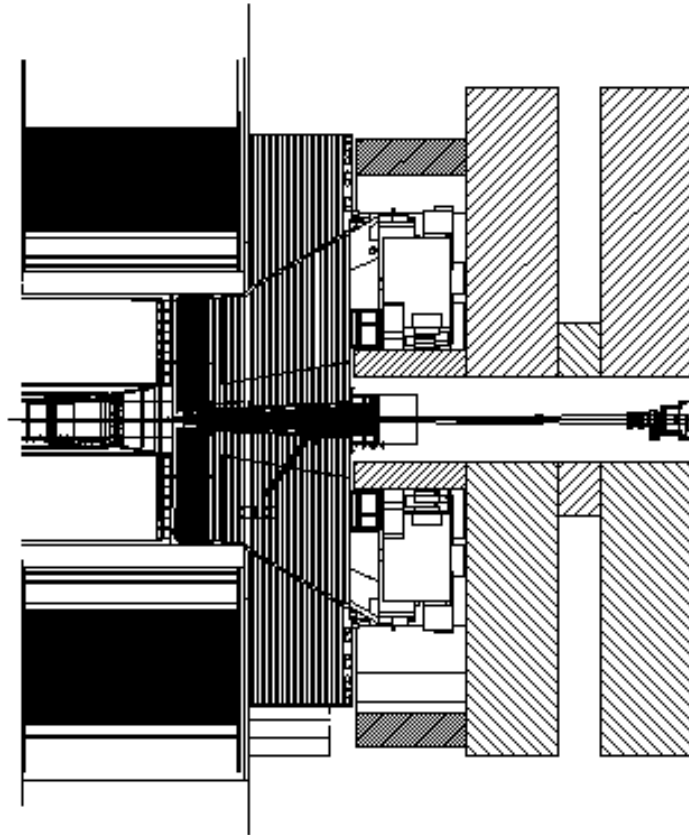
Figure 3-10. The Cherenkov Luminosity Counter at CDF. The detector modules are
located within the "3-degree holes" inside the forward and backward
calorimeters.

Dataflow of CDF "Deadtimeless"
Trigger and DAQ

Detector

7.6 MHz Crossing rate
132 ns clock cycle

L1 Storage
Pipeline:
42 Clock
Cycles Deep

L1 trigger

Level1:
7.6 MHz Synchronous pipeline
5544ns latency
<50 kHz Accept rate

L1 Accept

L2 Buffers:
4 Events

L2 trigger

Level 2:
Asynchronous 2 stage pipeline
~20μs latency
300 Hz Accept Rate

L2 Accept

L1+L2 rejection: 20,000:1

DAQ Buffers

L3 Farm

Mass
Storage

PJW 10/28/96
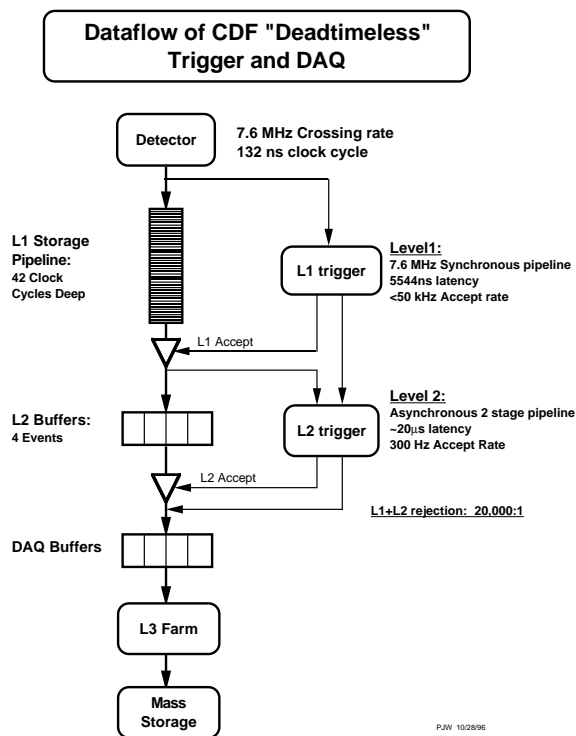
Figure 3-11. Functional block diagram of the CDF data flow. The crossing rate at the Tevatron is actually only 2.5 MHz, but the trigger system was designed for the originally envisioned 7.5 MHz crossing.

Figure 3-12. The ratio $\beta = p_T^{probe}/p_T^{trigger}$ of transverse momenta of the "probe" and the "trigger" jets using the 70 GeV jet trigger, obtained using two different methods (missing E_T projection fraction and dijet balancing. The "probe" trigger jet has to be in a central region $0.2 < |\eta| < 0.6$, while the probe jet may be anywhere in the calorimeter.

88

CHAPTER 4
ANALYSIS OF THE DATA

In order to conduct the desired studies of jet fragmentation we need to isolate
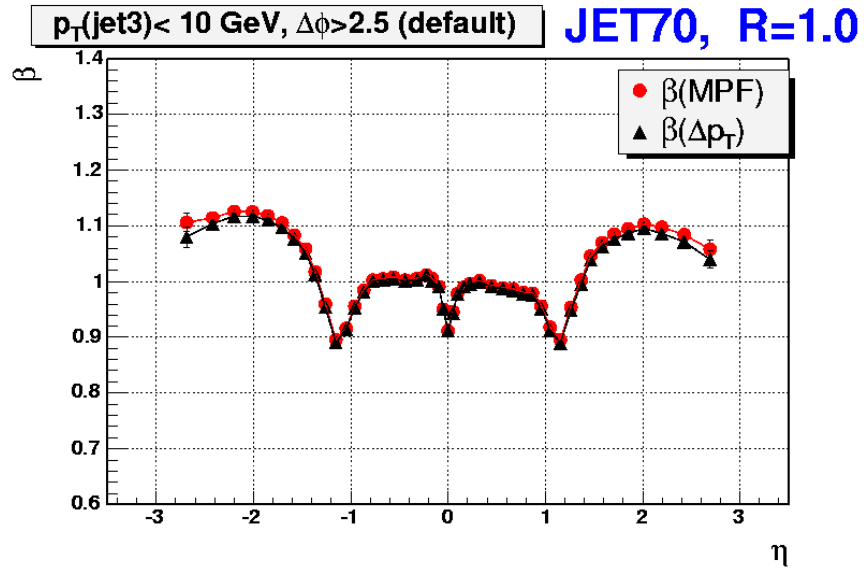events of interest by applying certain event selection criteria, the measurements are then
done using tracks in selected events. The next step is to evaluate contributions from
various sources of background, and to correct for these contributions. Unfortunately,
the separation of signal tracks from background tracks can not be perfect, and a certain
amount of background makes its way into the sample, which needs to be taken into
account in the evaluation of systematic uncertainties.

This chapter presents a detailed discussion of the measurements, including explanations
of the event selection, the correction for various backgrounds and the evaluation of
systematic uncertainties. This is done first in detail for the two-particle momentum
correlations, and then, succinctly, for the k_T distributions.

4.1   Two-particle Momentum Correlations

4.1.1   Data Samples

We report a measurement of the two-particle momentum correlations for charged
particles in events with dijet invariant masses in the range 66–563 GeV/c^2. Events were
produced at the Tevatron collider in $p\bar{p}$ collisions at a center of mass energy of 1.96 TeV
and were recorded by the CDF Run II detector. The results are based on data collected
during the running period from February 2002 to August 2004. The total integrated
luminosity was 385 pb^{-1}. The data are fit to NLLA analytical functions and the value of
the parton shower cutoff Q_{eff} is extracted. The correlations observed in data are compared
to Monte Carlo predictions by the Pythia Tune A and Herwig 6.5 event generators.

Events were collected using a single calorimeter tower trigger with a transverse energy (E_T) threshold of 5 GeV and with single jet triggers with E_T thresholds of 20, 50, 70, and 100 GeV. Each of the jet triggers had a different sampling rate so as to not saturate the available trigger bandwidth.

4.1.2 Event Selection

Cosmic ray events are rejected by applying a cutoff on the missing transverse energy $\not{E}_T$ significance [53], defined as $\not{E}_T / \sqrt{\Sigma E_T}$, where $\Sigma E_T = \Sigma_i E_T^i$ is the total transverse energy of the event, as measured using calorimeter towers with E_T^i above 100 MeV. The cut values are 3.0 GeV$^{1/2}$ for data collected using a single tower trigger with E_T threshold of 5 GeV, and 3.5, 5.0, 6.0, and 7.0 GeV$^{1/2}$ for data collected using jet triggers with thresholds of 20, 50, 70 and 100 GeV, respectively.

We require only one vertex in the event with $|z| < 60$ cm along the z axis. The cut value 60 cm is selected to ensure fully efficient vertex and track reconstruction.

To ensure robust and high efficiency track reconstruction and applicability of the background removal technique (see Sec. V(B)), only events with both leading jets in the central region ($|\eta| < 0.9$) are selected. To reject events with poorly measured jets, we require two leading jets to be well balanced in E_T: $|k_\perp| / (E_T^1 + E_T^2) < 2\sigma_{k_\perp}$, where E_T^1 and E_T^2 are the transverse energies of the first and the second leading jets, respectively, and $k_\perp$ and $k_\parallel$ are defined as:

$$k_\perp = \sqrt{k^2 - k_\parallel^2}, \tag{4--1}$$

$$k_\parallel = (E_T^1 + E_T^2) \cdot cos(\phi/2), \tag{4--2}$$

90

where $\vec{k}$ is a vector sum of momenta of the two leading jets, ϕ is the angle between two leading jets, and $\sigma_{k_\perp}$ is the resolution of $k_\perp$. The definitions of $\vec{k}$, $\vec{k_\perp}$, and $\vec{k_\parallel}$ are illustrated in Fig. 4-1. The component $k_\perp$ is known to be sensitive to the energy mismeasurement of jets, while $k_\parallel$ is more sensitive to the hard gluon radiation.

In events with high energy jets, a single particle emerging from a jet at a sufficiently large angle with respect to the jet axis can be identified as a separate jet. A jet can also be produced from the underlying event. Therefore, rejection of all events with more than two jets can introduce possible biases. We allow up to two extra jets, but their energy is required to be small: $E_T^{extra} < 5.5 + 0.065(E_T^1 + E_T^2)$, where E_T^{extra} is the transverse energy of an extra jet.

After application of the event selection cuts, the final sample consists of approximately 250,000 events and is further divided into seven bins according to the dijet mass as measured by the calorimeters and defined as:

$$M_{jj} = \sqrt{(E_1 + E_2)^2/c^4 - (\vec{P}_1 + \vec{P}_2)^2/c^2},$$ (4–3)

where E and $\vec{P}$ are the energies and momenta of the jets, respectively.

The mass bin boundaries, average invariant mass $\langle M_{jj} \rangle$ and number of events in each bin are given in Table 4-1. The bin width is selected to be $3 \cdot \delta M_{jj}$, where δM_{jj} is the calorimeter resolution for the dijet mass determination, $\frac{\delta M_{jj}}{M_{jj}} \sim 7$–10%.

4.1.3 Track Quality Requirements

Measurements to be described below are performed in the dijet center of mass frame. For Lorentz boosts all particles are treated as pions. Experimentally we define the variable ξ as $\xi = 1/x = \ln \frac{E_{jet}}{p_{track}}$, where E_{jet} is the jet energy as measured by the calorimeters and p_{track} is the track momentum as measured by the tracking system. The correlation

distributions are measured for all tracks pairs that pass track quality requirements and lie within a restricted cone of opening angle $\theta_c = 0.5$ radians relative to the jet axis. The peak position of the inclusive momentum distribution ξ_0 is constant for given jet hardness Q and is obtained from the data. The measurements are corrected for various backgrounds both correlated and uncorrelated with jet direction.

Several selection requirements are applied to ensure that the tracks in the measurement originate at the primary vertex and are not produced by cosmic rays, multiple $p\bar{p}$ interactions within the same bunch crossing, γ-conversions, K^0 and Λ-decays or other types of backgrounds.

In our analysis, we require full three-dimensional track reconstruction. The description of CDF track reconstruction can be found in [37, 54]. Poorly reconstructed and spurious tracks are removed by requiring good track fitting parameters, $\chi^2_{COT} < 6.0$. Tracks are required to have $p_T > 0.3$ GeV/c.

The parameter Δz is defined as the difference between the z position of the track at the point of its closest approach to the beam-line and the z position of the primary vertex. This parameter is used to remove tracks not originating at the primary interaction by requiring $|\Delta z| < 5 \cdot \sigma_{\Delta z}$, where $\sigma_{\Delta z}$ is determined for different categories of tracks based on the number of SVX and COT hits. The Δz distribtuions for tracks reconstructed with different track reconstruction algorithms are shown in Fig. 4-2. The measured values of $\sigma_{\Delta z}$ are summarized in Table 4-2.

Tracks produced from γ-conversions are removed using a combination of cuts on impact parameter d_0 and the distance R_{conv} (Fig. 4-4). The impact parameter d_0 is defined as the shortest distance in the $r - \phi$ plane between the interaction point and the trajectory of the particle obtained by the tracking algorithm fit. It can be shown that for

92

electrons and positrons originating from γ-conversion:

$$R_{conv} = \sqrt{\frac{d_0 p_T}{0.15B}}, \tag{4–4}$$

where p_T is the transverse momentum of the charged particle in GeV/c, B is the magnetic field in Tesla and R_{conv} is measured in meters. Monte Carlo studies indicate that the d_0 cut alone is less efficient at removing γ-conversion tracks than it is to require tracks to have $|d_0| < 5 \cdot \sigma_{d_0}$ or $R_{conv} < 13$ cm. The value $R_{conv} = 13$ cm is motivated by the location of SVX port cards. Indeed, conversions occurring at this radius are clearly seen in the data. The resolution of the impact parameter, σ_{d_0}, is evaluated for different categories of tracks based on the number of SVX and COT hits. The impact parameter distribtuions for tracks reconstructed with different track reconstruction algorithms are shown in Fig. 4-3. The measured values of σ_{d_0} are summarized in Table 4-3.

To verify the effectiveness of the track quality cuts, we compare distributions of the inclusive particle multiplicity and momentum in the Pythia Tune A at the generator level and at the full detector simulation (CDFSim) level. The comparison is shown in Fig. 4-5 and Fig. 4-6. CDFSim propagates particles through the detector including both conversions and in-flight decays to simulate the CDF detector response. The agreement, after selection cuts are applied, confirms that the cuts do remove most of the background tracks.

4.1.4 Underlying Event Background Subtraction

Generally, tracks from the underlying event tend to dissolve the two-particle momentum correlation. It is not possible to correct for this effect on an event-by-event basis, but the average correction factor can be reconstructed statistically. In order to correct for the underlying event contribution, we use the complementary cones technique.

On an event-by-event basis, two complementary cones are positioned at the same polar angle with respect to the beam-line as the original dijet axis but rotated in ϕ so that they are at $90°$ (*i.e.* as far as possible) from the dijet axis, as shown in Fig. 4-7. This can be done when the dijet axis is within $45° < \theta < 135°$, and this condition is automatically satisfied by our event selection. We assume that cones formed in such a fashion collect statistically the same amount of background (which is uncorrelated with jets) as the cones around the jet axis [23].

In order to obtain the corrected expression for $C(\Delta\xi_1, \Delta\xi_2)$, one needs to subtract the background from the one- and two-particle momentum distributions. This can be achieved by considering particles in jet cones together with particles in complementary cones. It can be shown that the momentum distributions after background subtraction $\tilde{D}$ are:

$$\tilde{D}(\xi) = D_{jet}(\xi) - D_{compl}(\xi), \tag{4–5}$$

$$\tilde{D}(\xi_1, \xi_2) \approx 2D_{jet}(\xi_1, \xi_2) - D_{jet+compl}(\xi_1, \xi_2) + 2D_{compl}(\xi_1, \xi_2), \tag{4–6}$$

where *jet* subscript denotes the distribution for particles in jet cones, *compl* denotes the distribution for particles in complementary cones, and *jet + compl* denotes the distribution for the combined set of particles in either jet cones or complementary cones.

4.1.5   Systematic Uncertainties

The sensitivity of the two-particle momentum correlation parameters c_0, c_1, and c_2 to various uncertainties in the event selection procedure is evaluated as follows. For each source of the systematic uncertainty, the so-called "default" and "deviated" two-particle momentum correlation distributions are obtained. A "default" distribution is produced using a default set of cuts described in the paper. Then, a "deviated" distribution

is obtained by varying all relevant parameters according to the estimated systematic uncertainty (one source of uncertainty at a time). For each bin in correlation $C(\Delta\xi_1, \Delta\xi_2)$, the scale factor is produced by taking the bin-by-bin ratio of the "deviated" and the "default" distributions:

$$\epsilon = \frac{C(\Delta\xi_1, \Delta\xi_2)_{deviated}}{C(\Delta\xi_1, \Delta\xi_2)_{default}}. \qquad (4\text{--}7)$$

The difference between correlation distributions in data, with and without this bin-by-bin scale factor applied, is taken as a measure of the systematic uncertainty:

$$\Delta C(\Delta\xi_1, \Delta\xi_2)_{Data} = \left|(1 - \epsilon) \cdot C(\Delta\xi_1, \Delta\xi_2)_{Data}\right|. \qquad (4\text{--}8)$$

Further in this section we discuss different sources of systematic uncertainties at the level of the event selection. Their contributions to the values of c_0, c_1, and c_2 are given in Table 4-4.

In each trigger sample only events with trigger efficiency higher than 99% were used. To check that trigger effects do not bias the measurement, we verify the continuity of the distributions of particle multiplicity in a jet in the transition between adjacent dijet trigger samples. No detectable offsets are observed.

To evaluate the uncertainty due to the selection of the jet reconstruction algorithm, we compare results of the measurement using three different values of the parameter R used in the jet reconstruction algorithm (0.4, 0.7, 1.0). This effect proved to be small compared to the other sources of systematic uncertainties.

We require only one vertex in the event. However, in some cases two vertexes can be very close to each other and get reconstructed as a single vertex. This can become significant at high values of instantaneous luminosity. To evaluate the uncertainty due to

this effect, we subdivide each dijet mass bin into sub-bins by the value of instantaneous luminosity. Momentum correlation distributions are compared in these sub-samples and the difference is taken as a measure of the systematic uncertainty.

To evaluate the uncertainty due to the jet energy corrections, we use parameterizations that under- and overestimate the jet energy by one standard deviation of the jet energy correction and then we reclassify events according to dijet mass. The difference between the default and deviated distributions is assigned to be the systematic uncertainty.

We use Monte Carlo dijet samples produced by Pythia Tune A to study systematic uncertainties associated with the jet balance requirement, the number of allowed extra jets and their energy. The "default" two-particle momentum correlation distribution is compared to the "deviated" one. The latter distributions has no requirements imposed on the jet balance or on the extra jet number and extra jet energy.

Monte Carlo simulations are utilized to evaluate the systematic uncertainty due to the mismeasurement of jet direction. Two-particle momentum correlations are compared for two cases. In one case, particles are counted in a restricted cone around the jet direction as determined by the detector response in the simulation. In the second case, the direction of primary partons from hard scattering, as given by Pythia Tune A, is used for the cone axis.

The effect of the remaining (after track selection requirements) fraction of secondary tracks is estimated by comparing the correlation distributions $C(\Delta\xi_1, \Delta\xi_2)$ at the charged hadron level and the CDFSim level and producing a corresponding bin-by-bin scale factor. The difference between distributions in data, with and without this scale factor applied, is assigned as the systematic uncertainty associated with the track quality cuts.

To evaluate systematic uncertainties associated with the background subtraction using the complementary cone technique, we use the following procedure. The amount of background in a jet cone is increased by a factor of two by adding tracks from a complementary cone of another event. Then, the background subtraction procedure, described above, is applied, taking into account the artificially doubled background. After the subtraction, the correlation distribution is expected to be the same as the distribution using the original background. The difference between the two-particle momentum correlation distributions, obtained after the subtraction of either the original or the doubled background, is assigned as a measure of the systematic uncertainty.

4.1.6 Effect of Tracking Inefficiency

A high efficiency of track reconstruction is ensured by selecting events with central jets. However, there still may be non-reconstructed tracks inside the jet. To evaluate the corresponding systematic uncertainty, we have modeled the track reconstruction inefficiency using the function $P(\xi) = p_1 + p_2\xi$, which denotes the probability of losing a track with given ξ. Values of the parameters p_1 and p_2 were varied over a range far exceeding the estimated COT inefficiency. The correlation distributions show a very weak dependence on tracking inefficiency. The range of momentum correlation variation in this tracking inefficiency model is taken as a measure of the systematic uncertainty.

4.1.7 Neutral Particles

Theoretical predictions of correlation distributions are done at the parton level, while LPHD relates final partons to hadrons, assuming that all hadrons are counted. The analysis, however, is done for charged particles only. To estimate this effect, the momentum correlation in a Pythia Tune A sample is compared for charged particles and all particles. The difference is assigned as the corresponding systematic uncertainty.

4.1.8 Heavy flavor jets

Theoretical predictions of correlation distributions are obtained for jets originated from gluons or light quarks only. In the data sample we expect a small fraction ($\sim$ 5 %) of heavy flavor jets. To estimate the size of this effect we repeat the analysis with the assumption that the correlations in heavy flavor jets are same as in gluon jets. This translates into the 3 MeV change in the value of Q_{eff} and is negligibly small compared to the size of the systematic uncertainty.

4.1.9 Resonance Decays

The presence of resonance decays may be expected to cause data-theory offsets. We examine this effect by comparing the correlation in Monte Carlo events at the level of final hadrons with the correlation at the stage before resonance decays. We find that this results in insignificant changes in $C(\Delta\xi_1, \Delta\xi_2)$ and does not change the overall level of the correlation.

4.2   The k_T Distributions

The event and track selection, the corrections and the evaluation of systematic uncertainties for the k_T distributions analysis are very similar to those of the two-particle momentum correlations analysis, and are described in detail in previous section. Here we give explanations to things done differently than in the two-particle momentum correlations measurement.

4.2.1 Data Samples

The measurement of the k_T distributions is done for charged particles in events with dijet invariant masses in the range 66–737 GeV/c^2. The results are based on data collected during the running period from February 2002 to September 2005. The total integrated luminosity was 774 pb^{-1}. The data are compared to the MLLA and the

NMLLA analytical functions as well as the predictions by the Pythia Tune A and Herwig 6.5 event generators.

Measurement of the k_T distributions requires less statistics than measurement of the two-particle momentum correlations. This, together with the increased integrated luminosity, allowed to extend the measurement to higher values of jet energies. The mass bin boundaries for this measurement , average invariant mass $\langle M_{jj} \rangle$ and number of events in each bin are given in Table 4-5.

4.2.2 Underlying Event Background Subtraction

To correct for the contribution from the underlying event we use the complementary cone technique, described earlier in this dissertation in the context of two-particle momentum correlations. For the k_T distributions, however, the corrected expression is more straightforward:

$$\frac{dN_{hadrons}}{dln(k_T)} = (\frac{dN_{hadrons}}{dln(k_T)})_{jet} - (\frac{dN_{hadrons}}{dln(k_T)})_{compl}, \qquad (4\text{--}9)$$

where the subtraction is done bin-by-bin.

4.2.3 Effect of Tracking Inefficiency

This effect was accounted for slightly differently than in the two-particle momentum correlations analysis. The tracking inefficiency was varied as a function of r (distance between track and jet axis in the $\eta - \phi$ space) and transverse momenta of both jet and track. The detailed studies have been performed [55] to measure the track reconstruction inefficiency inside jets as a function of r and the jet and track transverse momenta, using track embedding techniques. The effect of on the k_T distributions is found to be small and is absorbed into the systematic uncertainty.

Table 4-1. Measurement of momentum correlations: dijet mass bins boundaries, average invariant dijet mass $\langle M_{jj} \rangle$ and number of events in each bin after the event selection cuts.

Bin	Low edge (GeV/c^2)	High edge (GeV/c^2)	$\langle M_{jj} \rangle$ (GeV/c^2)	Number of events
1	66	95	76	15229
2	95	132	108	77246
3	132	180	149	17682
4	180	243	202	80608
5	243	323	272	18528
6	323	428	361	12000
7	428	563	475	19150

Table 4-2. The $\sigma_{\Delta z}$, evaluated for different categories of tracks based on the number of SVX and COT hits.

Algorithm	$\sigma_{\Delta z}$, cm
COT-only	1.20
Inside-Out (IO)	0.60
Outside-In $r\phi$	1.80
Kalman Outside-In $r\phi$	1.80
Outside-In stereo	0.40
Kalman Outside-In stereo	0.40
Outside-In 3D	0.21
Kalman Outside-In 3D	0.21
SVX Only	0.78

Table 4-3. The resolution of the impact parameter, σ_{d_0}, evaluated for different categories of tracks based on the number of SVX and COT hits.

Algorithm	σ_{d_0}, mm
COT-only	0.110
Inside-Out (IO)	0.013
Outside-In $r\phi$	0.020
Kalman Outside-In $r\phi$	0.020
Outside-In stereo	0.014
Kalman Outside-In stereo	0.014
Outside-In 3D	0.0095
Kalman Outside-In 3D	0.0095
SVX Only	0.020
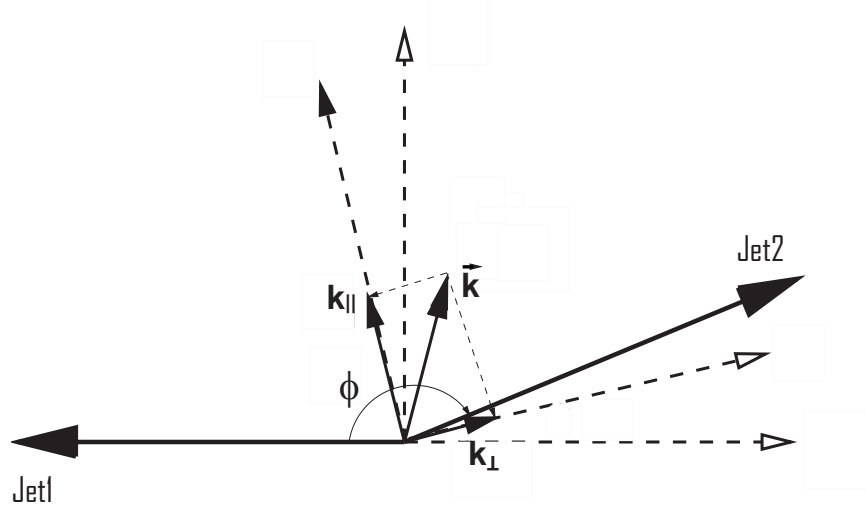
Figure 4-1. Definition of variables in the jet balance cut. Vector $\vec{k}$ represents a vector sum of the two leading jets' momenta. The $\vec{k}_{\parallel}$ and $\vec{k}_{\perp}$ components of $\vec{k}$ are parallel and perpendicular to the bisector of two jets.

Table 4-4. Summary of the systematic uncertainties of the correlation parameters c_0, c_1 and c_2 for the dijet mass bin with $Q = 50$ GeV.

Origin of systematic uncertainty	Δc_0	Δc_1	Δc_2
Luminosity dependence	0.001	0.004	0.002
Jet energy scale	0.001	0.001	0.001
Balance and extra jet cuts	0.006	0.001	0.003
Mismeas. of jet direction	0.006	0.008	0.007
Track quality cuts	0.014	0.008	0.006
Underlying event background	0.001	0.004	0.001
Tracking inefficiency	0.011	0.001	0.002
Neutral particles	0.002	0.002	0.001
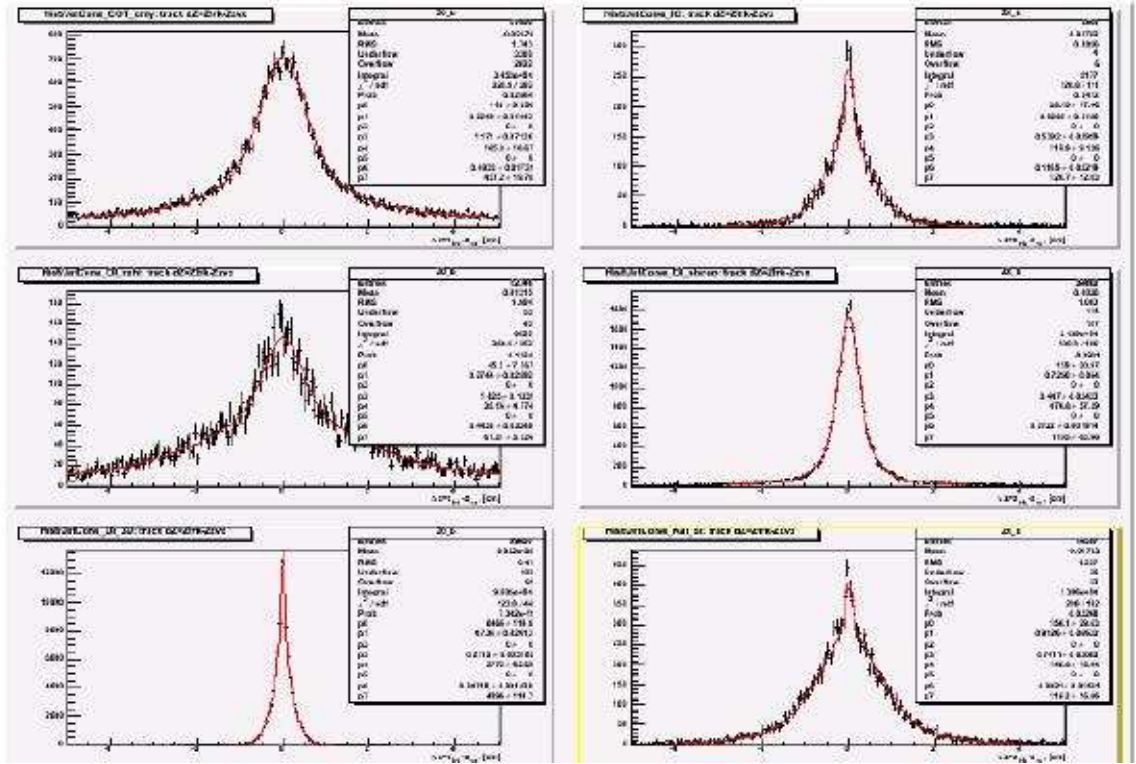
Figure 4-2. The Δz distribtuions for tracks reconstructed with different track reconstruction algorithms. The data are fit to a sum of two "Gaussians" to determine the width, $\sigma_{\Delta z}$, of the distributions, used in the event selection.

Table 4-5. Measurement of the k_T distributions: dijet mass bins boundaries, average invariant dijet mass $\langle M_{jj} \rangle$ and number of events in each bin after the event selection cuts.

Bin	Low edge (GeV/c^2)	High edge (GeV/c^2)	$\langle M_{jj} \rangle$ (GeV/c^2)	Number of events
1	66	95	76	17834
2	95	132	108	101619
3	132	180	149	23639
4	180	243	202	114437
5	243	323	272	26470
6	323	428	361	23742
7	428	563	475	38306
8	563	737	620	6638
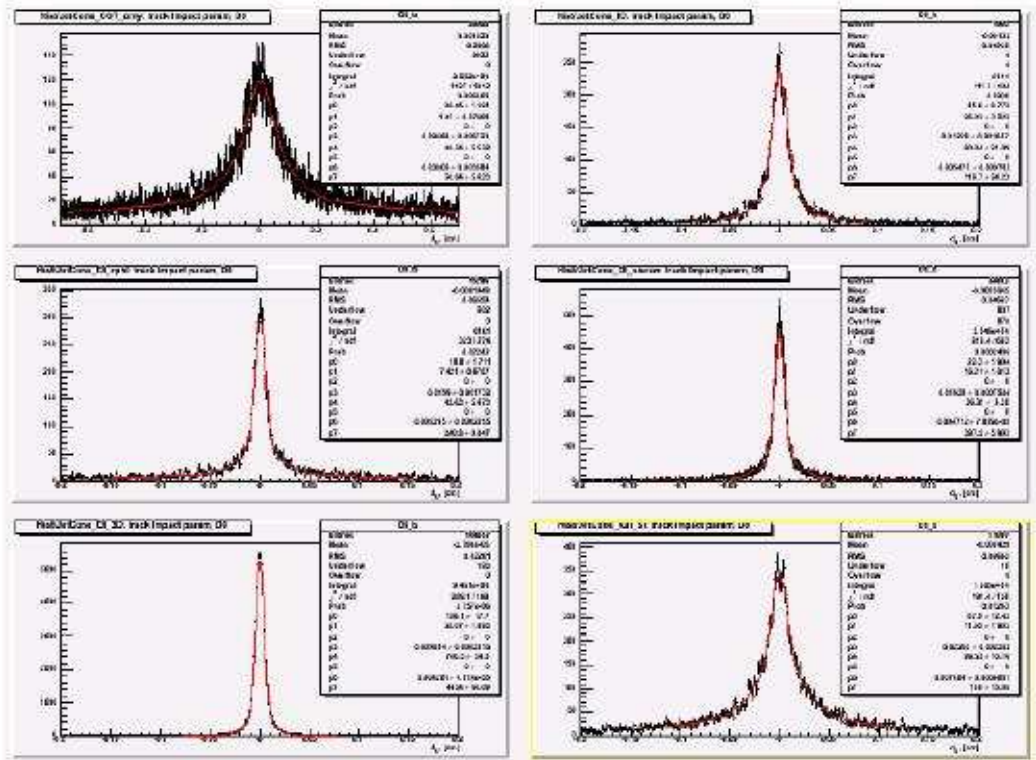
Figure 4-3. The impact parameter distribtuions for tracks reconstructed with different track reconstruction algorithms. The data are fit to a sum of two "Gaussians" to determine the width, σ_{d_0}, of the distributions, used in the event selection.
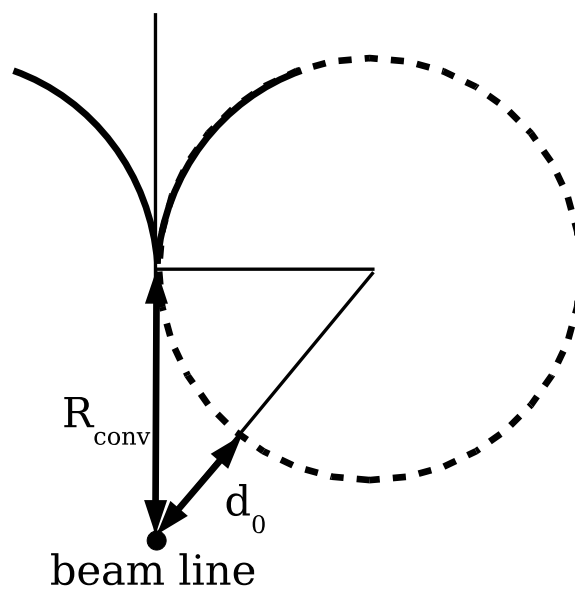
Figure 4-4. Illustration of the distance R_{conv} from the beam line to the point where the conversion occurred. Here, d_0 is the impact parameter.
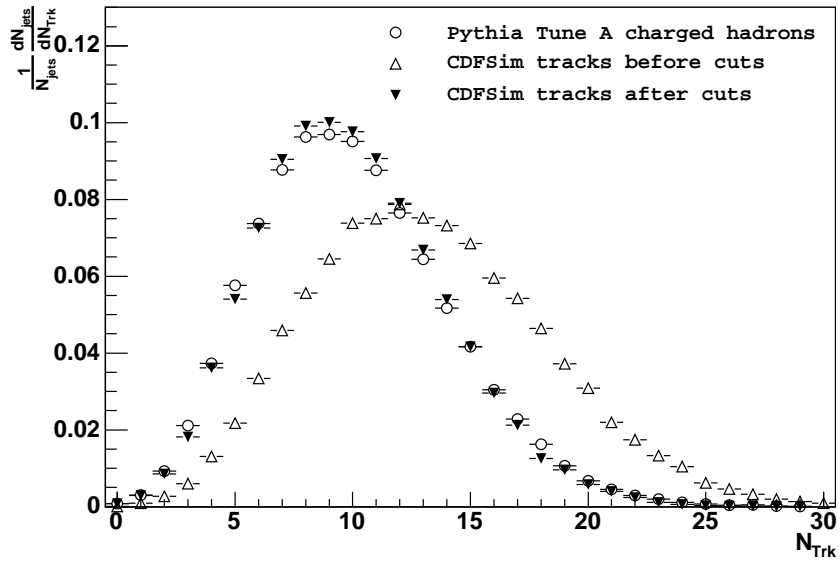
Figure 4-5. Monte Carlo track multiplicity in jets before and after applying track quality cuts. The distributions are for the dijet mass bin with $Q = 50$ GeV. Particles are counted within a cone of opening angle $\theta_c = 0.5$ radians. CDFSim refers to the full CDF data simulation.
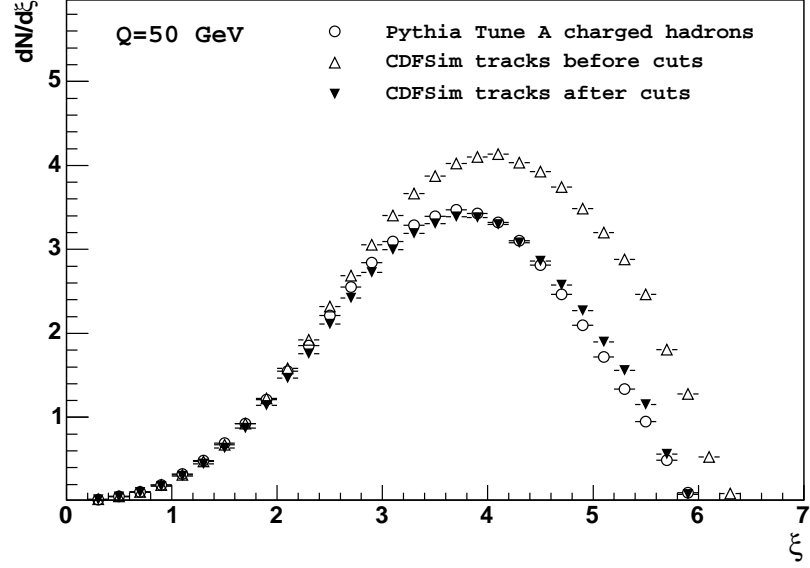
Figure 4-6. Inclusive momentum distributions of Monte Carlo tracks in jets before and after applying track quality cuts. The distributions are for the dijet mass bin with $Q = 50$ GeV. Particles are counted within a cone of opening angle $\theta_c = 0.5$ radians. CDFSim refers to the full CDF data simulation.
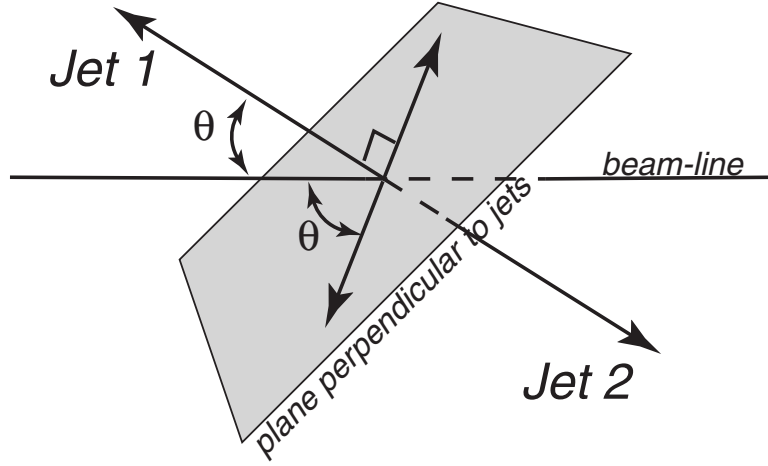
Figure 4-7. Illustration of the definition of complementary cones. The unlabeled arrows are the axes of the cones complementary to jets 1 and 2

CHAPTER 5
RESULTS

In this chapter we present experimental results of the measurement of the two-particle momentum correlations, as well as the measurement of the k_T distributions of particles in jets. The results are compared to the theoretical predictions obtained in the framework of the Analytical Perturbative Approach to jet fragmentation. Comparisons to the predictions by the Monte Carlo generators are also presented.

5.1   Two-particle Momentum Correlations

5.1.1   NLLA Fits to Data

The two-particle momentum correlation distributions $C(\Delta\xi_1, \Delta\xi_2)$ are produced for seven bins of dijet mass and do show the ridge-like shape as predicted by theory.

In this dissertation we plot the central diagonal profiles $\Delta\xi_1 = -\Delta\xi_2$ and $\Delta\xi_1 = \Delta\xi_2$ (shown in Fig. 2-5) of distributions. Figures 5-1-5-7 show the distributions corresponding to the dijet mass bins with $Q = 19, 27, 37, 50, 68, 90,$ and 119 GeV, respectively. The bin size $\Delta\xi = 0.2$ is chosen to be much wider than the momentum resolution in the fitted range. Smaller error bars correspond to the statistical uncertainty only, while the larger error bars correspond to both the statistical and systematic uncertainties added in quadrature. The 2-dimensional momentum correlation distribution is fit according to Eq. 2–18 with three free parameters c_0, c_1, and c_2. The solid line shows the profile of the fit function. The extracted values of fit parameters are given in Table 5-1. The fit range $-1 < \Delta\xi < 1$ is motivated by the region of validity of the NLLA calculations.

The dash-dotted lines correspond to the theoretical curves given by Eq. 2–18 for $Q_{eff} = 180 \pm 40$ MeV, extracted from fits of the inclusive momentum distributions (see A). The dashed lines correspond to the results of the Perez-Ramos calculation for the value

of $Q_{eff} = 230 \pm 40$ MeV extracted from fits of the inclusive momentum distributions to the MLLA function [23]. The fraction of gluon jets in the sample, used to model the theoretical prediction for quark and gluon jets, is obtained using PYTHIA tune A with CTEQ5L parton distribution functions [56].

The systematic uncertainty due to the parton distribution functions is evaluated by comparing results for the fraction of gluon jets f_g obtained using the CTEQ5L and the CTEQ6.1 [57] PDF sets. The systematic uncertainty due to the value of r was evaluated by taking a difference between the theoretical ($r_{theory} = 9/4$) and experimentally measured ($r_{exp} = 1.8$) [24] values and propagating it to the value of Q_{eff}. Both systematic uncertainties were found to be negligible.

The overall qualitative agreement between the data and the NLLA calculation [27] is very good. The data follow theoretical trends, indicating an enhanced probability of finding two particles with the same value of momenta (indicated by the parabolic shape of the $\Delta\xi_1 = -\Delta\xi_2$ diagonal profile with its maximum at $\Delta\xi_1 = \Delta\xi_2$). This effect becomes larger for particles with lower momenta (the positive slope of the $\Delta\xi_1 = \Delta\xi_2$ diagonal profile). An offset in the overall level of correlation is observed in all seven dijet mass bins, indicating that the Fong-Webber prediction overestimates the parameter c_0 of the correlation. The MLLA curves [28] qualitatively show the same trends; however, the quantitative disagreement is obviously larger for the MLLA predictions compared to the NLLA predictions [27].

Fig. 5-8 shows the evolution of parameters c_0, c_1 and c_2 with jet hardness Q. Each data point corresponds to the value of one parameter measured in a particular dijet mass bin. The distributions are fit to the NLLA function with Q_{eff} treated as the only free parameter. The fits are represented by solid lines. Theoretical curves for pure quark

and gluon jets in the final state are also shown. We used the results of the Fong-Webber calculation [27] to fit the evolution of these parameters with jet hardness and to extract the parameter Q_{eff}.

The value of Q_{eff} obtained from the fit of c_1 is $145 \pm 10(\text{stat})^{+79}_{-65}(\text{syst})$ MeV. The value of Q_{eff} obtained from the fit of c_2 is $129 \pm 12(\text{stat})^{+86}_{-71}(\text{syst})$ MeV. The average value of Q_{eff} extracted from the fits of c_1 and c_2 is 137^{+85}_{-69} MeV and is consistent with Q_{eff} extracted from the fits of inclusive particle momentum distributions. The dependence of c_0 on Q has an offset of $\sim$0.06, however this parameter is sensitive to the peak position of the inclusive momentum distribution ξ_0. In the data we measure correlation distributions around the true ξ_0, while theoretical predictions completely neglect all terms beyond $\tau/2$ in Eq.(2–4) as well as the parameter $O(1) = -0.6$. Therefore only its evolution with energy and not the absolute value is controlled in theory. For these reasons we exclude c_0 from the measurement of Q_{eff}. A formal fit to the theoretical function gives the value $Q_{eff} = 0.1$ MeV. This value, however, does not have physical meaning as the distributions of c_0 vs. Q in data and theory are not in agreement. Other than the offset, c_0 shows very weak, if any, Q dependence, consistent with the theory.

5.1.2 Comparison to Monte Carlo

We compare the momentum correlation distributions of charged particles in data to Pythia Tune A and Herwig 6.5 predictions. Predictions of the two Monte Carlo generators are in good agreement with each other and with results obtained from data. Figs. 5-9-5-13 show the correlation distributions in data compared to Pythia Tune A and Herwig 6.5 predictions at the level of final stable charged hadrons.

5.2   The k_T Distributions

5.2.1   Comparison to MLLA and NMLLA predictions

The $dN/dln(k_T)$ distributions are produced for eight bins of dijet mass and are shown in Fig.5-14. The error bars correspond to statistical uncertainty only, while the shaded area corresponds to statistical and systematic uncertainties added in quadrature. The dashed line corresponds to the MLLA curve calculated according to [33] for the value of $Q_{eff} = 230$ MeV, extracted from fits of inclusive momentum distributions. The solid line corresponds to the NMLLA curve for the same value of Q_{eff}. The fraction of gluon jets in the sample, used to mix the theoretical prediction for quark and gluon jets, is obtained using Pythia Tune A with CTEQ5L parton distribution functions [56].

Systematic error due to the parton distribution function uncertainties is evaluated by comparing results for the fraction of gluon jets f_g obtained using CTEQ5L and CTEQ6.1 [57] PDF sets. This systematic uncertainty was found to be negligible.

The overall qualitative agreement between the data and the MLLA calculation results [33] is very good within the range of soft approximation. Beyond the range (at high k_T), however, the MLLA predictions fail to reproduce data, predicting more particles with high values of k_T. The validity range of the soft approximation becomes larger with increasing energy and, as expected, the discrepancy between data and MLLA predictions decreases. The NMLLA predictions [34] provide good description of the CDF data over the entire range of jet energies. The fact that the hadron level distributions can be successfully described by the perturbative predictions made for partons suggests that the properties of jets are primarily determined at the partonic stage of an event and these properties are not altered significantly in the process of hadronization.

5.2.2   Comparison to Monte Carlo

We compare $dN/dln(k_T)$ distributions of charged particles in data to Pythia Tune A and Herwig 6.5 predictions. Predictions of Monte-Carlo generators are in agreement with each other and with results obtained in data. Fig.5-15 shows distributions in data compared to Pythia Tune A and Herwig 6.5 predictions at the level of final stable particles.

Both Monte Carlo generators use Leading Log Approximation precision to describe the process of parton showering. Despite the fact that MLLA predictions (which are obtained with Next-to-Leading Log precision) show significant deviation from the data at large values of $\ln(k_T)$, the agreement between the CDF data and the Monte Carlo predictions is very good. This suggests that hadronization parameters in Pythia and Herwig were heavily tuned to reproduce the data in the entire range of particle k_T.

Table 5-1. Summary of the correlation parameters c_0, c_1 and c_2 measured in seven dijet mass bins. The first uncertainty is statistical, the second one is systematic.

Q (GeV)	c_0	c_1	c_2
19	$1.078 \pm 0.007 \pm 0.016$	$0.081 \pm 0.006 \pm 0.016$	$-0.047 \pm 0.006 \pm 0.008$
27	$1.076 \pm 0.003 \pm 0.022$	$0.068 \pm 0.002 \pm 0.015$	$-0.038 \pm 0.002 \pm 0.012$
37	$1.075 \pm 0.005 \pm 0.018$	$0.057 \pm 0.004 \pm 0.013$	$-0.031 \pm 0.004 \pm 0.012$
50	$1.079 \pm 0.002 \pm 0.019$	$0.051 \pm 0.002 \pm 0.014$	$-0.029 \pm 0.002 \pm 0.010$
68	$1.081 \pm 0.004 \pm 0.028$	$0.040 \pm 0.004 \pm 0.012$	$-0.027 \pm 0.004 \pm 0.011$
90	$1.081 \pm 0.005 \pm 0.023$	$0.046 \pm 0.004 \pm 0.015$	$-0.024 \pm 0.004 \pm 0.014$
119	$1.077 \pm 0.004 \pm 0.033$	$0.028 \pm 0.003 \pm 0.013$	$-0.019 \pm 0.003 \pm 0.015$
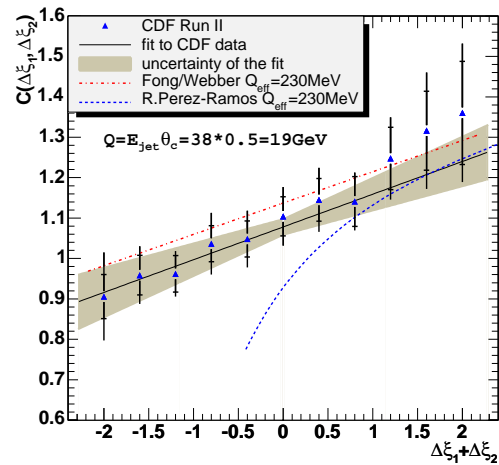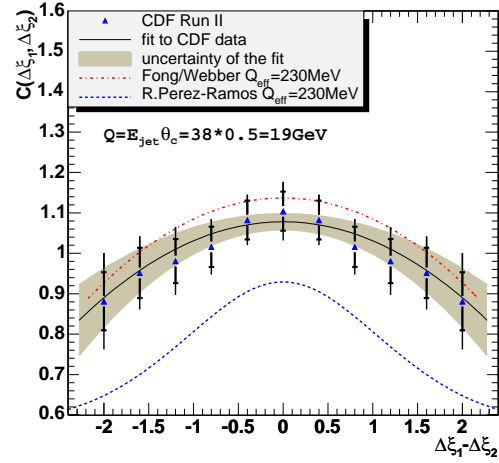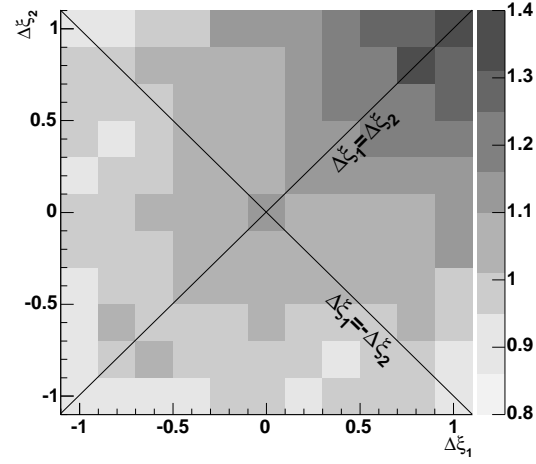
Figure 5-1. Two-particle momentum correlations in jets in the restricted cone of size $\theta_c = 0.5$ radians for dijet mass bin 3 with $Q = 19$ GeV (top). Central diagonal profiles $\Delta\xi_1 = -\Delta\xi_2$ (middle) and $\Delta\xi_1 = \Delta\xi_2$ (bottom) of the distributions are shown. The correlation in data is compared to that of theory as calculated by C.P. Fong and B.R. Webber for $Q_{eff} = 180$ MeV and as calculated by R. Perez-Ramos for $Q_{eff} = 230$ MeV.
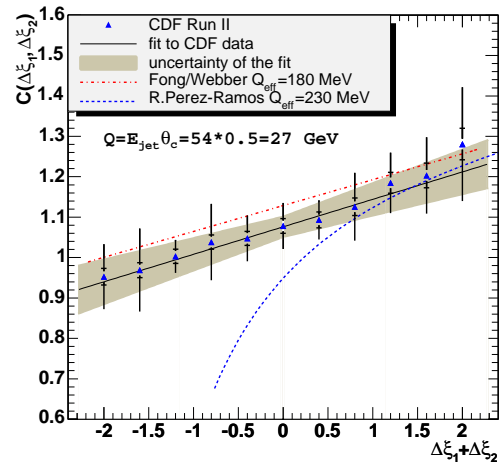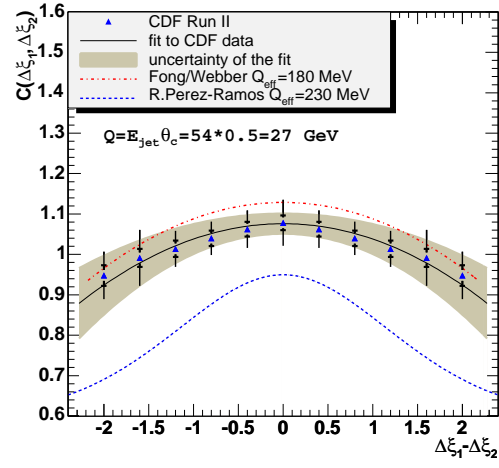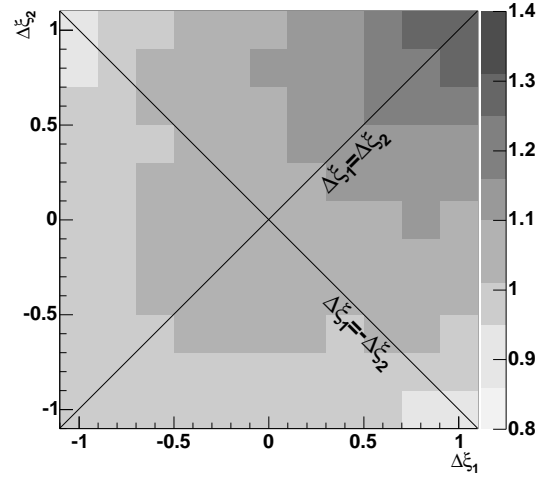
Figure 5-2. Same as in Fig. 5-1 for $Q = 27$ GeV.
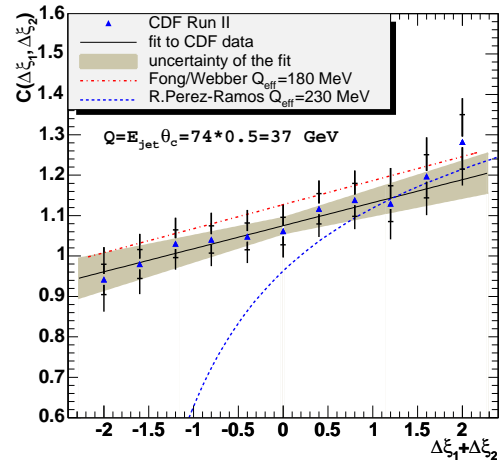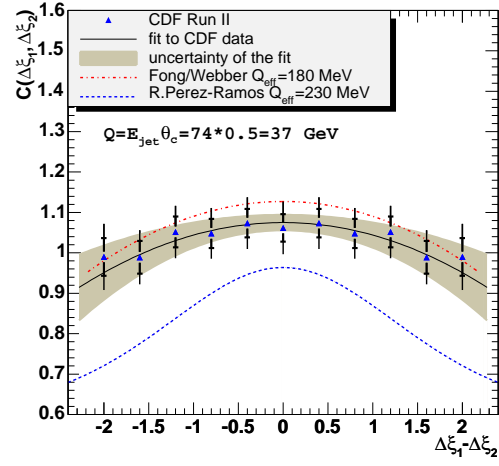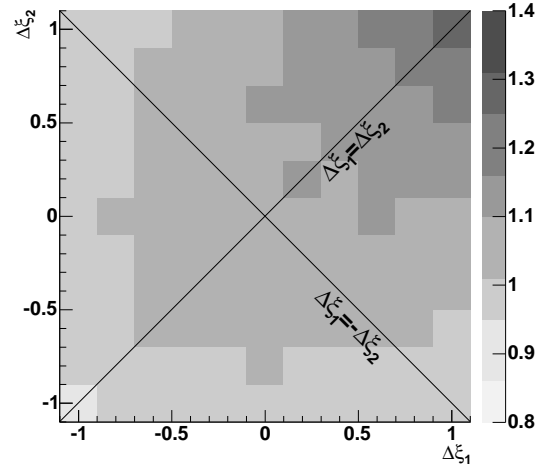
Figure 5-3. Same as in Fig. 5-1 for $Q = 37$ GeV.
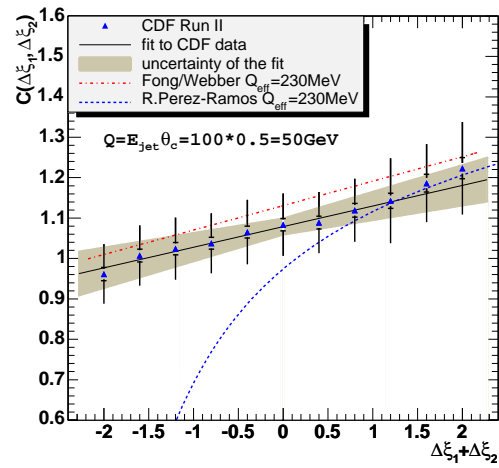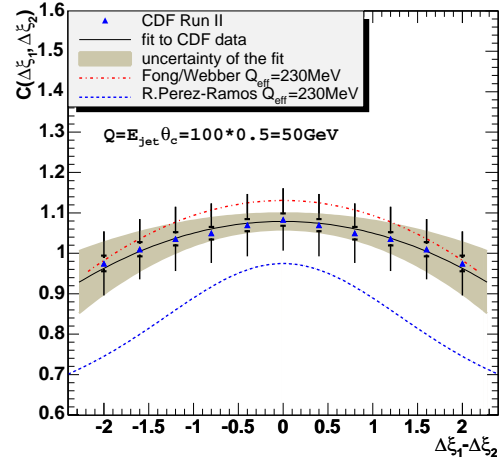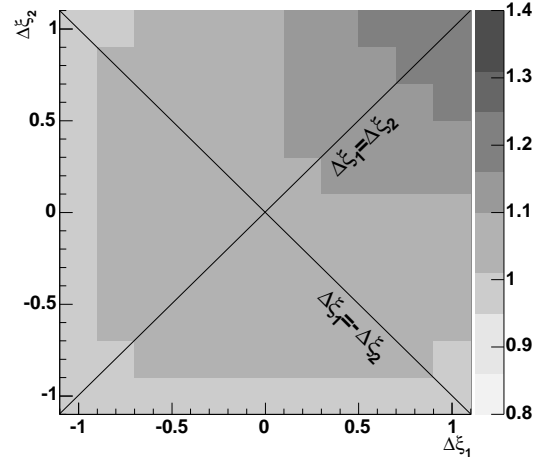
Figure 5-4. Same as in Fig. 5-1 for $Q = 50$ GeV.
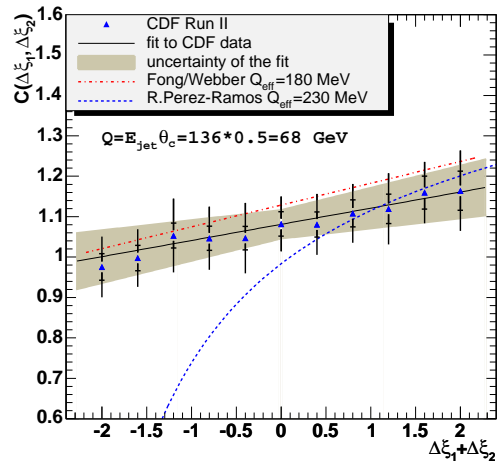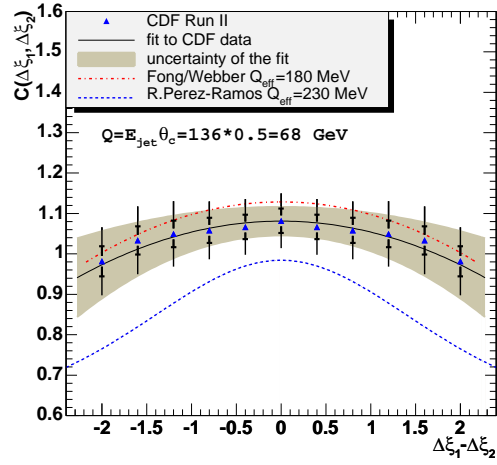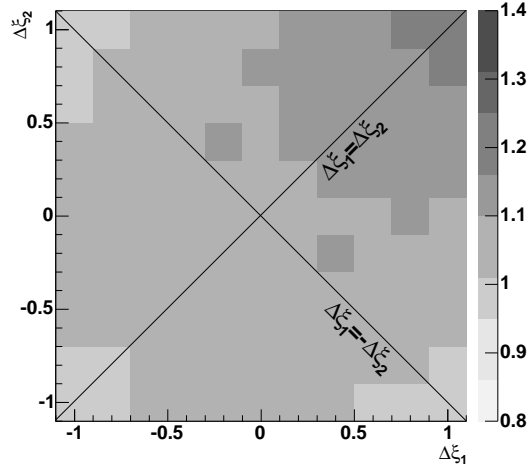
Figure 5-5. Same as in Fig. 5-1 for $Q = 68$ GeV.
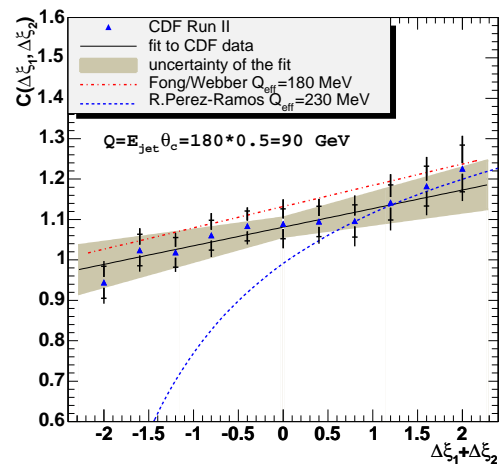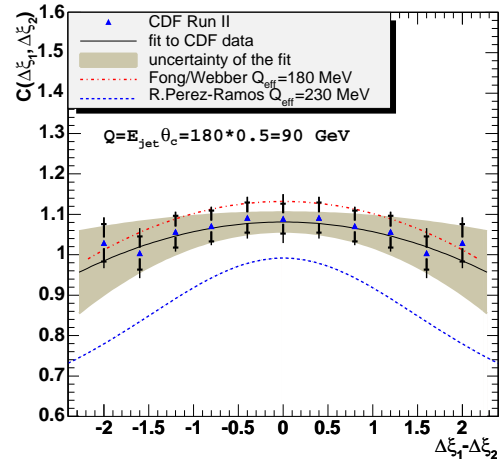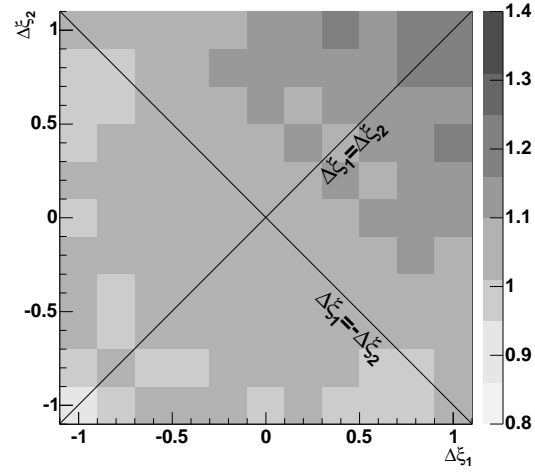
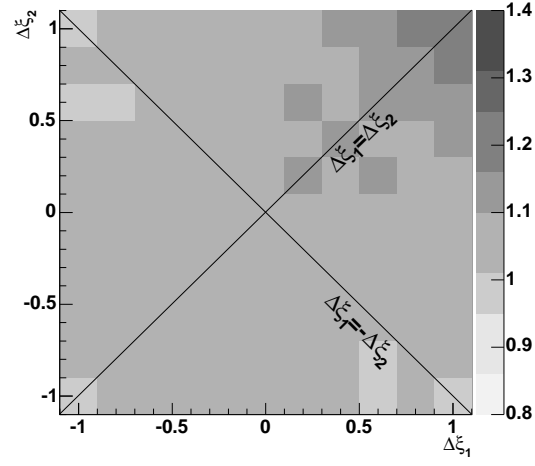Figure 5-6. Same as in Fig. 5-1 for $Q = 90$ GeV.
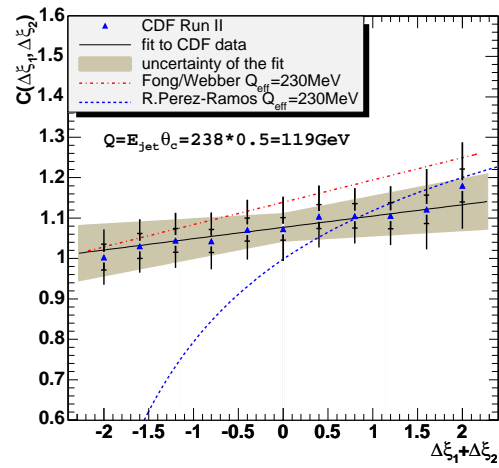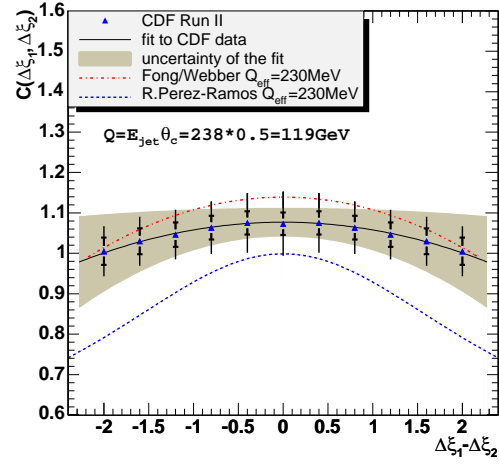
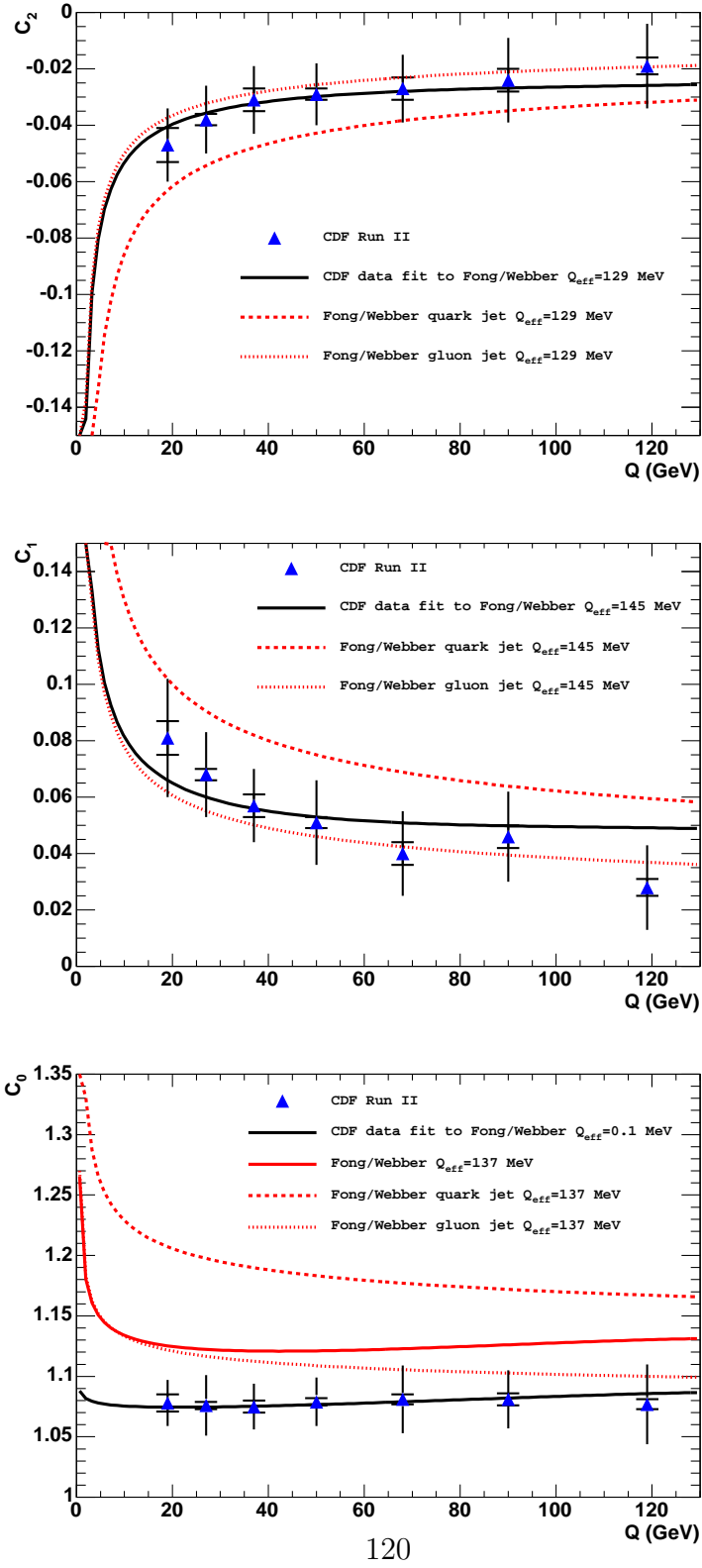Figure 5-7. Same as in Fig. 5-1 for $Q = 119$ GeV.

Figure 5-8. The evolution of correlation parameters c_2, c_1, and c_0 with jet energy. CDF data points are fit to the NLLA function as calculated by C.P. Fong and B.R. Webber. A value of Q_{eff} is extracted from each of these fits separately. The NLLA predictions for pure quark and pure gluon jet samples are also shown.
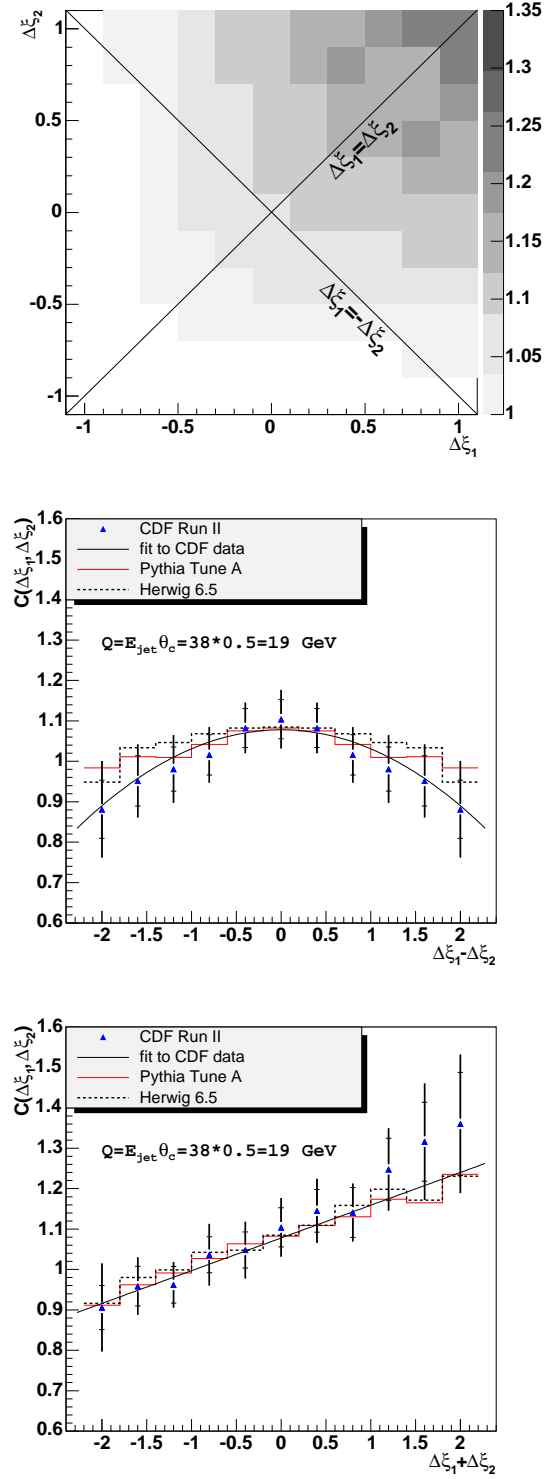
Figure 5-9. Hadron-level two-particle momentum correlations in jets in the restricted cone of size $\theta_c = 0.5$ radians for the dijet mass bin with $Q = 19$ GeV by the Pythia Tune A (top). The correlation in data is compared to the hadron momentum correlations by the Pythia Tune A and Herwig 6.5 event generators. Central diagonal profiles $\Delta\xi_1 = -\Delta\xi_2$ (middle) and $\Delta\xi_1 = \Delta\xi_2$ (bottom) of the distributions are shown.
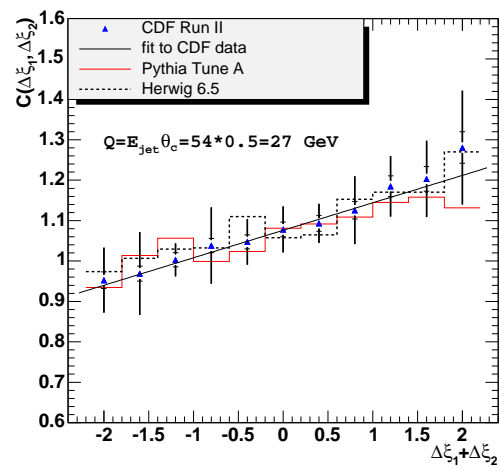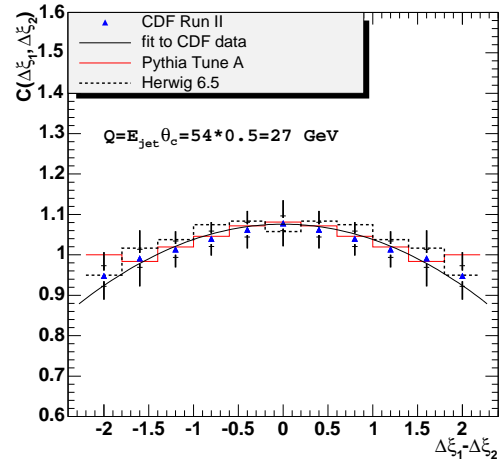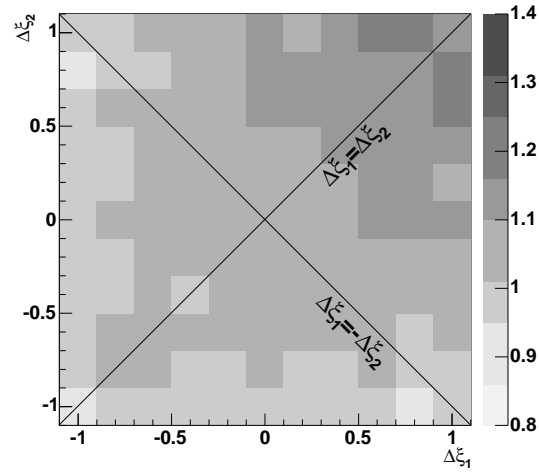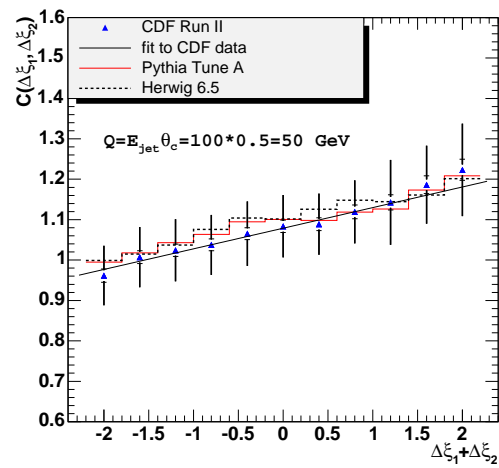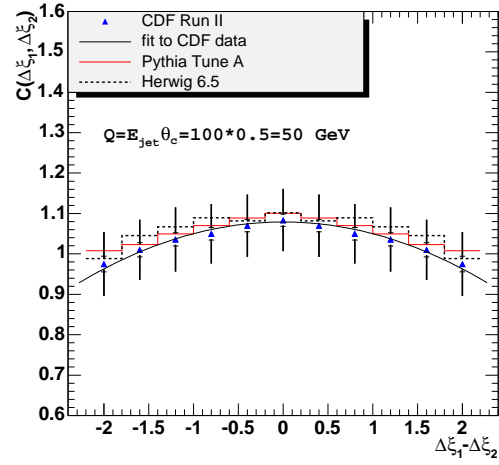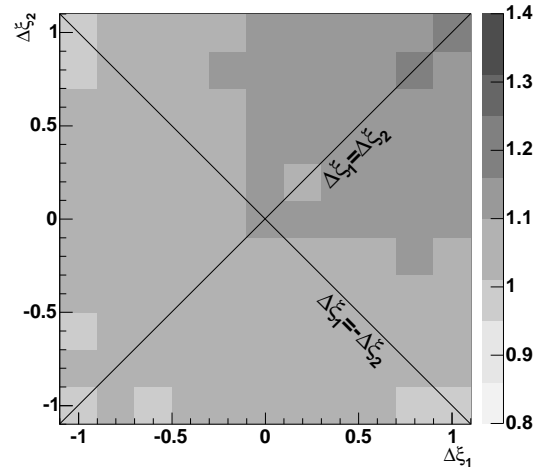
Figure 5-10. Same as in Fig. 5-9 for $Q = 27$ GeV.

Figure 5-11. Same as in Fig. 5-9 for $Q = 50$ GeV.
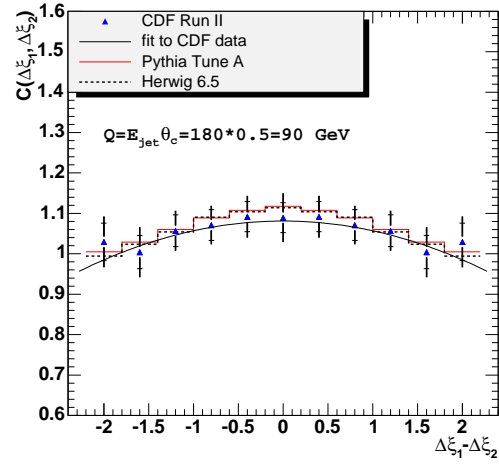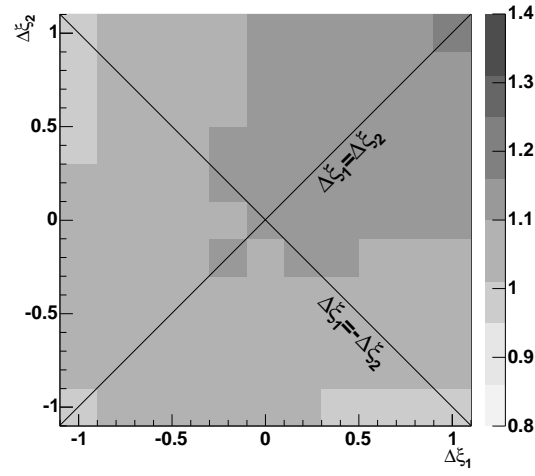
Figure 5-12. Same as in Fig. 5-9 for $Q = 90$ GeV.

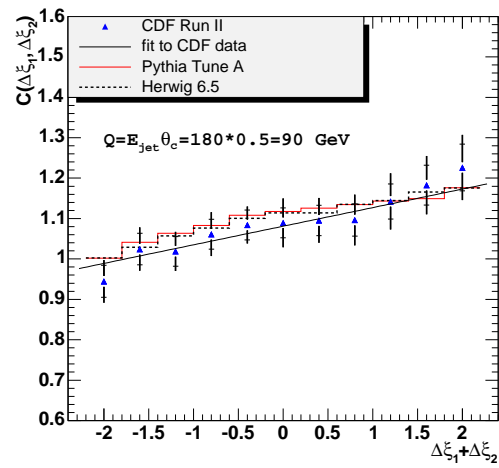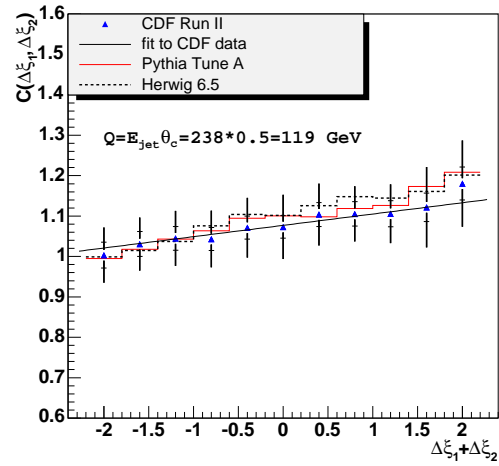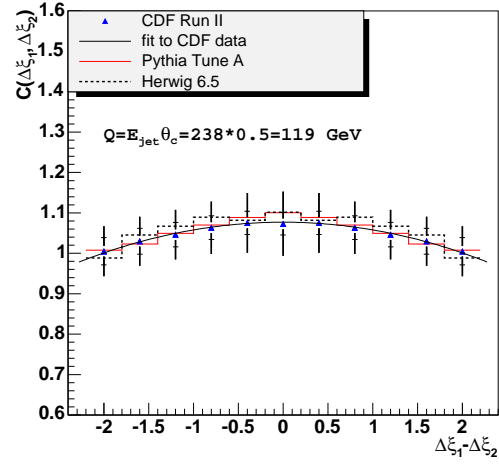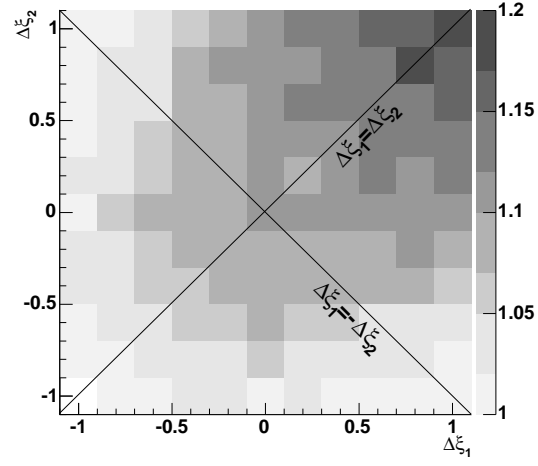Figure 5-13. Same as in Fig. 5-9 for $Q = 119$ GeV.

125

126
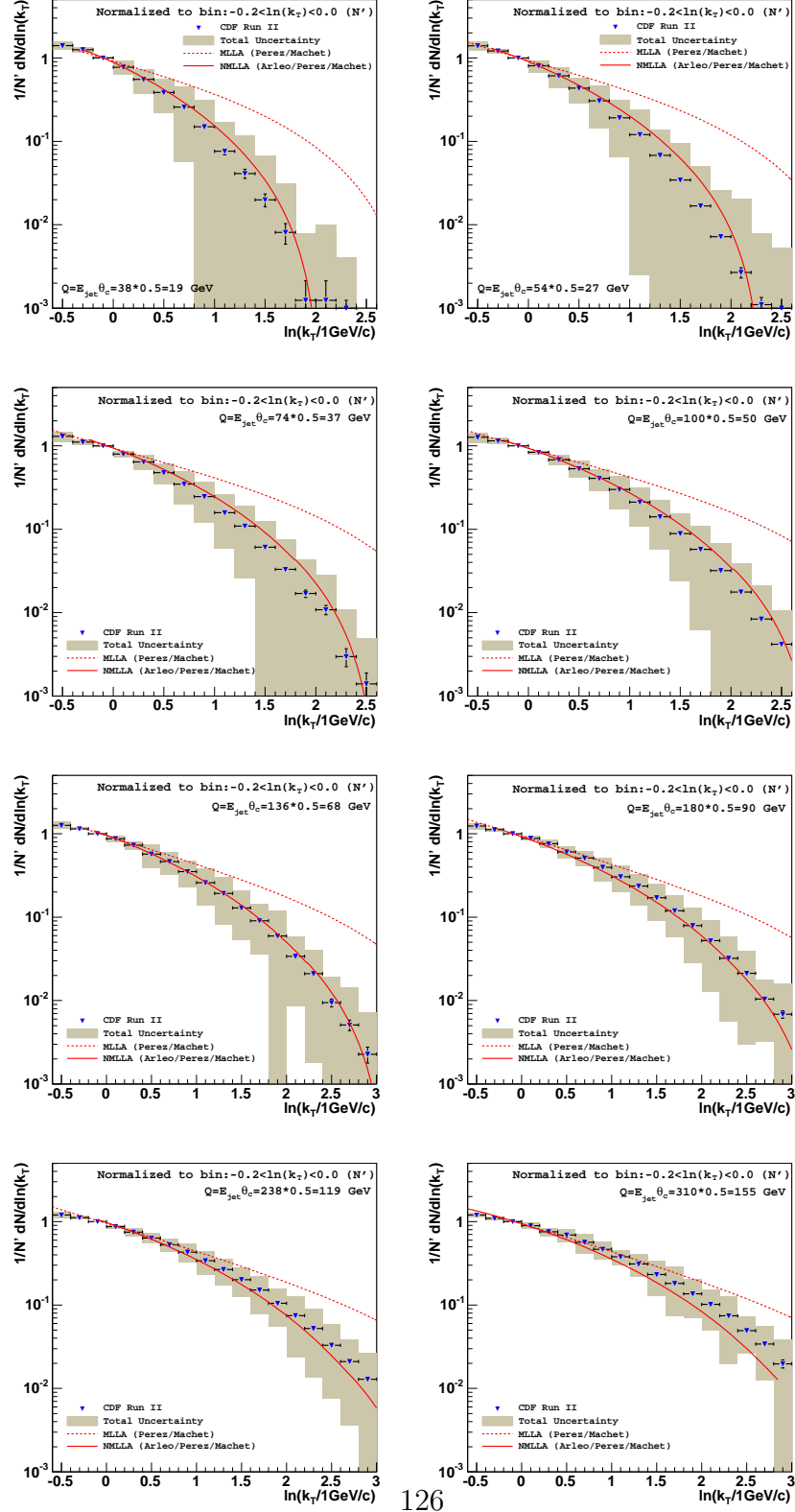
Figure 5-14. $dN/dln(k_T)$ distributions of particles in in the restricted cone of size $\theta_c = 0.5$ around jet axis in eight dijet mass bins. CDF data compared to the analytical MLLA (dashed line) and NMLLA (solid line) predictions.
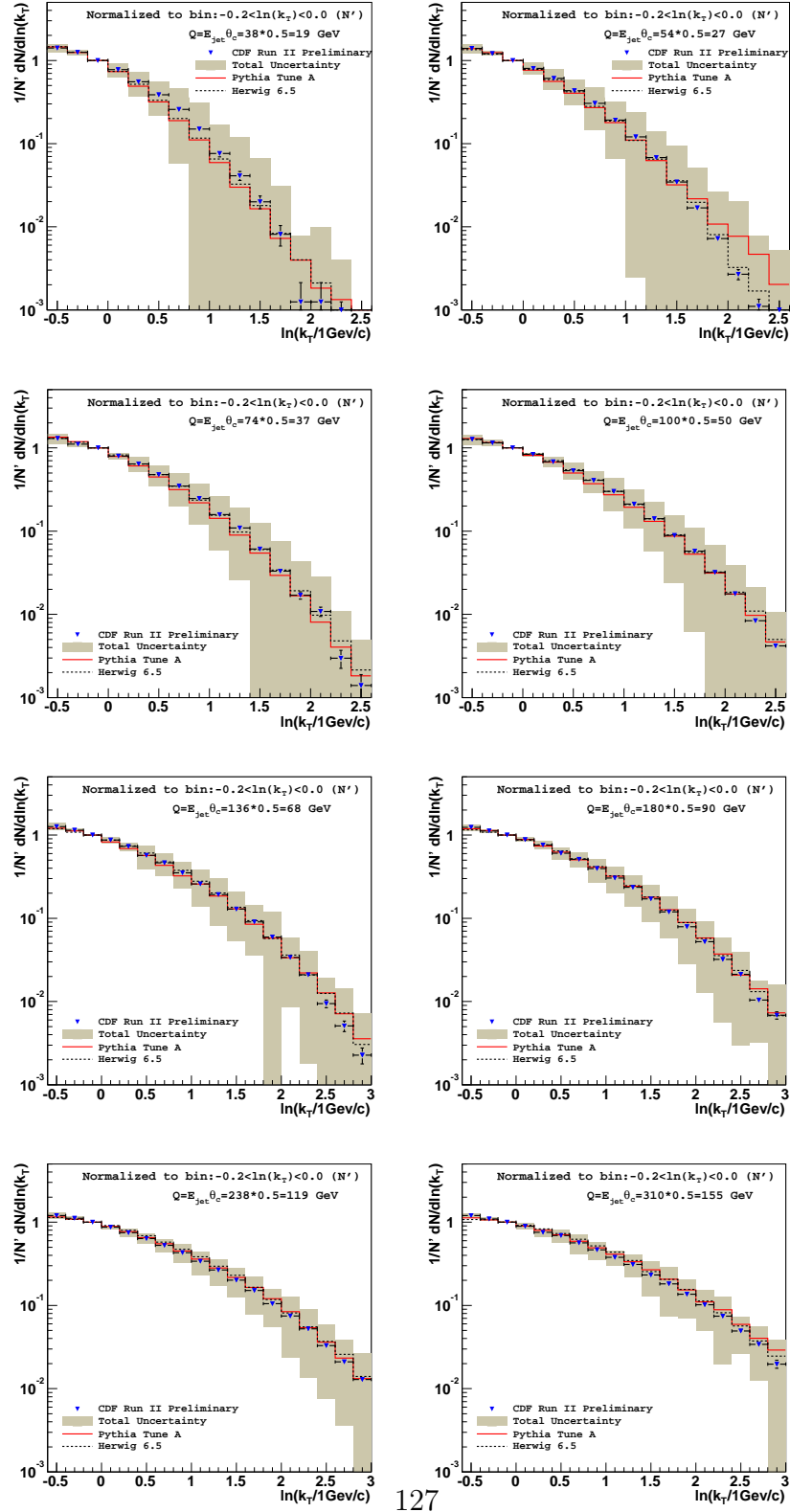
Figure 5-15. $dN/dln(k_T)$ distributions of particles in the restricted cone of size $\theta_c = 0.5$ around jet axis in eight dijet mass bins. CDF II data compared to the predictions by Pythia Tune A and Herwig 6.5 Monte Carlo generators.

CHAPTER 6
CONCLUSIONS

The two-particle momentum correlation distributions of charged particles in jets from dijet events were measured over a wide range of dijet masses from 66 to 563 GeV/c^2. The jets were produced in $p\bar{p}$ collisions at a center of mass energy of 1.96 TeV. The measurements were performed for particles in a restricted cone around the jet direction with opening angle $\theta_c = 0.5$ radians.

The data are compared to the Next-to-Leading-Log Approximation calculations combined with the hypothesis of Local Parton-Hadron Duality (LPHD). Overall, the data and the theory showed the same trends over the entire range of dijet energies. The parton shower cut-off scale Q_{eff} is extracted from fits of the evolution of the correlation parameters, c_0, c_1, and c_2, defining the strength of the correlation. The average value of Q_{eff} extracted from the fits of c_1 and c_2 is 137^{+85}_{-69} MeV and is consistent with Q_{eff} extracted from the fits of inclusive particle momentum distributions. As predicted, the parameter c_0 shows little, if any, dependence on jet energy; however, we observe a substantial systematic offset between the experimental and theoretical values.

We also measured transverse momenta of particles with respect to jet axis in dijet events in a wide range of masses 66-737 GeV/c^2. The measurement was done for particles in a restricted cone around the jet direction with opening angle $\theta_c = 0.5$ radians.

The data was compared to the Modified Leading Log and Next-to-Modified Leading Log Approximation calculations combined with the hypothesis of Local Parton-Hadron Duality. Within the range of the soft approximation, data and theory show same trends in the entire range of dijet energies. Above the range, MLLA predicts more hard particles

than observed in data. NMLLA shows good agreement with data in the entire range of k_T and dijet energies.

Predictions by Monte-Carlo event generators, Pythia Tune A and Herwig 6.5, were compared to the experimental data, and were found to reproduce the correlations and k_T distributions in data fairly well. Both Monte Carlo generators use Leading Log Approximation precision to describe the process of parton showering. Despite the fact that MLLA predictions (which are obtained with Next-to-Leading Log precision) show significant deviation from the data at large values of $\ln(k_T)$, the agreement between the CDF data and the Monte Carlo predictions is very good. This suggests that hadronization parameters in Pythia and Herwig were heavily tuned to reproduce the data in the entire range of particle k_T.

Overall, the results of both analysis indicate that the perturbative stage of the jet formation is dominant, giving further support to the hypothesis of LPHD.

APPENDIX A
INCLUSIVE MOMENTUM DISTRIBUTIONS OF PARTICLES IN JETS

In this data analysis we also measure inclusive momentum distributions of particles in jets in Run II. Previously these distributions were measured in CDF Run I and the data were fit to the theoretical MLLA function to extract the parameter Q_{eff}. Detailed description and results of the CDF Run I analysis can be found in [23]. In this note we fit the data to the Fong-Webber NLLA function Eq. (2–4). Due to natural differences in the two theoretical approaches the extracted values of Q_{eff} do not have to match, however they are expected to be of the same order. The principal difference between the Fong-Webber and the MLLA predictions is that Fong-Webber function contains one extra parameter $O(1)$-an uncertainty in the peak position of the distribution. This uncertainty is not controlled by theory. Therefore while in MLLA parametrization Q_{eff} controls both peak position and width of the distribution, in Fong-Webber's it controls only the width while the $O(1)$ parameter effectively controls the peak position.

Event and track selection, as well as the evaluation of systematic uncertainties is done in the same fashion as for the measurement of the two-particle momentum correlation distributions. The only effect accounted differently is tracking inefficiency. This is due to the fact that momentum distributions are expected to be more sensitive to inefficiency effects than the correlations. High efficiency of track reconstruction is ensured by selecting events with central jets and eliminating poorly reconstructed and spurious tracks. However, there still may be some non-reconstructed tracks inside jets. The tracking inefficiency varies as a function of the distance between track and jet axis in the $\eta - \phi$ space and transverse momenta of both jet and track. The detailed studies have been performed [55] to measure the track reconstruction inefficiency inside jets as a function of

130

r and the jet and track transverse momenta, using track embedding techniques. We used Pythia Tune A and the results of these studies to simulate inefficiency effects by loosing Monte Carlo tracks according to the parametrization obtained in [55]. A correction factor is then produced for each dijet mass bin by taking the ratio of the inclusive momentum distributions in Monte Carlo with and without simulated inefficiency. The correction factors for various energies are shown in Fig. A-1. The corresponding correction factors are then applied to the distributions in data. The difference between distributions in data, with and without this scale factor applied, is assigned as the systematic uncertainty.

The inclusive momentum distributions $D(\xi) = \frac{dN}{d\xi}$ in all seven experimental dijet mass bins are simultaneously fit to the theoretical Fong-Webber function. In the fit the Q_{eff} and $O(1)$ parameters are required to have same value in all dijet mass bins while normalization parameter $N(Q)$ is allowed to vary from one bin to another. Figure A-2 shows the distributions in data corresponding to the dijet mass bins with $Q = 27$, 50, and 90 GeV, respectively. The error bars correspond to both the statistical and systematic uncertainties added in quadrature. The solid curves correspond to the fit of CDF data to the theoretical Fong-Webber function. The extracted values of the fit parameters are $Q_{eff} = 180 \pm 40$ MeV and $O(1) = -0.6 \pm 0.1$.
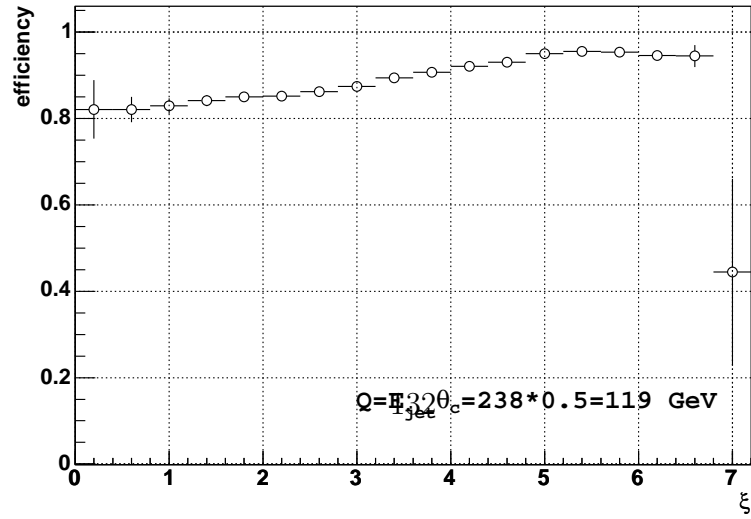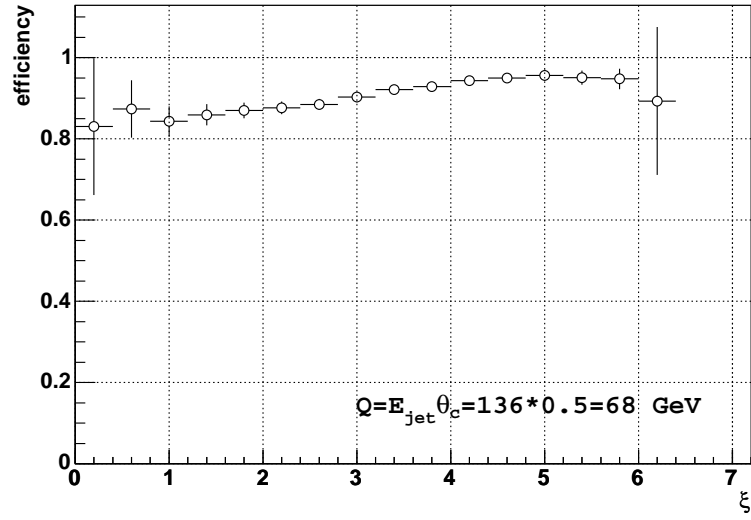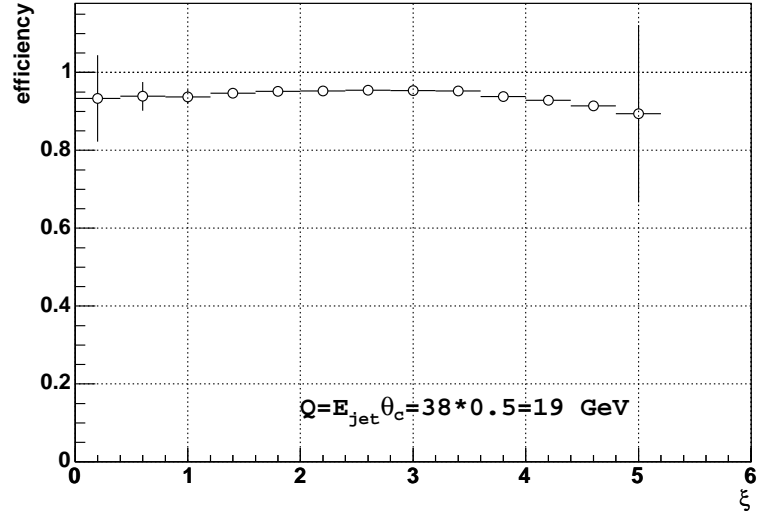
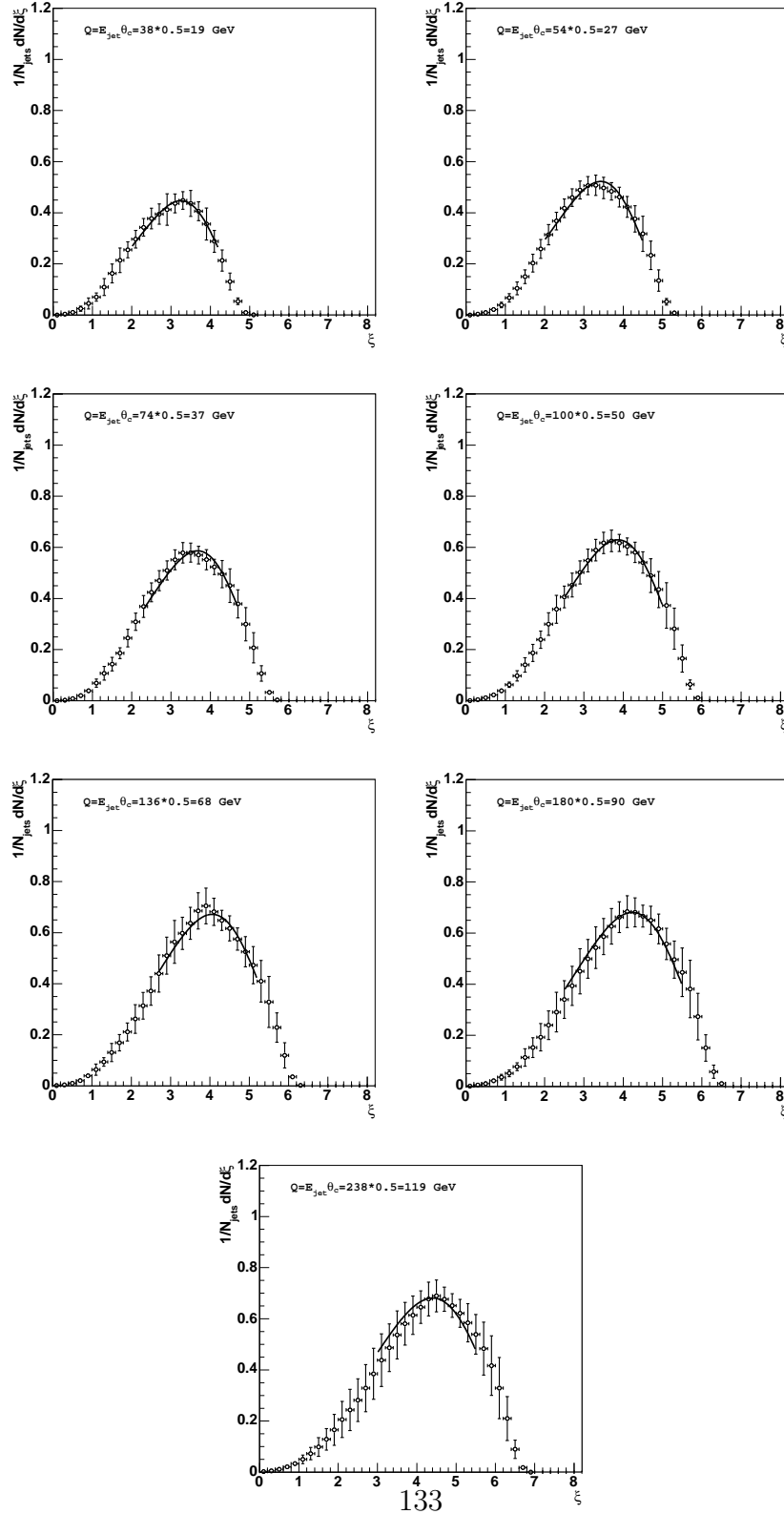Figure A-1. Tracking efficiency correction factors as functions of ξ for three dijet mass bins.

Figure A-2. Inclusive momentum distributions of particles in jets. Distributions in data are fit to theoretical fucntion as calculated by C.P. Fong and B.R. Webber.

REFERENCES

[1] J. F. Donoghue, E. Golowich and B. R. Holstein, "Dynamics Of The Standard Model," Camb. Monogr. Part. Phys. Nucl. Phys. Cosmol. **2**, 1 (1992).

[2] M. E. Peskin and D. V. Schroeder, "An Introduction To Quantum Field Theory," *Reading, USA: Addison-Wesley (1995) 842 p.*

[3] C. Quigg, Front. Phys. **56**, 1 (1983).

[4] A. Salam and J. C. Ward, Phys. Lett. **13**, 168 (1964).

[5] S. Weinberg, Phys. Rev. Lett. **19**, 1264 (1967).

[6] F. Halzen and A. D. Martin, *New York, Usa: Wiley (1984) 396p*

bibitemQCD2 R. D. Field, *Redwood City, USA: Addison-Wesley (1989) 366 p. (Frontiers in physics, 77)*

[7] P. W. Higgs, Phys. Lett. **12**, 132 (1964).

[8] M. Gell-Mann, Phys. Lett. **8**, 214 (1964).

[9] O. W. Greenberg, Phys. Rev. Lett. **13**, 598 (1964).

[10] D. J. Gross and F. Wilczek, Phys. Rev. Lett. **30**, 1343 (1973).

[11] H. D. Politzer, Phys. Rev. Lett. **30**, 1346 (1973).

[12] Y. L. Dokshitzer, V. Khoze, A. Mueller, and S. Troyan, Basics of Perturbative QCD, edited by J. Tran Thanh Van (Editions Frontières, Gif-sur-Yvette, 1991).

[13] Y. I. Azimov, Y. L. Dokshitzer, V. A. Khoze and S. I. Troian, Z. Phys. C **27**, 65 (1985); ibid. C **31**, 213 (1986).

[14] V. N. Gribov and L. N. Lipatov, Sov. J. Nucl. Phys. **15**, 438 (1972) [Yad. Fiz. **15**, 781 (1972)]; G. Altarelli and G. Parisi, Nucl. Phys. B **126**, 298 (1977); Y. L. Dokshitzer, Sov. Phys. JETP **46**, 641 (1977) [Zh. Eksp. Teor. Fiz. **73**, 1216 (1977)].

[15] W. Furmanski, R. Petronzio and S. Pokorski, Nucl. Phys. B **155**, 253 (1979). D. Amati, A. Bassetto, M. Ciafaloni, G. Marchesini and G. Veneziano, Nucl. Phys. B

173, 429 (1980); Y. L. Dokshitzer, V. S. Fadin and V. A. Khoze, Phys. Lett. B **115**, 242 (1982).

[16] B. I. Ermolaev and V. S. Fadin, JETP Lett. **33**, 269 (1981) [Pisma Zh. Eksp. Teor. Fiz. **33**, 285 (1981)]; A. H. Mueller, Phys. Lett. B **104**, 161 (1981).

[17] Y. L. Dokshitzer and S. I. Troian, "Nonleading Perturbative Corrections To The Dynamics Of Quark - Gluon Cascades And Soft Hadron Spectra In E+ E-Annihilation,"; A. H. Mueller, Nucl. Phys. B **228**, 351 (1983).

[18] G. Alexander *et al.* (OPAL Collaboration), Phys. Lett. B **265**, 462 (1991);

[19] G. Alexander *et al.* (OPAL Collaboration), Phys. Lett. B **265**, 462 (1991); P. D. Acton *et al.* (OPAL Collaboration), Z. Phys. C **58**, 387 (1993); R. Akers *et al.* (OPAL Collaboration), Z. Phys. C **68**, 179 (1995); D. Buskulic *et al.* (ALEPH Collaboration), Phys. Lett. B **346**, 389 (1995); G. Alexander *et al.* (OPAL Collaboration), Phys. Lett. B **388**, 659 (1996); D. Buskulic *et al.* (ALEPH Collaboration), Phys. Lett. B **384**, 353 (1996); P. Abreu *et al.* (DELPHI Collaboration), Z. Phys. C **70**, 179 (1996); K. Ackerstaff *et al.* (OPAL Collaboration), Eur. Phys. J. C **1**, 479 (1998) [arXiv:hep-ex/9708029]; P. Abreu *et al.* (DELPHI Collaboration), Phys. Lett. B **449**, 383 (1999) [arXiv:hep-ex/9903073]; G. Abbiendi *et al.* (OPAL Collaboration), Eur. Phys. J. C **11**, 217 (1999) [arXiv:hep-ex/9903027]; Y. Iwasaki, for SLD Collaboration, SLAC-R-95-460, SLAC preprint, Stanford, 1995.

[20] J. B. Gaffney and A. H. Mueller, Nucl. Phys. B **250**, 109 (1985); S. Catani, Y. L. Dokshitzer, F. Fiorani and B. R. Webber, Nucl. Phys. B **377**, 445 (1992); A. Capella, I. M. Dremin, J. W. Gary, V. A. Nechitailo and J. Tran Thanh Van, Phys. Rev. D **61**, 074009 (2000) [arXiv:hep-ph/9910226]; S. Lupia and W. Ochs, Phys. Lett. B **418**, 214 (1998) [arXiv:hep-ph/9707393].

[21] A.H. Mueller, in Proc.1981 Int. Symp. on Lepton and Photon Interactions and Energies, ed. W. Pfeil (Bonn, 1981), p.689; Y. L. Dokshitzer, V. S. Fadin and V. A. Khoze, Phys. Lett. B **115**, 242 (1982); A. H. Mueller, Nucl. Phys. B **213**, 85 (1983); ibid B **241**, 141 (1984).

[22] A. A. Affolder *et al.* (CDF Collaboration), Phys. Rev. Lett. **87**, 211804 (2001).

[23] D. Acosta *et al.* (CDF Collaboration), Phys. Rev. D **68**, 012003 (2003).

[24] D. Acosta *et al.* (CDF Collaboration), Phys. Rev. Lett. **94**, 171802 (2005);
A. Pronko (CDF Collaboration), Int. J. Mod. Phys. A **20**, 3723 (2005); A. Pronko
(CDF collaboration), Acta Phys. Polon. B **36**, 451 (2005).

[25] Y. L. Dokshitzer, S.I. Troyan, XIX Winter School of LNPI, vol. 1, 144 (1984).

[26] Y. L. Dokshitzer, V. A. Khoze and S. I. Troian, Int. J. Mod. Phys. A **7**, 1875 (1992);
Y. L. Dokshitzer, V. A. Khoze and S. I. Troian, Z. Phys. C **55**, 107 (1992).

[27] C. P. Fong and B. R. Webber, Phys. Lett. B **229**, 289 (1989); C. P. Fong and
B. R. Webber, Phys. Lett. B **241**, 255 (1990); C. P. Fong and B. R. Webber, Nucl.
Phys. B **355**, 54 (1991).

[28] R. Perez Ramos, JHEP **0606**, 019 (2006) [arXiv:hep-ph/0605083], JHEP **0609**, 014
(2006) [arXiv:hep-ph/0607223].

[29] M. Gyulassy, S. K. Kauffmann, and L. W. Wilson, Phys. Rev. C **20**, 2267 (1979).

[30] P. D. Acton *et al.* (OPAL Collaboration), Phys. Lett. B **287**, 401 (1992).

[31] M. Z. Akrawy *et al.* (OPAL Collaboration), Phys. Lett. B **247**, 617 (1990).

[32] Y. L. Dokshitzer, V.A. Khoze and S.I. Troyan, in Perturbative Quantum
Chromodinamics, ed. A.H. Mueller (World Scientific, Singapore, 1989), p. 241;
E. D. Malaza and B. R. Webber, Phys. Lett. B **149**, 501 (1984); K. Tesima, Phys.
Lett. B **221**, 91 (1989).

[33] R. Perez-Ramos and B. Machet, JHEP **0604**, 043 (2006) [arXiv:hep-ph/0512236].

[34] F. Arleo, R. Perez-Ramos and B. Machet, In preparation.

[35] Fermilab Beams Division, **Run II Handbook**,
$http : //www - bdnew.fnal.gov/pbar/run2b/Documents/RunII_handbook.pdf$,
(1999).

[36] D. Acosta *et al.* (CDF Collaboration), Phys. Rev. D **71**, 032001 (2005)
[arXiv:hep-ex/0412071].

[37] The CDF II Detector Technical Design Report, Fermilab-Pub-96/390-E.

[38] K. A. Bloom *et al.* (CDF Collaboration), "Track reconstruction for the CDF silicon
tracking system"

[39] J. Elias *et al.*, Nucl. Instrum. Meth. A **441**, 366 (2000).

[40] S. Cabrera *et al.* (CDF Collaboration), Nucl. Instrum. Meth. A **494**, 416 (2002).

[41] E. J. Thomson *et al.*, IEEE Trans. Nucl. Sci. **49**, 1063 (2002).

[42] F. Abe *et al.* (CDF Collaboration), Phys. Rev. D **45**, 1448 (1992).

[43] S. D. Ellis and D. E. Soper, Phys. Rev. D **48**, 3160 (1993) [arXiv:hep-ph/9305266].

[44] A. Bhatti *et al.*, Nucl. Instrum. Meth. A **566**, 375 (2006) [arXiv:hep-ex/0510047].

[45] T. Sjostrand, Phys. Lett. B **157**, 321 (1985); M. Bengtsson, T. Sjostrand and M. van Zijl, Z. Phys. C **32**, 67 (1986); T. Sjostrand and M. van Zijl, Phys. Rev. D **36** (1987) 2019.

[46] R. Field, presented at Fermilab ME/MC Tuning Workshop, Fermilab, October 4, 2002; R. Field and R.C. Group (CDF Collaboration), arXiv:hep-ph/0510198.

[47] G. Marchesini and B. R. Webber, Nucl. Phys. B **310**, 461 (1988); I. G. Knowles, Nucl. Phys. B **310**, 571 (1988); S. Catani, B. R. Webber and G. Marchesini, Nucl. Phys. B **349**, 635 (1991).

[48] V. N. Gribov and L. N. Lipatov, Sov. J. Nucl. Phys. **15**, 675 (1972) [Yad. Fiz. **15**, 1218 (1972)]; G. Altarelli and G. Parisi, Nucl. Phys. B **126**, 298 (1977); Y. L. Dokshitzer, Sov. Phys. JETP **46**, 641 (1977) [Zh. Eksp. Teor. Fiz. **73**, 1216 (1977)].

[49] X. Artru and G. Mennessier, Nucl. Phys. B **70**, 93 (1974); M. G. Bowler, Z. Phys. C **11**, 169 (1981); B. Andersson, G. Gustafson and B. Soderberg, Z. Phys. C **20**, 317 (1983).

[50] R. D. Field and S. Wolfram, Nucl. Phys. B **213**, 65 (1983); B. R. Webber, Nucl. Phys. B **238**, 492 (1984).

[51] R. Brun, F. Bruyant, M. Maire, A. C. McPherson and P. Zanarini, "GEANT3", 1987.

[52] G. Grindhammer, M. Rudowicz and S. Peters, Nucl. Instrum. Meth. A **290**, 469 (1990).

[53] $\not{E}_T$ is defined as the norm of $-\Sigma_i E_T^i \cdot \vec{n_i}$, where $\vec{n_i}$ is the unit vector in the azimuthal plane that points from the beamline to the i-th calorimeter tower.

[54] C. Hays *et al.*, Nucl. Instrum. Meth. A **538**, 249 (2005).

[55] S. Sabik, P. Savard, "Track reconstruction efficiency in jets", CDF Note 6894, 2004.

[56] H. L. Lai *et al.* (CTEQ Collaboration), Eur. Phys. J. C **12**, 375 (2000) [arXiv:hep-ph/9903282].

[57] D. Stump, J. Huston, J. Pumplin, W. K. Tung, H. L. Lai, S. Kuhlmann and J. F. Owens, JHEP **0310**, 046 (2003) [arXiv:hep-ph/0303013].

BIOGRAPHICAL SKETCH

Sergo R. Jindariani was born in Tbilisi, (Republic of) Georgia on August 18,1980. He received primary education at the 37th middle school. In 1994 he successfully passed the examination and was admitted to the Vekua High School, the school oriented on providing exceptional level of education in physics and mathematics. During his years at high school Sergo participated in International Young Physicist Tournaments (third team award in 1996 and 1997, first individual award in 1996), as well as in the national physics and mathematics olympiads (multiple awards 1995-1997). He also played basketball at the point guard position. In 1997 he received a thank you letter from the President of Georgia, E. Shevardnadze, for academic excellence and leadership.

In 1997 Sergo graduated with honors from high school and applied to the Department of Physics at Tbilisi State University (TSU). For his achievements during the years of high school he was admitted without qualifying examinations. He was also a selected to be a recipient of George Soros Stipend (1997-2000). This stipend was established to provide financial support to outstanding students during their college years in countries with very poor economy. In his early years in college Sergo got introduced to the basics of particle physics, and his interest to the high energy physics grew quickly. At the same time he worked as system administrator at the Internet service provider "Geonet" and was one of the first few to implement the concept of IP-telephony in Georgia. In 2001 Sergo graduated from TSU with B.S. in Physics, *Summa Cum Laude*.

In late nineties the economy in Georgia was struggling and the level of education has also gone down. This, together with Sergos interest in particle physics, influenced his decision to take a research assistant position at the Joint Institute of Nuclear Research in Dubna, Russia. There, at the University Center, he also continued his education toward

Masters and PhD degrees. His research was mainly focused on developing numerical methods to solve equations describing very high multiplicity hadron processes.

In 2002 Sergo was admitted to graduate school at University of Florida. After completion of the course requirements, he engaged himself completely with research for the next three years. His research was focused on the jet fragmentation studies at CDF. Sergo presented his results at many international conferences. He also contributed to the online and offline operations of the Cherenkov Luminosity Counter (CLC) at CDF.